SISSA
Scuola
Internazionale
Superiore di
Studi Avanzati

Physics Area - PhD course in
Statistical Physics

Geometric approach to bounded critical phenomena

Candidate:
Alessandro Galvani

Advisors:
Andrea Trombettoni
Giacomo Gori

Academic Year 2021-22

Contents

List of Publications

- **A. Galvani**, G. Gori and A. Trombettoni, *Magnetization profiles at the upper critical dimension as solutions of the integer Yamabe problem*, Physical Review E 104.2 (2021), p. 02413

- **A. Galvani**, G. Gori and A. Trombettoni, *Critical* 1- *and* 2*-point spin correlations for the* $O(2)$ *model in* 3*d bounded domains*, Journal of High Energy Physics 2021, 106

- **A. Galvani**, A. Trombettoni and G. Gori, *High-precision anomalous dimension of* 3*d percolation from giant cluster slicing*, Physical Review E 106 (2022), p. 064111

Preface

This thesis is the result of my studies on critical phenomena in bounded domains. This is a fascinating field providing a playground for the application and development of methods initially used for critical phenomena in infinite, translationally invariant, bulk systems. The perspective from which bounded critical phenomena are studied is geometrical, and one aim is to develop the so-called critical geometry approach proposed in [1].

Chapter 1 starts with an introduction to critical phenomena, mean-field theory, renormalization, bounded systems, conformal field theory and the statistical models used in later chapters (Ising, XY and percolation).

Chapter 2 explains the concept of uniformization on which the critical geometry approach is based in a self-contained manner: for this purpose, it delves into the mathematics needed to define the fractional laplacian and the corresponding Yamabe problem on bounded domains. To emphasize the role of uniformization in our work hypothesis, in the following we will refer to the approach proposed in [1] as "uniformization approach" in alternative to "critical geometry approach".

The next three chapters are application of the uniformization approach to systems in different dimension: we start from $d = 2$ in Chapter 3, where results from boundary conformal field theory are recovered, and a test is performed through the two-dimensional Ising model. Chapter 4 contains most of my work, published in [2] and [3], as I tested the uniformization theory through Monte Carlo simulations of the three-dimensional XY model and percolation: the respective (bulk) anomalous dimensions exponents are extracted and compared with previous results. For the

case of the XY model, I studied two-point correlations as well. Chapter 5 examines systems at the upper critical dimension, where the fractional Yamabe equation reduces to the integer version, published in [4].

Finally, Chapter 6 discusses how to extend the conjecture to fields other than the order parameter, focusing in particular on the energy field for the three-dimensional Ising and XY models.

Chapter 1

Introduction

1.1 A reminder on critical phenomena

A thesis about boundary critical phenomena should, for the sake of being somewhat self-contained, start from an introduction to critical phenomena in general, i.e. in the full space. Since there is a plethora of excellent introductions that have already been written on the topic (such as the first chapters of [5, 6, 7]), this introductory part will be rather concise.

The theory of critical phenomena aims to describe the vast breadth of quirks and interesting phenomena that happen when a substance is undergoing a phase transition. This includes all the everyday transitions, such as ice melting, as well as many more which we can only see in a lab, such as bosons forming a Bose-Einstein condensate. The theory has been successful enough that it has been applied in contexts far from many physicists' comfort zones, ranging from the flight of a flock of birds [8] to neural networks [9] (including actual human neurons). Practically, whenever a system is composed of many similar elements interacting with each other based on a few parameters that can be varied, statistical physics can tell us something about it. And surprisingly often, a critical point – or several of them – is found in that system.Even more surprisingly, studying one of these systems can give us quantitative knowledge about many other systems which appear completely unrelated, thanks to a property called universality.

As is standard in statistical physics, when describing any of these systems, one starts from the microscopic degrees of freedom and tries to understand how they collectively affect measurable, macroscopic quantities, without attempting to solve the equations of motion for each particle, which would be, to put it lightly, unfeasible. To get some feel for what this is all about, we can start from an (almost) experimental

observation involving magnets.

To start, say we have an iron bar in a strong magnetic field $h > 0$: its magnetization will be close to a maximum value, meaning all its spins are aligned. As the intensity of the field is decreased, the magnetization also decreases, but when the field is switched off entirely, if the bar is at room temperature, it will still have a residual magnetization $m_0 > 0$. The same experiment could be repeated with a field aligned in the opposite direction $h < 0$, which would lead, even once switched off, to a negative magnetization $m = -m_0$, since m has to be an odd function of the magnetic field, as seen in Fig. 1.1. This abrupt change in the magnetization as the sign of the magnetic field is changed is an example of a first-order phase transition.

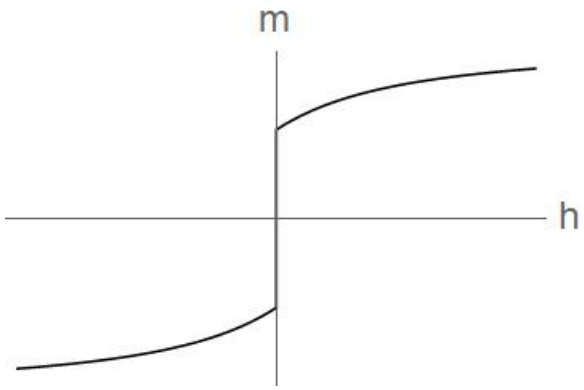

Figure 1.1: Magnetization as a function of the magnetic field for low temperature: there is a sharp jump when the field switches sign.

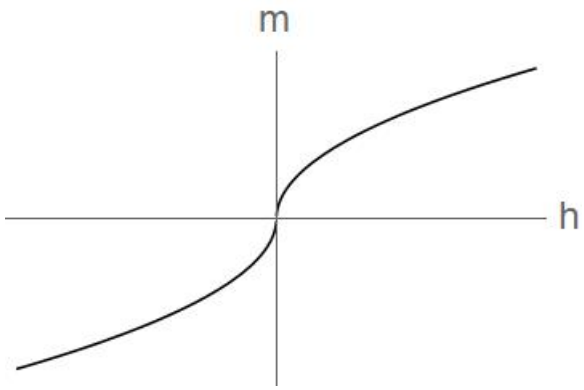

Figure 1.2: Magnetization as a function of the magnetic field at the critical temperature: the function is continuous, but its derivative at the origin diverges.

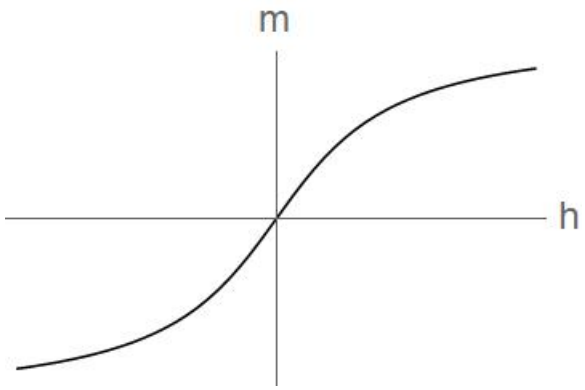

Figure 1.3: Magnetization as a function of the magnetic field for high temperature: the function is smooth.

Next, say the experiment is repeated at higher temperature: the same phenomenon is observed, but the value of m_0 is lower. As the temperature increases, we get to an important point, where this value first reaches 0: the plot $m(h)$ is no longer discontinuous, but it has infinite slope in the origin, as seen in Fig. 1.2. We call this temperature the critical temperature T_c, and the transition happening by varying T around T_c for $h = 0$ a second-order phase transition. For even higher temperature, the curve $m(h)$ is smooth, and nothing of interest (to us) happens, as seen in Fig. 1.3. The magnetization is therefore called the **order parameter** of the transition, since it discriminates between two regimes when $h = 0$: the low-temperature or ferromagnetic phase, where $m \neq 0$ (there is spontaneous magnetization) and the high-temperature or paramagnetic phase, where $m = 0$ (no spontaneous magnetization).

This phenomenology may seem specific to magnets, but is actually more general. The study of phase transitions concerns itself with all these peculiar points where a thermodynamic function exhibits a discontinuity: for example, if we plot the residual magnetization at vanishing magnetic field m_0 as a function of the temperature, we get Fig. 1.4.

1.1.1 Critical exponents

The previously discussed example shows how drastic changes in the macroscopic properties of a substance translate to singularities in thermodynamic functions. To quantify this, we should look at the free energy of the system,

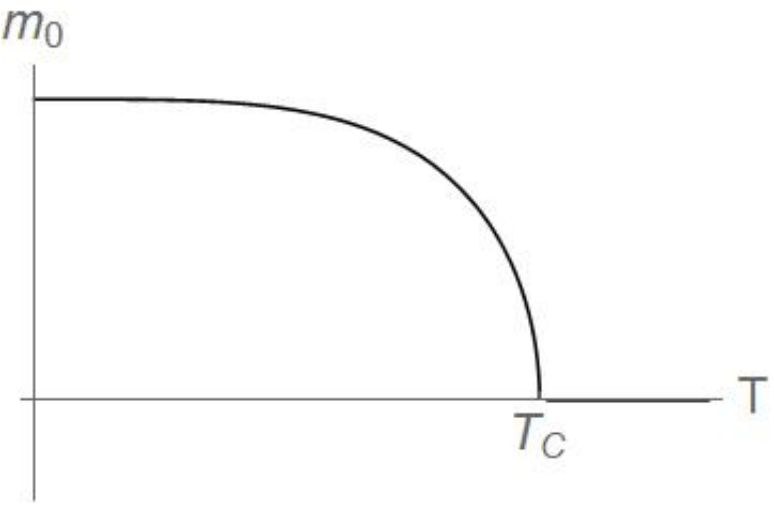

Figure 1.4: Spontaneous magnetization as a function of the temperature. The function is continuous, but its derivative jumps at $T = T_c$.

$$F = E - TS, \tag{1.1}$$

where S is the entropy. The free energy can also be defined from the partition function of the system, as

$$Z = \mathrm{Tr}\, e^{-\beta H} = e^{-\beta F}, \tag{1.2}$$

the trace being a sum on all the configuration of the system.

Derivatives of the free energy give various thermodynamic quantities. In particular, what we call first-order transitions are the ones which exhibit a discontinuity in the first derivative of the free energy, such as the magnetization. In the following I will always refer to the magnetization per spin, so we divide it by the number of spins N:

$$m = \frac{1}{N}\frac{\partial F}{\partial h} \tag{1.3}$$

(and when needed take the limit of large N).

In second-order transitions, instead, a discontinuity only appears once second derivatives of the free energy are computed, such as at the critical point from Fig. 1.2, where the magnetization is continuous but its derivative with respect to the magnetic field, called susceptibility, diverges:

$$\chi = \frac{\partial m}{\partial h} = \frac{1}{N}\frac{\partial^2 F}{\partial h^2}. \tag{1.4}$$

The divergence of the susceptibility and the vanishing of the magnetization at the critical point lead us to the introduction of some fundamental quantities in statistical mechanics: **critical exponents**. They are pure numbers which describe the behavior of a function at or near the critical point. For example,

$$\chi \propto |T - T_c|^{-\gamma} \tag{1.5}$$

and

$$m \propto (T_c - T)^{\beta} \quad , \quad T < T_c. \tag{1.6}$$

Critical exponents are not all independent. They are related by two sets of relations, called scaling and hyperscaling relations, which means that all exponents can be recovered from the knowledge of just two of them. These relations will be explored in more details later on.

The importance of these exponents is related to the other fundamental property of critical phenomena: **universality**. When trying to compute critical exponents and a few other special dimensionless quantities, many of the nuts-and-bolts details about the specific system do not matter. All that is relevant is the dimensionality of the system and which kind of symmetry is broken during the transition. This means that vastly different real-world phenomena, ranging from magnets to fluids to flocks of birds, can share the same critical exponents. This is what justifies devoting so much effort in the study of models which, at first glance, appear somewhat disconnected from reality: if we want to predict the critical exponents of any given critical phenomenon, we can determine which symmetry is broken during the transition, and then select whichever model with the same symmetry is easier to study, either through analytical techniques such as conformal field theory, or numerical ones such as Monte Carlo simulations and finite-size scaling. This is why, for example, we can determine the critical exponents of the superfluid transition of He^4 by studying a planar model of a magnet, which will be explained in more details in Section 1.2.1. Now, in practice, the actual experimental values of the Helium superfluid transition [10, 11] do not perfectly match the predicted exponent from conformal bootstrap [12], and this quite large discrepancy (eight standard deviations) is still an unsolved problem.

To see some slightly more concrete example of phase transitions and critical exponents, it might be useful to introduce the Ising model.

1.1.2 The Ising model

The most well-known statistical physics model is a lattice of spins with value $s_i = \pm 1$, each interacting only with its neighbors through the Hamiltonian

$$H = -\sum_i h s_i - \frac{J}{2} \sum_{\langle ij \rangle} s_i s_j. \tag{1.7}$$

The first term tells us that a magnetic fields tends to align the spins in the same direction as the field h, while the second term, the more interesting one, is the interaction between spins. For $J > 0$ the spins want to align with each other, so the ground state consists of spins all aligned in the direction of the magnetic field: either $\uparrow\uparrow\uparrow \ldots$ or $\downarrow\downarrow\downarrow \ldots$; for $h = 0$, these two states have the same weight.

The Ising model has been solved exactly (that is, its partition function was computed analytically) in one and two dimensions: while the $1d$ case is rather easy, the two-dimensional solution by Onsager [13] (in absence of external magnetic field) is not.

1.1.3 Mean field theory

A very rough approximation that can be used as a starting point in the study of statistical models, and which sometimes produces useful result, is called mean field theory. It basically consists of replacing the interaction between spins with the interaction between a single spin and an effective magnetic field, produced by the average of the spins.

To do that, we rewrite the Hamiltonian with this replacement:

$$s_i \to s_i + \langle s_i \rangle - \langle s_i \rangle = s_i + m - m, \tag{1.8}$$

where $\langle s_i \rangle = m$ is the average magnetization, and grouping the terms appropriately, we get

$$H = -\frac{J}{2} \sum_{\langle ij \rangle} \big(m^2 + m(s_i - m) + m(s_j - m) + (s_i - m)(s_j - m) \big) + h \sum_i s_i. \tag{1.9}$$

The mean field approximation consists in removing the last term $(s_i - m)(s_j - m)$ entirely, as it is quadratic in the spins. What we are left with is

$$H_{\mathrm{MF}} = -\frac{NJzm}{2} - (Jzm + h) \sum_i s_i, \tag{1.10}$$

where z is the number of neighbors of a site (for a square lattice $z = 2d$). This new Hamiltonian, up to a constant, can be seen as an Ising model without the interaction term, in which the magnetic field has been strengthened by the "background" effect of all the spins. It is now trivial to compute the partition function

$$Z = \sum_{\{s\}} e^{-\beta H_{\mathrm{MF}}} = e^{-\frac{1}{2}\beta N J z m^2} \left(\sum_{s=\pm 1} e^{\beta(Jzm+h)s} \right)^N = e^{-\frac{1}{2}\beta N J z m^2} \left(2\cosh(\beta J z m + \beta h)\right)^N . \tag{1.11}$$

From this, we get the free energy per spin

$$f = -\frac{1}{\beta N} \log Z = \frac{1}{2} J z m^2 - T \log(\cosh(\beta J z m + \beta h)), \tag{1.12}$$

and finally a derivative of the free energy gives the magnetization. Since it is a function of the magnetization itself, what we obtain is a self-consistency equation

$$m = -\frac{\partial f}{\partial h} = \tanh(\beta(Jzm + h)). \tag{1.13}$$

Plotting the two sides of the equation lets us see the number of solutions for a given value of the temperature, as per Fig. 1.5 for $h = 0$. For large β, we see three possible solution, which means we are in the low temperature phase with two opposite minima. For small β only the $m = 0$ solution remains, meaning we are in the disordered phase. From this, we can obtain the mean field critical temperature, where $y = m$ is tangent to $y = \tanh(\beta z J m)$. The solution is $T_c = Jz$.

This value is not the correct critical temperature for the Ising model, as we should expect from such a rough approximation. It should be noted, moreover, that while in $d \geq 2$ mean field theory gives at least qualitatively correct predictions, in $d = 1$ it fails entirely, as it predicts a finite temperature transition while the actual Ising model is disordered for any $T > 0$.

Equation (1.12) can also serve as a starting point for Landau theory.

1.1.4 Landau-Ginzburg theory

Landau theory aims at generalizing the expression for the free energy of the mean field Ising model to obtain a simple function that can still qualitatively describe symmetry breaking. To do this, we start by expanding (1.12) around $m = h = 0$, as we want to describe behavior near the critical point:

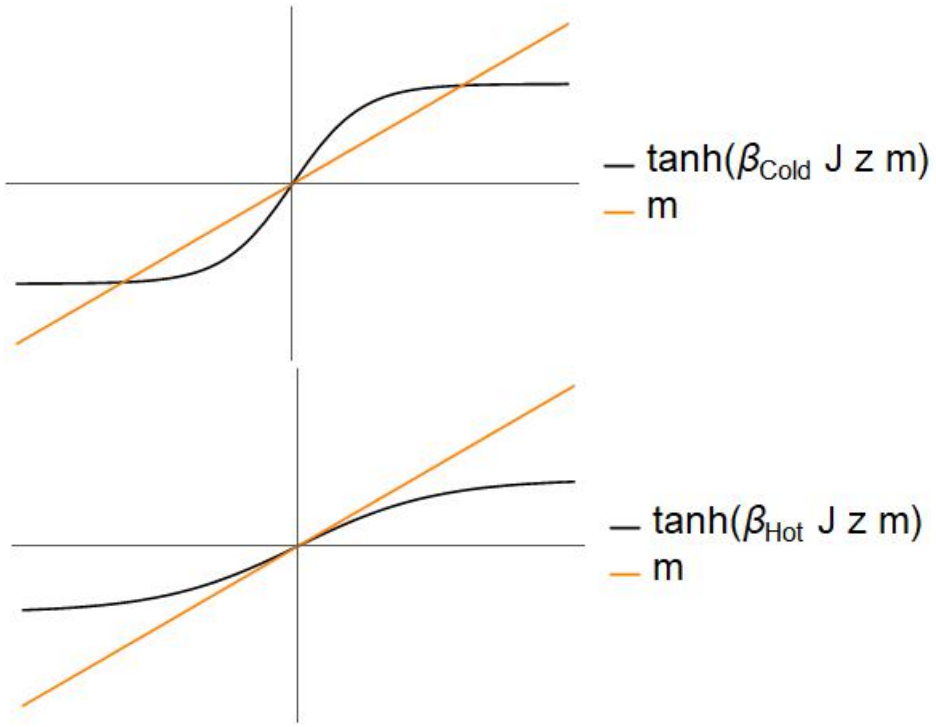

Figure 1.5: Self-consistency equation (1.13): above, $T < T_c$, so there are three intersections: the two minima $m = \pm m_0$ and $m = 0$; below, $T > T_c$, so only the solution with no magnetization remains.

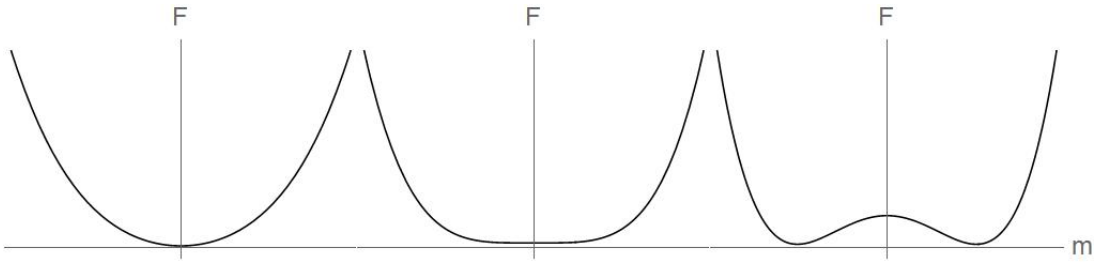

Figure 1.6: Landau free energy as a function of the magnetization, in the three cases: high temperature, critical point and low temperature, respectively. At the critical point, since the coefficient of the m^2 term vanishes, the function has a small slope around $m = 0$, which means that fluctuations have a small energy cost. For $T < T_c$ we see the emergence of two symmetric minima.

$$F \approx \frac{JNzm^2}{2} - \frac{TNm^2}{2} + \frac{T_c^4 Nm^4}{12T^3} - Nhm = 2N(T - T_c)m^2 + \frac{g}{2}m^4 - hm. \quad (1.14)$$

Since $Jz = T_c$, and we defined $g = N\frac{T_c^4}{6T^3} \approx \frac{N}{6}T_c$. For $h = 0$,

$$F = \frac{\mu^2}{2}m^2 + \frac{g}{2}m^4. \quad (1.15)$$

The coefficient of the quadratic term has been called $\mu^2 \propto (T - T_c)$ as it has the role of mass of the system (i.e. it vanishes at the critical point) and the letter m was already taken. This function provides a classical and arguably rather intuitive way to explain symmetry breaking.

One might also come to the conclusion that this F is a sensible choice without even coming from the mean-field calculation. If we take a step back, so far we understood that a hot magnet is not magnetized, while a cold one either has positive or negative magnetization, with the same probability absent an external field. We also know that the system, at any temperature, minimizes its free energy. How do we introduce a model so that the latter justifies the former?

One needs a free energy which is function of both the magnetization and the temperature $F(m, T)$, so that for $T > T_c$ it has a single minimum, in $m = 0$, while for $T < T_c$ it has two minima, in $m = \pm m_0(T)$. Indeed, Eq. (1.15) has all these properties: if we start from $T > T_c$, $m = 0$ is clearly the only minimum, so at equilibrium the system will have no magnetization. As the temperature is lowered, however, the shape of the function changes as seen in Fig. 1.6.

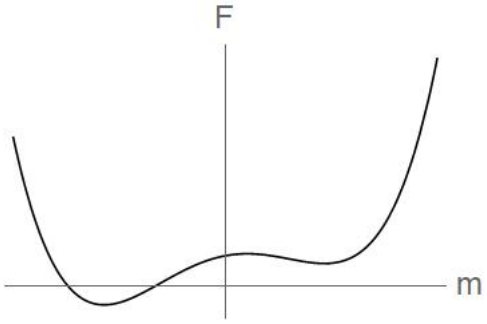

Figure 1.7: Landau free energy at low temperature with a small magnetic field, that leads to one minimum being favored over the other.

Finally, if we switch on the magnetic field, we introduce in the free energy the term $h\,m$, which is odd in m and therefore breaks explicitly the $m \to -m$ symmetry. As we can see in Fig. 1.7, the two minima now no longer have the same free energy, as the one in which the spins are aligned to the magnetic field is favored.

Overall, despite descending from a rather coarse approximation, we see how Landau theory can qualitatively explain all the phenomena we have seen so far: the alignment of spins with a magnetic field, the presence of spontaneous magnetization even when this field is absent, and the disappearance of this magnetization when the temperature is raised above the critical point.

For our purposes, we need to generalize this slightly by turning the free energy, function of the magnetization, into an action, functional of a magnetization field. This means promoting the magnetization to a field ϕ, which represents the local mean value of many spins. To do this, another term needs to be added to the free energy, that quantifies the energy cost related to the presence of fluctuations: when the magnetization is not uniform throughout the system, even if its mean value is the same, the configuration has higher energy. This term is the same as the kinetic term in high-energy field theories: $(\nabla\phi)^2$. So the Landau-Ginzburg action has the form

$$S = \int d^d x \left((\nabla\phi)^2 + \frac{\mu^2}{2}\phi^2 + \frac{g}{2}\phi^4 \right). \tag{1.16}$$

The quadratic terms make up the free part of the action, while any term with a higher power of ϕ (or of another form) is the interaction. The Landau-Ginzburg action is often used as a lab rat to learn about renormalization. Other conventions for the coefficients of the last term are often used; this one was chosen to match the notation of Chapter 5.

1.1.5 Renormalization

Any attempt to thoroughly explain the renormalization group from the beginning would inevitably take up most of this thesis, so I will be less ambitious. All that we need here is to introduce the concept of upper critical dimension, which will be investigated in Chapter 5. To this end, we present a short and mostly qualitative explanation and any interested reader is advised to read more on it on classical sources, such as [14, 15].

The main idea is that critical properties, the ones we are interested in, do not depend on short-distance details of the system. So, starting from a model on an infinite lattice with a lattice spacing a, we can try and determine what the model will look like to us if we inspect it with a tool that has a distance resolution of $2a$. Most of the time, we can write a new Hamiltonian which describes the system we actually see, which may be similar although not identical to the original one. Then we call the new lattice spacing a and imagine our resolution is even worse, twice this new lattice size, and we can repeat the procedure. Sometimes, after we do this a few (or infinitely many) times, the Hamiltonian that we use to describe the new system stops changing. We reached what is called a fixed point, which is a very interesting object in high-energy physics as well, but for our purposes describes the system at the critical point. Among many quirks, the most visible one is self-similarity: if one keeps zooming out, after the critical point is reached the system at the new scale looks the same as the system at the previous scale: it is a fractal.

This procedure, despite being called a group, is irreversible: whenever we zoom out, we lose something that we previously know about the system. This is a good thing: all the details that we are forgetting are not important to our description. Once we reach the fixed point, it means we dropped all these nitty-gritty specs and we are left with only what we need.

All of this can be done either on a lattice, by defining on each step of the procedure a new "Big Spin" that replaces a block of adjacent spins, or directly from the field theory; the latter is what we are interested in.

We can see what this coarse-graining procedure looks like on the action (1.16). At each step of the renormalization process, we zoom out, meaning that the new coordinate x' is related to the old one x by $x' = \zeta x$, for $\zeta > 1$. As a consequence, derivatives will get rescaled by the inverse factor, and in particular $\triangle' = \zeta^{-2}\triangle$, while fields will get rescaled according to their scaling dimension $\phi'(x') = \zeta^{\Delta_\phi}\phi(x)$. If we start from an action with just the kinetic term,

$$S = \int d^d x (\nabla\phi)^2, \tag{1.17}$$

then the action remains unchanged after this transformation if $\Delta_\phi = \frac{d-2}{2}$. This means that looking at the system from further away does not change anything: we found a fixed point, where the model exhibits self-similarity. In particular, the field in the Gaussian fixed points has no anomalous dimension.

We can now see what happens when we add more terms to the action. If a mass term is added $\frac{\mu^2}{2}\phi^2$, after a renormalization step we see that the term has become $\zeta^2\frac{\mu^2}{2}\phi^2$. It has the same shape as before, but with a new mass $\mu' = \zeta^2\mu$. This means that as we keep repeating this procedure, μ keeps increasing, so the mass terms becomes more and more important in the action. This means the term proportional to ϕ^2 is *relevant*: if we start the renormalization process near the Gaussian fixed point but even with a small value of μ, we will be driven away from it.

So what about the ϕ^4 term? The coupling g changes as $g' = \zeta^{4-d}g$. This means that for $d < 4$ this term is relevant, while for $d > 4$ it is *irrelevant*. Exactly at $d = 4$ this term is called *marginal*. $d = 4$ has therefore an important role in a ϕ^4 theory: above it, an action with this term flows towards the Gaussian fixed point (if the mass term is not present), while below the renormalization flow pushes the theory away from the Gaussian fixed point. $d = 4$ is called the upper critical dimension of the theory d_c. It can also be interpreted as the dimension above which fluctuations around the mean value of the field become negligible, allowing mean field theory to provide correct results, while it fails below d_c.

In the same way, one can see that an action with a ϕ^6 term has upper critical dimension $d_c = 3$ and ϕ^3 has $d_c = 6$.

1.2 Models

In the next chapters we will introduce two other statistical models which we introduce in quite general terms here: the XY model and percolation.

1.2.1 XY model

The Ising model needed an early introduction, as without it, it is rather difficult to explain any statistical physics topic. The next model, the XY model, can be quite easily seen as an extension of the Ising model, with a different symmetry group: $O(2)$ rather than Z_2. It still consists in spins on a lattice, and each spin still interacts only with its nearest neighbors, but the difference lies in the fact that now the spins are free to rotate continuously on a circle, rather than having only two possible values. The Hamiltonian, like in the previous case, favors the alignment of the spins:

$$H = -J \sum_{\langle i,j \rangle} \vec{s}_i \cdot \vec{s}_j - \sum_i \vec{h} \cdot \vec{s}_i, \tag{1.18}$$

with

$$\vec{s}_i = (\cos\theta_i, \sin\theta_i), \qquad \theta_i \in [0, 2\pi). \tag{1.19}$$

So we can alternatively treat the angles themselves as the degrees of freedom, with an interaction $-J\cos(\theta_i - \theta_j)$.

The universality class of $3d$ models with $O(2)$ (or $U(1)$, if one prefers high-energy terminology for groups) symmetry finds broad application in different areas of physics, thanks to its ability to describe various phenomena ranging from high-energy models and lattice gauge theories [16, 17] to superfluids and superconductors [18], while at the same time being amenable to be studied by both analytical and numerical techniques.

The most studied lattice counterpart to the $O(2)$ field theory is the XY spin model, which can describe the chiral transition of lattice QCD in the presence of two staggered quark flavors [19, 20]. The XY Hamiltonian also provides a model for liquid helium on a lattice [21, 22], which allows it to describe the superfluid transition of ^{4}He across the λ line. This phase transition enjoys extremely accurate experimental studies [10], thanks to a weakly singular compressibility of the fluid and the possibility of performing experiments in space [11], to reduce gravitational effects that would broaden the transition. However, the experimentally determined exponent of the specific heat α (and therefore, the exponent ν as well) differs from the most accurate numerical results, obtained from Monte Carlo simulations [23], by a whopping eight standard deviations. Successive conformal bootstrap results [12] confirm the Monte Carlo values, meaning that this discrepancy is still an open problem. Another remarkable phenomenon displayed by the XY model is the appearance of vortices and vortex lines: in $2d$, vortices drive the celebrated Berezinskii–Kosterlitz–Thouless transition [24, 25], while vortex loops appear in the $3d$ XY model [26], providing a topological mechanism for its order-disorder transition an additional tool to tackle the problem of the specific heat of helium [27] and duality in (2+1)-d systems at finite temperature [28].

It should come as no surprise, then, that after the uniformization theory was tested on the Ising model, the next step is to apply it to the three-dimensional XY model in a slab, a task discussed in Chapter 4.1.

1.2.2 Percolation

The next model that needs to be introduced is not a spin model, but something arguably even simpler: percolation. What follows does not assume that the reader is in any way familiar with this phenomenon, while still hoping I will not appear excessively didactic. Besides, percolation has an invaluable and pedagogical geometrical meaning. Better sources to learn about percolation include [29, 30, 31].

Despite being introduced to study molecules branching to form a gel [32, 33], a simpler example often used to explain percolation goes like "Imagine having a rock and pouring water on the top. How porous does the rock have to be before the water starts coming out the bottom?". It may then seem like percolation is a rather concrete problem. Indeed, there happens to be a plethora of real-world phenomena which are, at least as a first approximation, described by percolation theory. Whether you are interested in saving forests from fires [34] or saving people from epidemics [35, 36, 37, 38], you might end up encountering this model. I shall resist the urge to quote Feynman, but all these applications are not, currently, my main interest.

The actual reason we study percolation is because it is a disarmingly simple concept with surprisingly interesting features. Out of the many similar models which fall into the same class, the easiest to define is site percolation. Pick any lattice, and then for each site toss a weighed coin: that site will be labeled "open" with probability p and "closed" with probability $1 - p$, independently from other sites. Some open sites will be adjacent to one or more other open sites: we call a cluster any set of connected open sites. The study of percolation is then the study of the statistical properties of these clusters. For the sake of completeness, it should be added that a very similar model can be defined on the bonds of the lattice, rather than the site; this is called bond percolation. In this case, each bond has a probability of being open, and two bonds with an end in common belong to the same cluster.

The study of percolation is, in essence, the study of the distribution of clusters[1]. The model lacks a Hamiltonian, any notion of temperature and therefore there are no Boltzmann weights: at a first glance, one might assume it lacks any physics, and may naively conclude that clusters simply grow larger as one increases p, in a continuous fashion. However, changing the only parameter, p, has a much more interesting effect: the model undergoes a phase transition. Below a critical value p_c, each cluster in the lattice consists of a few sites, a vanishingly small fraction

[1]The meaning of a cluster in various real-world applications is quite intuitive. If a tree catches fire, one may want to know how far the fire will spread, i.e. how many other trees belong to the same cluster. The same can be said for epidemics.

in the thermodynamic limit. Increasing p, some of these clusters merge, until, at the critical point, they form what is known as giant or macroscopic or simply large cluster, which contains a finite fraction of all the lattice points.

The initial explanation of liquid passing through porous material comes in handy to confer the transition a more intuitive interpretation. For a finite lattice (we can imagine a square lattice of size N for simplicity), we can define two opposing boundaries and ask: what is the probability $\mathcal{P}$ that a path of open sites exists from one boundary to the other? This must clearly be a non-decreasing function of p. For finite N, $\mathcal{P}$ is almost zero for small p, grows quickly around some value and reaches 1 for $p = 1$. In the limit $N \to \infty$, however, this probability jumps from 0 for $p < p_c$ to 1 for $p > p_c$: this discontinuity, which is also quite apparent in simulations with relatively small lattices, is the clearest fingerprint of a phase transition.

Another typical feature of critical phenomena is self-similarity [39]. The appearance of fractals at the critical point is particularly striking for the case of percolation, as it lends itself to graphical representations. Looking at two pictures of the same large cluster, one which zooms in on a "branch" of the other, there is no way to tell which is contained in the other: this shows the disappearance of length scales at the critical point.

Yet, percolation feels different from spin models; this distinction can be reconciled through a process of analytic continuation, by which one can see percolation as a limit of the Potts model.

1.2.3 Potts model and analytic continuation

Some quantities which are easily defined for spin systems may initially cause some head scratching if discussed for percolation. In order to see what one means by correlation functions and critical exponents in percolation models, it is instructive to revise the analytic continuation that allows to consider percolation as the $q \to 1$ limit of the Potts model [40].

To start off, the q-state Potts model is a lattice model with spins that can take q different values or—more pictorially—colors, $s_i = 1, \ldots, q$. Its Hamiltonian is simply:

$$H = -K \sum_{\langle ij \rangle} \delta_{s_i, s_j}. \tag{1.20}$$

It shares the configuration space of the q-state clock model, but it differs in its interaction: while in the clock model any pair of adjacent spins provide an energy contribution, in the Potts model only sites with the same color interact. For this reason, its symmetry group is the group of permutations of q objects, S_q, which

justifies the name color: the values of spins can be seen as labels, and changing the name of each label does not change the energy.

As one can guess, there exists a critical temperature above which each color is equally represented, and below which one color is more likely to be present than the others. It makes sense, then, to define as order parameters

$$\sigma_\alpha(i) = \delta_{s_i,\alpha} - \frac{1}{q}, \qquad \alpha = 1, \dots q. \tag{1.21}$$

So, for $T > T_c$, $\langle \sigma_\alpha(i) \rangle = 0 \ \forall \alpha$, while for $T < T_c$ they differ from zero.

To find out how one gets from the Potts model to percolation [41], one computes the partition function of the former:

$$Z = \sum_{\{s\}} e^{\beta K \sum_{\langle i,j \rangle} \delta_{s_i,s_j}} = \sum_{\{s\}} \prod_{\langle i,j \rangle} e^{\beta K \delta_{s_i,s_j}} = \sum_{\{s\}} \prod_{\langle i,j \rangle} \left(1 + x \delta_{s_i,s_j}\right), \tag{1.22}$$

having defined $x = e^{\beta K} - 1$. One can map each Potts configuration to a graph on the same lattice, by drawing a line between sites with the same color. A set of lines is called a cluster. The partition function can then be seen as a sum of all the possible ways to connect sites into clusters $\mathcal{G}$, where each cluster configuration corresponds to many different Potts configurations, since each cluster can be colored in q different ways. For a given set of clusters, we then have q^{N_c} configurations with the same weight, where N_c is the number of clusters. The partition function is then:

$$Z = \sum_{\mathcal{G}} q^{N_c} x^{N_b}, \tag{1.23}$$

where N_b is the total number of bonds. So the average of a quantity $\mathcal{O}$ in the Potts model is simply

$$\langle \mathcal{O} \rangle_q = Z^{-1} \sum_{\mathcal{G}} \mathcal{O}\, q^{N_c} x^{N_b}. \tag{1.24}$$

On a lattice describing bond percolation, consisting of N sites and with each bond active with probability p, the average of an observable $\mathcal{O}$ is given by

$$\langle \mathcal{O} \rangle = \sum_{\mathcal{G}} \mathcal{O} p^{N_b} (1-p)^{N - N_b}, \tag{1.25}$$

where we sum over all possible configurations $\mathcal{G}$, each with N_b active bonds. This means that if we set $x = p/(1-p)$, then (1.24) for $q = 1$ coincides with (1.25). This

means that percolation can be seen as the analytic continuation of the Potts model for $q \to 1$. This may seem confusing at first, since based on the definition above a Potts model with a single color makes no sense, but it means that if we can compute analytically some quantity related to the Potts model for a generic number of colors q, then we can take the $q \to 1$ limit and we obtain the corresponding quantity for percolation. As an example, the mean number of sites of a cluster (below the critical point) in percolation is given by

$$N_c = \lim_{q \to 1} \frac{\partial \log Z}{\partial q}. \tag{1.26}$$

Another rather intuitive percolation quantity one can define and measure is the pair connectivity $g(x, y)$, the probability that two sites belong to the same cluster. In the limit of large distances, this probability vanishes below the critical point, and becomes the square of the probability that a point belongs to the large cluster P above the critical point:

$$\lim_{|x-y| \to \infty} g(x, y) = \begin{cases} 0, & p \leq p_c \\ P^2, & p > p_c \end{cases}. \tag{1.27}$$

From the pair connectivity one can obtain the mean cluster size, by counting the number of points connected to a reference point:

$$S = \sum_x g(x, 0). \tag{1.28}$$

Above the critical point this quantity clearly diverges, so g must be replaced by g_c, the connected connectivity, which only considers points not belonging to the large cluster, to obtain finite results.

The connected connectivity can then be used to define the correlation length:

$$\xi^2 = \frac{\sum_x |x|^2 g_c(x, 0)}{\sum_x g_c(x, 0)}. \tag{1.29}$$

What is the corresponding quantity in the Potts model? First, one can compute the probability that a site is of a given color α:

$$\left\langle \delta_{s(x),\alpha} \right\rangle_q = \frac{1}{q}. \tag{1.30}$$

Similarly, we can compute a "two-point function" as the probability that two sites are both of the same given color α. If we know the probability that the two

sites belong to the same cluster $g_c(x,y)$, we can write this average as the sum of two terms: if the two sites belong to the same cluster, then there is a one-in-q chance that they will be of the given color, otherwise there is still a chance they will both "accidentally" be of color α, with a $1/q^2$ chance:

$$\left\langle \delta_{s(x),\alpha}\delta_{s(y),\alpha}\right\rangle = \frac{1}{q}g_q(x,y) + \frac{1}{q^2}(1-g_q(x,y)). \tag{1.31}$$

Now we can replace the Kronecker δs with the σs from Eq. (1.21) and we get

$$\left\langle \sigma_\alpha(x)\sigma_\alpha(y)\right\rangle_q = \frac{q-1}{q}g_q(x,y). \tag{1.32}$$

Now, the $q \to 1$ limit of the Potts connectivity g_q is clearly the percolation connectivity, and we related it to the actual two-point function (since the σs serve as the order parameter) of the Potts model. This means that

$$g(x,y) = \lim_{q\to 1}\frac{1}{q-1}\left\langle \sigma_\alpha(x)\sigma_\alpha(y)\right\rangle. \tag{1.33}$$

This allows us to link critical exponents of the Potts model to percolation: percolation quantities defined above, such as the probability that a point belongs to the large cluster P and the mean cluster size S, can be obtained, respectively, from the magnetization and the susceptibility of the Potts model:

$$\begin{aligned} P &= \lim_{q\to 1}\frac{m}{\sqrt{q-1}}, \\ S &= \lim_{q\to 1}\frac{\chi}{q-1}. \end{aligned} \tag{1.34}$$

And the percolation correlation length is simply the Potts correlation length evaluated at $q = 1$. This means that the critical exponents of percolation can also be obtained from the Potts critical exponents if the latter are known analityically in q:

$$\begin{aligned} P &\propto (p-p_c)^\beta, \\ S &\propto |p-p_c|^{-\gamma}, \\ \xi &\propto |p-p_c|^{-\nu}. \end{aligned} \tag{1.35}$$

This way, we have seen the percolation transition is characterized by critical exponents like other statistical models: while being related to spin systems, it still differs from them by lacking unitarity, which the analytic continuation does not preserve.

1.3 Boundary critical phenomena

1.3.1 History

After learning about critical phenomena in $\mathbb{R}^d$, and enjoying the comfort of full translational and even conformal invariance, free of any length scale, one might understandably be wary at the idea of studying those same systems in bounded domains. We should, however, see boundaries as a feature, rather than a bug: quite a few interesting phenomena only manifest in systems with a boundary. As an example, in a mixture of two fluids, we can observe a transition between a mixed phase and a phase in which the fluids are separate. At the critical point, long-range forces act on the boundaries of this system, leading to the thermodynamic Casimir effect [42]. It shares the name of the well-known effect in quantum electrodynamics since both involve a change in the energy of a region of space as it is limited by two parallel plates, leading to a force acting on them. The Casimir effect has shifted the spotlight from semi-infinite systems [43, 44, 45, 46] to the geometry of a slab [47, 48, 49, 50, 51, 52], which is going to be the main focus of this thesis as well.

Besides being interesting, studying bounded systems is also often useful, in no small part because the real world is made of finite objects: a theory which takes boundaries into account is necessary to predict and interpret the results of experiments. Numerical simulations also use finite systems, and can be of great use in understanding how the size of the system, its shape and its boundary conditions affect various observables. This is especially true at the critical point: while, for most values of the parameters, any effect of a boundary only propagates a few layers into the lattice, in a critical system, thanks to diverging correlation length, the effect of a boundary can be felt deep within the bulk.

Multiple techniques have been developed that exploit the finiteness of a real or simulated system to extract bulk properties, with the most well-known method being finite-size scaling [53, 54], commonly used to extract critical exponent from numerical simulations.

Boundary critical phenomena received little attention until the mid 70's [55]. Renormalization group techniques had not yet been extended to bounded systems, experiments were not precise enough to discern the effect of boundaries, and conformal field theory was still a decade away. In the following thirty years, the subject of boundaries saw exploration from various different angles. It attracted the attention not just of condensed matter physicists working on magnets or quantum impurities [56], but also of high-energy physicists studying field theories on manifolds with boundaries [57, 58] and biophysicists using polymers near a surface [59].

The importance of conformal symmetry in the study of critical systems was first understood by Polyakov in 1970 [60], but it was not until 14 years later that what we call Conformal Field Theory emerged [61], with the discovery that the symmetry group of the critical point of many two-dimensional quantum field theories is infinite-dimensional: the Virasoro algebra emerging from this symmetry has allowed for exact solutions of these theories. It did not take much longer for the machinery of CFT to be applied to bounded systems: Boundary Conformal Field Theory [62, 63], even ignoring its applications in both string theory and statistical physics, has some advantages compared to bulk CFT, as it is mathematically simpler and its operator structure appears in a more intuitive way [64].

Then, just before the turn of the millennium, the paper [65] opened the door for the study of holography, greatly increasing the interest in boundaries. The AdS/CFT correspondence relates a theory of quantum gravity defined on a $d+1$-dimensional space with Anti-de Sitter metric to a Conformal Field Theory defined on the boundary of this space, which is d-dimensional. This means that, contrary to the intuitive idea that a higher dimensional system has to contain "more" information, each observable in the bulk theory corresponds to one in the boundary theory, meaning that the boundary contains all the information about the entire bulk. One reason for the success of this duality is that it relates a strongly-interacting theory to a weakly-interaction one, which is often more tractable.

While this correspondence was invented and mostly applied to the case of string theory, where a gauge theory is defined on a space embedded within a larger space with gravity, there are applications in lower energy fields, like the study of superconductors and superfluids, cold atoms and quantum phase transitions [66].

1.3.2 Surface critical behavior

To understand how the presence of a boundary alters the critical properties of a system, let us go back to the simplest case, which we have seen in the bulk for now (Section 1.1.3): the mean-field theory of the Ising model. In this case, we cannot simply replace the interaction with the spin average times the number of nearest neighbors, since not all spins have the same number of neighbors. So we go back one step and consider a slightly more general interaction $J(x, x')$, with arbitrary range for now. The self-consistency equation for the magnetization (1.13) only changes slightly [67]

$$m(x) = \tanh\left(\beta \sum_{x'} J(x, x') m(x')\right). \tag{1.36}$$

From this, one obtains the bulk critical temperature by setting $\beta \sum_{x'} J(x, x') = 1$. For now, we assume that the coupling J has the same value close to the boundary as it has in the bulk: this is known as an ordinary transition. If this is the case, then $\beta \sum_{x'} J(x, x')$ will be smaller for x close to the boundary, meaning that slightly below the critical temperature the value of the magnetization will decrease approaching the boundary.

From the coupling $J(x, x')$ we can define its (square) range,

$$R^2(x) = \frac{\sum_{x'} x'^2 J(x, x')}{\sum_{x'} J(x, x')}. \tag{1.37}$$

In the bulk, $R(x)$ assumes a constant value R. Similarly, the denominator in this expression,

$$J(x) = \sum_{x'} J(x, x'), \tag{1.38}$$

is constant everywhere except near the boundary, meaning that in the continuum limit it can be written as its bulk value J plus a correction

$$J(x) \approx (J - \frac{R^2}{2\lambda}\delta(x)), \tag{1.39}$$

where λ is positive unless the boundary coupling has been enhanced. One can then Taylor expand the magnetization:

$$\sum_{x'} J(x, x')m(x') = \sum_{x'} J(x, x')m(x) + \frac{1}{2}R^2 J \frac{\partial^2 m(x)}{\partial x^2} + \cdots, \tag{1.40}$$

and then substitute the expression for J from (1.39):

$$\frac{1}{2}R^2 \frac{\partial^2 m}{\partial x^2} + m - \left(\frac{R^2}{\lambda}\right)\delta(x)m = (\beta J)^{-1} \tag{1.41}$$

At the critical point $\beta J = 1$, expanding the hyperbolic tangent, one gets the usual equation

$$\frac{1}{2}R^2 \frac{\partial^2 m}{\partial x^2} = tm + \frac{1}{3}m^3. \tag{1.42}$$

What we are interested in is the boundary condition: integrating (1.41) in a small region around the boundary $x = 0$, one gets:

$$\frac{\partial m}{\partial x} = \lambda^{-1} m. \tag{1.43}$$

So, all throughout the bulk the magnetization, below the critical temperature, assumes a constant value. As one approaches the boundary, the magnetization decreases. If this magnetization profile were prolonged beyond the boundary, in the $x < 0$ region, with a straight line, then it would vanish at $x = -\lambda$. This gives an intuitive meaning to the quantity introduced in Eq. (1.41), which is called *extrapolation length* [67]. In practice, this quantity is of microscopic length, but it still has an important effect as it cuts away part of the magnetization profile, as will be explored later. For an example of how including an extrapolation length allows numerical results to match universal predictions, see [68].

Going back to (1.42), we can see that, for $t \to 0^-$, the magnetization in the bulk vanishes as $(-t)^{\frac{1}{2}}$, recovering the usual mean-field exponent $\beta = \frac{1}{2}$. Another aspect that enriches the topic of boundary critical phenomena, however, is the presence of other exponents, besides the well-known bulk ones. Similarly to what is done in the bulk case, some of these exponents can be extracted from scaling arguments: as an example, we can see how the boundary magnetization vanishes at $t \to 0^-$. To this end, we can write the magnetization as a constant bulk term plus a boundary contribution, function of z:

$$m(z) = m_B + \delta m(z). \tag{1.44}$$

Since the bulk term is expected to be the main contribution, we can substitute this expression into (1.42) keeping only terms up to linear order in $\delta m(z)$. While the zero-order terms reproduce the bulk mean-field equation, the first order terms give

$$\frac{R}{2}\delta m''(z) = \delta m(z)(t + m_B^2) \propto -t\delta m(z), \tag{1.45}$$

whose solution, knowing that $\delta m(z) \to 0$ as $z \to \infty$, is

$$\delta m(z) \propto e^{-z\sqrt{-t}}. \tag{1.46}$$

Since the bulk correlation length is $\xi \propto (-t)^{-1/2}$, we conclude that the boundary magnetization below the critical temperature approaches its bulk value over an exponentially short distance, of the order of ξ. We can then write a scaling form of the solution of (1.42):

$$m(z) = (-t)^{\frac{1}{2}} f\left(\frac{z+\lambda}{Rt^{-1/2}}\right), \tag{1.47}$$

where f must be an analytic function, since m is the solution of the differential equation (1.42), with the properties $f(0) = 0$, so that the magnetization vanishes if the profile is continued to $z = -\lambda$ and $f(z \to \infty) \to k$ for some finite constant k, so that the bulk magnetization is constant in z and vanishes with the temperature as $(-t)^{1/2}$. Based on the boundary condition (1.43), the magnetization has a finite derivative in $z = 0$, meaning that its series expansion contains a first-order term. So we can expand f as

$$f\left(\frac{z+\lambda}{Rt^{-1/2}}\right) \approx c(z+\lambda)t^{1/2} + O(t). \tag{1.48}$$

This means that, near $z = 0$ and slightly below the critical temperature, one can expand f to first order and obtain that

$$m(0) \propto -t. \tag{1.49}$$

This is an example of a **surface exponent**, $\beta_1 = 1$: the magnetization on the boundary, as the critical point is approached, vanishes faster than the bulk magnetization. It should be noted that while boundary theories contain new critical exponents, it is still possible to compute the usual (i.e., bulk) exponents from them, as we are going to do in the next chapters.

Ordinary, extraordinary and special transitions

In the previous example, the couplings on the boundary have the same strength as the couplings in the bulk, so that at the (bulk) critical point the entire system is disordered, and by lowering the temperature further the bulk orders and causes the boundary spins to order as well. This is what is known as an **ordinary** transition. There are other options as well: if the couplings on the boundary are enhanced sufficiently, the boundary would align at higher temperature than the bulk. Let us imagine starting from very high temperature, where everything is disordered: lowering the temperature to $T_c^{(d-1)}(J_{\text{boundary}})$, one would first encounter a phase transition for the degrees of freedom on the boundary alone: this **surface transition** belongs then to the same universality class as the bulk transition, but in one fewer dimensions. Lowering the temperature further to $T_c^{(d)}(J_{\text{bulk}})$, we would then have a further transition, happening in the bulk in the presence of an already aligned boundary: this is known as an **extraordinary transition**.

If the boundary coupling is gradually lowered, the surface transition temperature approaches the extraordinary transition temperature: when the two coincide, one has reached the **special transition**. This can be seen as a sort of multicritical point, as

it requires tuning one additional parameter (the relative strength of the boundary coupling with respect to the bulk coupling) in addition to the temperature and any other relevant quantities.

It should be added, of course, that any transition occurring on the surface still has to respect the no-go theorems of statistical physics: no spontaneous breaking of a continuous symmetry in $d = 2$ at finite temperature (Mermin-Wagner theorem [69]) and no finite-temperature transitions in $d = 1$ (sometimes called Landau argument). So, for example, if we want to have a bulk transition in a two-dimensional Ising model (or a three-dimensional Heisenberg model) in the presence of an ordered boundary, this cannot be achieved simply by enhancing the boundary couplings, but a magnetic field localized on the boundary has to be introduced in order to break the symmetry explicitly.

1.4 Boundary conformal field theory

Some special cases of the uniformization theory presented in the next chapter reproduce a few results of boundary CFT, so it is worth briefly explaining its basics. This section assumes familiarity with the ABC of $2d$ CFT in, which can be found in the "Yellow Pages" [70]. In particular, all we need are the facts that

- conformal symmetry imposes strong constraints on field correlation functions;
- each field is characterized by a pair of numbers called holomorphic dimensions, that determine the decay of its correlations:

$$\langle \phi(z_1, \bar{z}_1)\phi(z_2, \bar{z}_2)\rangle = \frac{\alpha}{(z_1 - z_2)^{h_\phi}(\bar{z}_1 - \bar{z}_2)^{\bar{h}_\phi}}, \tag{1.50}$$

  where $z = x + iy$. While computing correlations, $\bar{z} = x - iy = z^*$, though z and $\bar{z}$ can often be treated as independent variables. A field scaling dimension is the sum of holomorphic and antiholomorphic dimensions, $\Delta_\phi = h_\phi + \bar{h}_\phi$. We will for the most part consider spinless fields, i.e. $h_\phi = \bar{h}_\phi$.

The simplest space with a boundary is of course the half-space. In two dimensions, the study of fields on a half-plane is enough to obtain correlation functions in any sensible geometry, since one can map the upper-half plane onto a disc, and then, by the Riemann mapping theorem, perform a Schwarz-Christoffel mapping of the disc into any polygon.

To see what changes when a boundary is introduced, the first thing is to recall the Ward identity, which states the effect of an (active) infinitesimal transformation

of the coordinates on a correlation function. Using complex coordinates $(z, \bar{z})$ that transform into

$$z \to z + \epsilon(z), \qquad \bar{z} \to \bar{z} + \bar{\epsilon}(\bar{z}), \tag{1.51}$$

a field $\phi(z, \bar{z})$ transforms as

$$\phi(z) \to \phi(z) + \epsilon'(z)\Delta_\phi + \epsilon(z)\partial_z. \tag{1.52}$$

The conformal Ward identity states that a correlation function containing ϕ, $\langle X \rangle = \langle \phi(z, \bar{z}) \ldots \rangle$ transforms as

$$\delta_{\epsilon,\bar{\epsilon}} \langle X \rangle = -\oint_C \frac{dz}{2\pi i} \langle TX \rangle \epsilon(z) + \oint_C \frac{d\bar{z}}{2\pi i} \left\langle \bar{T}(\bar{z})X \right\rangle \bar{\epsilon}(\bar{z}), \tag{1.53}$$

where T is the stress-energy tensor and the integral is performed over a contour that contains all the points in the correlation function. An infinitesimal transformation is then identified with a pair of a holomorphic and a antiholomorphic functions $\{\epsilon(z), \bar{\epsilon}(\bar{z})\}$, which are independent. What happens if we now add a boundary, at $\mathrm{Im}(z) = 0$?

Our choice of transformations is limited, as we must preserve the boundary on the real axis. This means that we can no longer select ϵ and $\bar{\epsilon}$ independently, as the antiholomorphic function must be the complex conjugate of the holomorphic one: $\bar{\epsilon} = \epsilon^*$. Similarly, the antiholomorphic part of the stress-energy tensor on the upper half-plane becomes the reflection of its holomorphic part on the lower half:

$$\bar{T}(z) = T(z^*), \qquad \to \qquad T = \bar{T} \quad \text{when } \mathrm{Im}(z) = 0. \tag{1.54}$$

So far everything looks quite mathematical, but we can see the first glimpse of physical intuition: if we rewrite the condition $T = \bar{T}$ on the real axis using real (x, y) coordinates, it becomes $T_{x,y} = 0$, which means that there is no energy flux across the boundary, consistently with our constraint.

One can then apply Schwarz reflection principle on $T(z)$: a complex function, defined on the upper half-plane and with real values on the real axis, can be extended on the entire complex plane by setting

$$T(z^*) = (T(z))^*, \tag{1.55}$$

which means that its value at a point z, with $\mathrm{Im}(z) < 0$, is simply the complex conjugate of the value of its mirror image above the real axis.

Now we get to the important point [62]: with a boundary, the holomorphic and antiholomorphic parts of the Ward identity (1.53) are no longer independent;

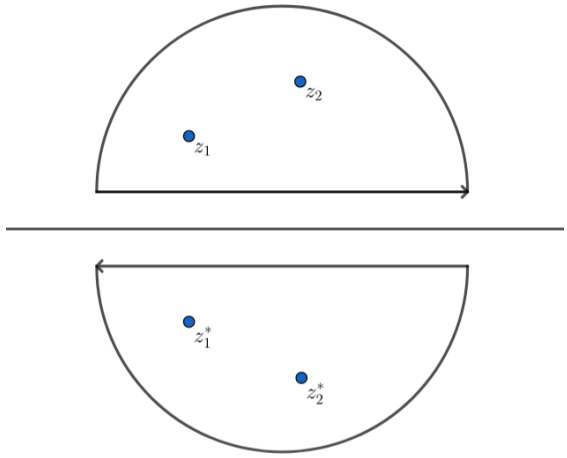

Figure 1.8: Integration contour of the points in the upper half-plane and its mirror image on the lower half-plane, which corresponds to the integral over the antiholomorphic fields. Since both paths are counterclockwise, the contributions on the real axis cancel each other out.

instead, we can use (1.55) to replace the integral over the antiholomorphic part with an integral of the corresponding holomorphic functions reflected onto the lower half-plane:

$$\delta_{\epsilon,\bar{\epsilon}} \langle X \rangle = -\oint_C \frac{dz}{2\pi i} \langle TX \rangle \, \epsilon(z) + \oint_{\bar{C}} \frac{dz}{2\pi i} \langle \bar{T}X \rangle \, \bar{\epsilon}(\bar{z}) = \oint_B \frac{dz}{2\pi i} \left\langle T\tilde{X} \right\rangle = \delta_\epsilon \left\langle \tilde{X} \right\rangle . \tag{1.56}$$

Here, C represents a contour on the upper half-plane containing all the points, which may be shaped like a half circle. The second term is an integral over the same contour, but contains the antiholomorphic parts of T and ϵ: this means it is equivalent to an integral over the mirror image of the previous contour, which surrounds the complex conjugates of the original points, as seen in Fig. 1.8.

As long as there are no fields on the real axis, the path right above the axis cancels the opposite path right below it. The two integrals then turn into a single integral over a full circle, encompassing the original points and their mirror image.

This means that any n-point correlation function on the half-plane can be computed as a $2n$-point correlation function on the entire plane:

$$G_n(z_1, \bar{z}_1; z_2, \bar{z}_2; \dots z_n, \bar{z}_n) = G_{2n}(z_1; z_1^*; z_2; z_2^*; \dots z_n; z_n^*) \tag{1.57}$$

The good news is that (ignoring boundary conditions for a second) if we know everything about a theory on the entire plane, we also know everything about that theory on the half-plane. The bad news is that most of the time, higher-order correlation functions are hard to compute, and even something as simple as a two-point function on the half-plane becomes a non-trivial four-point function on the entire space.

For now, let us see the simplest case, and the first interesting result of boundary CFT: one-point functions. We know that, in the full space,

$$\langle \phi(z_1)\phi(z_2)\rangle = \frac{C}{|z_1 - z_2|^{2h_\phi}}. \tag{1.58}$$

This means that, in the upper half-plane,

$$\langle \phi(z)\rangle_{\text{UHP}} = \langle \phi(z)\phi(z^*)\rangle = \frac{C}{(2\,\text{Im}\, z)^{2h_\phi}} = \frac{C}{(2\,\text{Im}\, z)^{\Delta_\phi}}, \tag{1.59}$$

with the last equality holding for a spinless field.

There is another important detail: while on the full space the constant C in front of two-point correlation can always be set to 1, as it simply depends on an arbitrary normalization of the fields, on a bounded system this constant also depends on the boundary conditions, something which makes finite system a very rich topic. To make it more concrete, let us for now consider the order parameter field, representing the magnetization in spin models. Imposing a choice of boundary conditions means selecting the value of the magnetization at each point of the boundary. In order to respect conformal invariance on the boundary, the value of the field has to be homogeneous. On the lattice model, this means either fixing the value of each spin to be the same, or leaving them free. These two choices are called, respectively, Fixed Boundary Conditions (FBCs) and Open Boundary Conditions (OBCs). FBCs break the symmetry of the model, by picking a preferential direction. As an example, on an $O(N)$ model one can decide to fix the boundary spins to be parallel to a given vector $\vec{r}$. Even at the critical temperature, the boundary spins contribute to an alignment of the spins in the bulk, leading to a nonvanishing magnetization, defined as $\left\langle \vec{\phi}\cdot\vec{r}\right\rangle$.

Now the role of the constant in (1.59) should be clearer: in the case of OBCs, there is no reason for the fields to "choose" to lean one way or the other, so their average is still zero: $C_{\text{OBC}} = 0$. On the other hand, in the case of FBCs the value of this constant will be nonzero, meaning that an ordered boundary at the critical point creates a profiles of the order parameter, energy density and other fields across the half-plane, which decay as a power law. From (1.59) with FBCs we also see that, in the limit $\text{Im}\, z \to 0$, $\phi(z) \to \infty$. An infinite magnetization (or other fields) on the

boundary is indeed the continuum equivalent of fixed spins on the lattice: any finite value of the field on the boundary flows under renormalization to $\phi = \pm\infty$, as it is the only scale invariant boundary condition besides $\phi = 0$.

It is worth mentioning that, despite violating translational symmetry, other kinds of boundary conditions can be studied through CFT. In particular, a change from one BC to a different one in the same boundary can be described as the action of a boundary field. Our theory, however, cannot currently describe the effect of boundary fields, so they will not be explored further.

As usual, a lot more is known in $d = 2$ compared to higher dimensions, thanks to conformal field theory. All critical exponents [71, 72, 73], as well as crossing probabilities [74], are exactly known. For this reason, simulating continuum percolation in two dimensions is mainly intended as a benchmark: it is useful to have exact results to compare to our data.

Chapter 2

Critical geometry approach

2.1 Uniformization

In the previous chapter, we reviewed some of the many important results that follow from conformal symmetry. Now let us try and see this property from a more intuitive, if somewhat heuristic, point of view.

Conformal invariance, in words so simple they would probably anger mathematicians, means that each point and each region of space has the same property as every other point or region. We can use conformal maps because we are allowed to move points around, as long as we preserve local properties. Once a boundary is introduced, however, this property is at least partly lost. As we have seen, boundary CFT then asks itself: which are the conformal transformation that can still be used? For instance, correlation functions on a half-space are no longer invariant under a translation perpendicular to the boundary, but dilations are still allowed.

The main idea in [1] is, however, somewhat different. Rather than try to obtain which transformations are allowed by the combination of conformal invariance and the presence of a boundary, the aim is now to recover a concept of homogeneity throughout a bounded domain. This, of course, seems contradictory at first: some point are close to a boundary, while others are far away. However, there is a way out: in order to quantify this distinction between points near the boundary and points deep in the bulk, one needs a way to measure distances, i.e. a metric. What if the default choice of metric, the euclidean one, was not the correct one for field theories on bounded spaces?

To be clear, the models themselves live on a flat space: the discrete models we will consider are defined on a simple cubic lattice. What is new is the idea of computing correlation as if the fields were defined on a curved space.

There are many requirements for this choice to make sense. First of all, local properties must be preserved. This means that zooming in on a small region, the metric must still appear euclidean, and it must change smoothly. This limits our choice to a metric which is in the same conformal class as the euclidean metric, i.e. it is the flat metric multiplied by a point-dependent scale function:

$$g_{ij} = \frac{\delta_{ij}}{\gamma(\mathbf{x})^2}, \tag{2.1}$$

where δ_{ij} is the euclidean metric; we chose to call this function $1/\gamma(x)^2$ so that $\gamma(x)$ takes the role of a local length scale, as will become clearer soon. Now we need further constraints to fix this function. Here is the main hypothesis in [1], which the rest of this thesis aims at providing support for:

A bounded system at criticality alters its metric so that it becomes uniform, by having constant curvature

This is what we call **uniformization**. Once the homogeneity of a model is broken by the addition of boundaries, the system "tries" to restore it by making some quantity, associated with the metric, homogeneous throughout the system. A slightly less binding formulation of the same idea would be the following: correlation functions in a bounded system can be computed using the metric that makes the curvature constant.
There are many possible measures of curvature for any given metric. As the first guess, we may pick the simplest one: the Ricci scalar curvature. To get it, first one starts from the Christoffel coefficients of the metric:

$$\Gamma^i_{jk} = \frac{1}{2} g^{il} \left(\partial_k g_{lj} + \partial_j g_{lk} - \partial_l g_{jk} \right), \tag{2.2}$$

from which one gets the Ricci tensor

$$\mathrm{Ric}_{ij} = \partial_l \Gamma^l_{ji} - \partial_j \Gamma^l_{li} + \Gamma^l_{lp} \Gamma^p_{ji} - \Gamma^l_{jp} \Gamma^p_{li}. \tag{2.3}$$

Finally, contracting the Ricci tensor with the metric gives the Ricci scalar curvature R.

$$R = \mathrm{Ric}_{ij} g^{ij}. \tag{2.4}$$

So, our hypothesis translate to $R = \kappa$. We can say something more about this constant: if we set $\kappa > 0$, we would have a system with no boundaries, such as the surface of a sphere. This is clearly not what we want; next would be the case $\kappa = 0$,

which can also be quickly discarded as it would mean going back to a flat space. We are left with $\kappa < 0$, and, without losing generality, we can set $\kappa = -d(d-1)$, since it will simplify the next equations.

To make this more concrete, we can look at the simplest space with constant negative curvature: the Poincaré half-plane. It is defined as the set of points $(x, y), x \in \mathbb{R}, y > 0$, with the metric

$$g_{ij} = \frac{\delta_{ij}}{y^2}. \tag{2.5}$$

The most immediate property of this metric is that it diverges at the boundary. This is shared by all hyperbolic metrics, and they satisfy another fundamental requirement for this theory: the distance between any point and the $y = 0$ boundary is infinite. This means that we no longer have a distinction between points close to the boundary and points far away from it, as desired.

More in general, the requirement of constant curvature can be turned into an equation for the scale factor $\gamma(x)$. To do this, the first thing is to compute the Christoffel coefficients (2.2) for our metric (2.1):

$$\Gamma^i_{jk} = \frac{1}{\gamma(x)} \left[-\delta_{i,j}\partial_k\gamma(x) - \delta_{i,k}\partial_j\gamma(x) + \delta_{j,k}\partial_i\gamma(x) \right]. \tag{2.6}$$

A small detail about the indices: during these calculation there is no need to raise or lower any index, so the only time there is a meaningful difference between high and low indices is in the metric: while $g_{ij} \propto \gamma(x)^{-2}$, the metric with raised indices is its inverse, $g^{ij} \propto \gamma(x)^2$. So if the indices in (2.6) do not seem to match, it is simply because we already replaced g_{ij} with its expression.

Now, rather than compute the entire Ricci tensor (2.3), we may compute its trace directly:

$$R = R_{ij}g^{ij} = R_{ij}\delta_{ij}\gamma^2(x) = R_{ii}\gamma^2(x), \tag{2.7}$$

and

$$\mathrm{Ric}_{ii} = \partial_l\Gamma^l_{ii} - \partial_i\Gamma^l_{li} + \Gamma^l_{lp}\Gamma^p_{ii} - \Gamma^l_{ip}\Gamma^p_{li}. \tag{2.8}$$

We can substitute (2.6) to compute each term:

$$\begin{aligned}
\partial_l \Gamma^l_{ii} &= (d-2)\left(\frac{\partial_i\partial_i\gamma}{\gamma} + \frac{\partial_i\gamma\partial_i\gamma}{\gamma^2}\right) \\
-\partial_i \Gamma^l_{li} &= d\left(\frac{\partial_i\partial_i\gamma}{\gamma} - \frac{\partial_i\gamma\partial_i\gamma}{\gamma^2}\right) \\
\Gamma^l_{lp}\Gamma^p_{ii} &= -\frac{d(d-2)}{\gamma^2}\partial_i\gamma\partial_i\gamma \\
-\Gamma^l_{ip}\Gamma^p_{li} &= \frac{d-2}{\gamma^2}\partial_i\gamma\partial_i\gamma.
\end{aligned} \tag{2.9}$$

Now we replace these derivatives with more recognizable expressions: $\partial_i\partial_i\gamma = \triangle\gamma$ and $\partial_i\gamma\partial_i\gamma = |\nabla\gamma|^2$, so that the sum of all four terms gives us

$$R = \gamma(x)^2 R_{ii} = (2d-2)\gamma\nabla^2\gamma - d(d-1)|\nabla\gamma|^2 = -d(d-1). \tag{2.10}$$

This equation, in general not particularly well-known to physicists, is known by geometers as the **Yamabe equation**. It is convenient to represent the Laplacian operators with $\triangle$, rather than ∇^2, for a reason that will become apparent later. The Yamabe equation has another, slightly more intuitive, form:

$$\boxed{(-\triangle)\gamma(x)^{-\frac{d-2}{2}} = -\frac{d(d-2)}{4}\gamma^{-\frac{d+2}{2}}.} \tag{2.11}$$

Let us start by seeing the simplest solutions to this equation, on bounded domains Ω with the boundary condition $\gamma(x) = 0$ on the boundary $x \in \partial\Omega$. For a half-space in any dimension, i.e. $x_1, \dots x_{d-1} \in \mathbb{R}^{d-1}, x_d > 0$:

$$\gamma(\mathbf{x}) = x_d. \tag{2.12}$$

So the metric is $g_{ij} = \delta_{ij}/x_d^2$. Despite the simplicity of this example, it highlights a property which is common to all the solutions of the Yamabe equation, in any domain: close to the boundary, $\gamma(x)$ is proportional to the distance to the boundary, meaning that the metric is proportional to the inverse square of this distance. For this reason,

$$\lim_{\mathbf{x}_1 \to \mathbf{x}_0 \in \partial\Omega} \mathfrak{D}_\gamma(\mathbf{x}_1, \mathbf{x}_2) = \infty, \tag{2.13}$$

which was one of our initial requirements: every point is now infinitely far away from the boundary, so there is no longer a distinction between regions close to the boundary and regions far away from it.

To give another example, which is also valid in any dimension, the solution of the Yamabe equation in a $d-$dimensional ball of radius R is simply

$$\gamma(\mathbf{x}) = \frac{R^2 - r^2}{2R}, \tag{2.14}$$

where $r^2 = \sum_{i=1}^{d} x_i^2$. Again, we see that the conformal factor vanishes linearly as one approaches the boundary $r = R$.
Now, assuming that we manage to solve the Yamabe equation for the desired domain, an obvious question follows: what do we do with it? Of course, the main goal while studying any statistical model is to compute correlation function. So let us investigate how they can be related to the solution of the Yamabe equation.

2.1.1 Correlation functions

For a rescaling of the domain Ω by a factor λ, i.e. $x \in \Omega$, $x' \in \Omega'$, $x' = \lambda x$, quasi-primary fields are known to transform as

$$\phi'(x') = \lambda^{\Delta_\phi} \phi(x). \tag{2.15}$$

This could be seen as (1.52) for the case of a finite (rather than an infinitesimal) transformation, in which $\epsilon(z) \propto z$, i.e. a dilation. It is also easy to deduce how our conformal factor $\gamma(x)$ transforms for a dilation of the system. Say we have a solution of the Yamabe equation (2.11) for the rescaled domain Ω':

$$(-\triangle_{x'})\gamma_{\Omega'}(x')^{-\frac{d-2}{2}} = -\frac{d(d-2)}{4}\gamma_{\Omega'}^{-\frac{d+2}{2}}(x'). \tag{2.16}$$

Since the Laplacian in the new coordinates is simply the Laplacian in the old coordinates divided by λ^2, the solution $\gamma_{\Omega'}$ in the new rescaled domain is related to the solution in the original domain by

$$\gamma_{\Omega'}(\lambda x) = \lambda \gamma_\Omega(x). \tag{2.17}$$

This means that the conformal factor has the role of a local length scale. In other words, $\gamma(x)$ is not a field, but if it were, it would have scaling dimension -1. Since there are in general no other quantities that could take the role of a local length scale in the system, this leads us to the first conjecture:

$$\boxed{\langle \phi(x) \rangle = \frac{\alpha}{\gamma(x)^{\Delta_\phi}}.} \tag{2.18}$$

This is the first result of the uniformization theory, which we might call "conjecture for one-point functions". It means that, if we can solve the Yamabe equation in a given domain, assuming we already know the scaling dimensions of the fields present in the theory, then all their one-point functions are completely determined, up to a field-dependent multiplicative constant α, which cannot be fixed by this approach but is in any case unimportant. We will see in the next Section how to add the effect of anomalous dimension.
This might sound too good to be true, and, as we explain in the next Section, it is. For the moment, let us start by looking at a first example where Eq. (2.18) reproduces a known result from boundary CFT. We have seen that in a half-space, $\gamma(\mathbf{x}) = x_d$ (2.12). Using this, the Yamabe approach recovers Eq. (1.59):

$$\langle \phi(\mathbf{x}) \rangle = \frac{\alpha}{x_d^{\Delta_\phi}}. \tag{2.19}$$

While not a new result, this gives us a hint that we are heading in the correct direction. It should be noted that this is not limited to $d = 2$, since the solution (2.12) is valid in any dimension. In this and in any other example, one can see that $\langle \phi(x) \rangle \to \infty$ for x approaching a boundary. This is a consequence of our choice of boundary conditions for the Yamabe problem, i.e. $\gamma(x) = 0$ on the boundaries. As mentioned in Chapter 1, this theory is suited to models with fixed boundary conditions.
Now one might want more: we have one-point function, can we get two-, three-, N-point functions? The first thing we can say is that higher-order correlation functions need to have the correct dimensions: this means adding a factor $\gamma(\mathbf{x}_i)^{-\Delta_\phi}$ for each point $\mathbf{x}_i$. By itself, this would be the limit of the correlation function when each point is very far from every other point: simply the product of one-point functions. But then, of course, we need to include a function which captures the actual correlation between points,

$$\langle \phi(\mathbf{x}_1) \dots \phi(\mathbf{x}_n) \rangle = \frac{1}{\gamma(\mathbf{x}_1)^{\Delta_\phi}} \dots \frac{1}{\gamma(\mathbf{x}_n)^{\Delta_\phi}} F(x_1, \dots, x_n), \tag{2.20}$$

for some unknown function F of the points. There is more we can say, however: this function cannot depend on each point separately, since the contribution from one-point functions has already been factored out: what matters is the interaction between these points, so F must be a function of the distances between each pair of points. Following this idea of uniformization, we come to our second conjecture: **correlation functions on critical bounded domains depend on the distances between points computed using the metric which solves the**

corresponding Yamabe equation. The idea is that the system has, in a sense, forgotten about its original euclidean metric, and now behaves according to the new curved metric. Therefore, distances between points are the lengths of geodesics according to the introduced metric. So, for example, for two-point functions, we have

$$\boxed{\langle\phi(\mathbf{x}_1)\phi(\mathbf{x}_2)\rangle = \frac{1}{\gamma(\mathbf{x}_1)^{\Delta_\phi}}\frac{1}{\gamma(\mathbf{x}_2)^{\Delta_\phi}}\mathcal{F}\left(\mathfrak{D}_\gamma(x_1,x_2)\right)}, \tag{2.21}$$

where $\mathcal{D}_\gamma$ is the distance computed using $g = \delta/\gamma^2(\mathbf{x})$. Even without completely fixing higher-order correlation function, this conjectures imposes a tight constraint on them. In the next chapters we will see how this conjecture can be tested on numerical data.

2.1.2 Anomalous dimension

There are some complications, which lead to important features, that we dodged so far: the formulation just presented cannot be complete. To get a hint of where the Yamabe equation might come from, let us look again at the physicist version of it (2.11): the exponent of γ on the left-hand side, $\frac{d-2}{2}$, is the same as the scaling dimension of the order parameter field for a theory at the upper critical dimension $d = d_c$:

$$\Delta_\phi = \frac{d-2}{2} \qquad \to \qquad \langle\phi(x)\rangle \propto \gamma^{-\frac{d-2}{2}}. \tag{2.22}$$

This means that the Yamabe equation can be rewritten in terms of the order parameter one-point function in place of γ. For simplicity and since we will for the most part deal with spin models, we can call this average the magnetization profile $m(x)$:

$$\langle\phi(x)\rangle = m(x). \tag{2.23}$$

What we get is

$$\triangle m(\mathbf{x}) = g\frac{d(d-2)}{4}m(\mathbf{x})^{\frac{d+2}{d-2}}. \tag{2.24}$$

This equation is not as alien as the original Yamabe equation (2.10): for example, setting $d = 4$ we get $\triangle m \propto m^3$. In general, this is the saddle-point equation for the action of a scalar or on $O(N)$ theory with marginal potential at the critical point $\mu = 0$:

$$S = \int d^d x \left[-\frac{1}{2}\phi(x) \triangle \phi(x) + \frac{\mu^2}{2}\phi(x)^2 + g\, c_d\, (\phi^2)^{\frac{d}{d-2}} \right], \tag{2.25}$$

The factor in the interaction constant,

$$c_d \equiv \frac{(d-2)^2}{8}, \tag{2.26}$$

has been chosen to reproduce (2.24). The connection between the mean field Landau-Ginzburg equations and the Yamabe equation, which arrives at the Hilbert-Einstein action functional, is presented in [75].
Indeed, taking the functional derivative of (2.25) with respect to the field ϕ and setting it to zero, i.e. taking its saddle point, reproduces the Yamabe equation written for the order parameter rather than for γ:

$$\frac{\partial S}{\partial \phi} = 0 \quad \rightarrow \quad \triangle\phi = g\frac{d(d-2)}{4}\phi^{\frac{d+2}{d-2}}. \tag{2.27}$$

This is nice as it connects the Yamabe equation to something more physical and better known, but it also means that the Yamabe equation can only be valid for model whose critical behavior is correctly described by a mean-field model, i.e. models at the upper critical dimension. These models, however, are too simple to be interesting: if we could only study them, the uniformization approach would be quite disappointing.
One of the main features of critical models below the upper critical dimension is the appearance of nontrivial scaling dimensions for the fields in the theory. As an example, the scaling dimension of the spin field of the three-dimensional Ising model is known to be $\Delta_\phi = 0.518149(10)$ from Conformal Bootstrap, currently the most precise method to obtain various critical exponents. This quantity differs from its "engineering" dimension $\frac{d-2}{2} = 0.5$, by an apparently small but very meaningful amount, called the anomalous dimension η. To be more specific, the critical exponent η is defined from the scaling of two-point functions on the full space, i.e.,

$$\langle \phi(x)\phi(y) \rangle = \frac{\alpha}{|x-y|^{2\Delta_\phi}} = \frac{\alpha}{|x-y|^{d-2+\eta}}. \tag{2.28}$$

The anomalous dimension $\eta = 2\Delta_\phi + 2 - d$ quantifies how much the scaling of a field differs from what we would expect by naive power counting.
So we need to find a way to modify the Yamabe equation in order to account for the anomalous dimension. To see one possible way, let us start from rather far away: consider a simple field theory, quadratic in the field ϕ:

$$S = -\int d^d x \left(\frac{1}{2}\phi(x) A\phi(x) + h(x)\phi(x)\right), \tag{2.29}$$

for some generic positive definite operator A (we are of course thinking of $-\triangle$), and h is an external field. Correlation functions of the field are easily computed, in particular

$$\langle\phi(x)\rangle = A^{-1}h(x). \tag{2.30}$$

So

$$A\langle\phi(x)\rangle = h(x). \tag{2.31}$$

This is quite similar to the Yamabe equation in the form (2.11): in particular, if we have a length scale $\gamma(x)$, we expect $\langle\phi\rangle \propto \gamma^{-\frac{d-2}{2}}$, and the magnetic field h has scaling dimension $\frac{d+2}{2}$, so it can also be expressed as $\gamma^{(d+2)/2}$. If we also set $A = -\triangle$, we get

$$(-\triangle)\gamma(x)^{-\frac{d-2}{2}} \propto \gamma^{-\frac{d+2}{2}}, \tag{2.32}$$

which is exactly the Yamabe equation. But if the scaling dimension of the field differs from $\frac{d-2}{2}$, we would get a different equation! The question is now: is there a way to modify the Yamabe equation which can account for $\eta \neq 0$, and at the same time preserves some geometrical interpretation?
The first thing we can do is change the exponent on the left-hand side of (2.11) to $\frac{d-2+\eta}{2} = \Delta_\phi$. To maintain the correct scaling, let us look at the second term in Eq. (2.29): since the dimensions of ϕ and h must add to d, the scaling dimension of h must be $d - \Delta_\phi$. By replacing the exponent $\frac{d+2}{2}$ with $d - \Delta_\phi$ on the right-hand side of (2.11), we get

$$(-\triangle)\gamma(x)^{-\Delta_\phi} = -\frac{d(d-2)}{4}\gamma^{-d+\Delta_\phi} \qquad ? \tag{2.33}$$

The problem with this equation is that the two sides do not scale in the same way. To fix this, we need to change the dimension of the laplacian operator itself, to $(-\triangle)^{\frac{d}{2}-\Delta_\phi}$, and we end up with the **fractional Yamabe equation** (the multiplicative constant is unimportant):

$$\boxed{(-\triangle)^{\frac{d}{2}-\Delta_\phi}\gamma(x)^{-\Delta_\phi} = k\gamma^{-d+\Delta_\phi}.} \tag{2.34}$$

We will call the exponent of the laplacian s for convenience, but this does not address the elephant in the room: what is this operator? Does it even mean anything? To answer this, we need a rather long mathematical detour.

2.2 Fractional laplacian

To define the problem slightly better, the two questions we need to answer are: how is the fractional laplacian operator $(-\triangle)^s$ defined? And how do we solve a differential equation containing such operator?
Let us start by guessing some intuitive definition. By the definition of a derivative, it looks like something that can only be performed an integer number of times: asking to compute half a derivative of a function does not seem to make any sense. So, as is commonly done when trying to extend a definition (think of the case of analytic continuation), we can take a property of the original operator, and make it the definition of the generalized operator. We know that the Fourier transform (from x-space to k-space) of the derivative of a function is simply the Fourier transform of that function multiplied by k, and in general

$$\mathcal{F}\left[\frac{\mathrm{d}^n}{\mathrm{d}x^n}f\right](k) = k^n \mathcal{F}[f](k). \tag{2.35}$$

In more than one dimension, the same is valid for the usual laplacian:

$$\mathcal{F}\left[-\triangle f\right](k) = k^2 \mathcal{F}[f](k). \tag{2.36}$$

This should clarify why we take powers of the negative laplacian: $\triangle$ is a negative definite operator, but we want to deal with a positive definite one if our goal is to compute non-integer powers of it. So, we can generalize Eq. (2.36) into

$$\mathcal{F}\left[(-\triangle)^s f\right](k) = k^{2s} \mathcal{F}[f](k). \tag{2.37}$$

And this is indeed one possible definition of the fractional laplacian. There are surprisingly many others, and it can be shown [76] that in the full space they are all equivalent. An example of an alternative definition comes from the use of an "incremental ratio", like the ones used in the definition of regular derivatives, but with the difference that an integral over the entire space is necessary, thus losing the property of locality typical of integer derivatives:

$$(-\triangle)^s f(x) = c_{d,s} \int \frac{f(x) - f(y)}{|x-y|^d + 2s} dy, \tag{2.38}$$

where $c_{d,s} = \frac{4^s \Gamma(d/2+s)}{\pi^{d/2}\Gamma(-s)}$ is a constant added so that this definition matches the previous one (and reduces to the integer laplacian in the limit $s \to 1$).
For a more rigorous and more thorough explanation, [77] is an entire book on fractional laplacian. If, on the other hand, one wants some physical intuition, there is a rather simple example where fractional derivatives appear: anomalous diffusion. We know that the continuum limit of a stochastic process where a random walker jumps left or right one step at a time is a diffusion equation, with the usual second derivative. The same happens if the jumps follow a short-tailed distribution. If, however, the distribution has long tails and infinite variance, there is still a way to write a master equation for the probability density of the walker, but this time using a fractional laplacian.
There is, however, a rather thorny issue: all these definitions are only equivalent if the function and the integrals are defined on the whole space. But the entire point of the uniformization approach is to treat finite domains! Out of the various definitions found in [76], it turns out that the last one, introduced in [78], is the correct one for our purposes. It relies on extending our domain into a $d+1$-dimensional space, of which the original domain is just the boundary[1]. To illustrate this technique, let us start from the simplest non-integer power, $s = 1/2$.

2.2.1 Fractional laplacian as an extension problem

We want to compute the square root of the laplacian, $(-\triangle)^{1/2}$, of a function $f(\mathbf{x})$ defined on a domain Ω. To do so, we define a $d+1$-dimensional space $\Theta = \Omega \times \mathbf{R}^+$ by adding an auxiliary variable y. The original domain Ω is recovered for $y = 0$, as seen in Fig. 2.1. On the extended domain Θ, we need to define a function $u(\mathbf{x}, y)$ which satisfies both these properties:

- u is harmonic, i.e.
$$\triangle_{(d+1)} u(\mathbf{x}, y) = \triangle_d u + \partial_y^2 u = 0 \tag{2.39}$$
- f is the Dirichlet boundary condition of u: $u(x, 0) = f(x)$.

If we can find such a function, then the square root of the laplacian of f is simply

[1]To be slightly less sloppy, in principle our domain Ω cannot be the boundary of some space, since Ω itself must have a boundary, and the boundary of a boundary is the empty set. Nevertheless, since the extended space can be seen as infinite slices of Ω, the original space is simply the first of those slices. Basically, if the extended space is a salami, the original space is one slice, and the physical boundary is the skin of one salami slice.

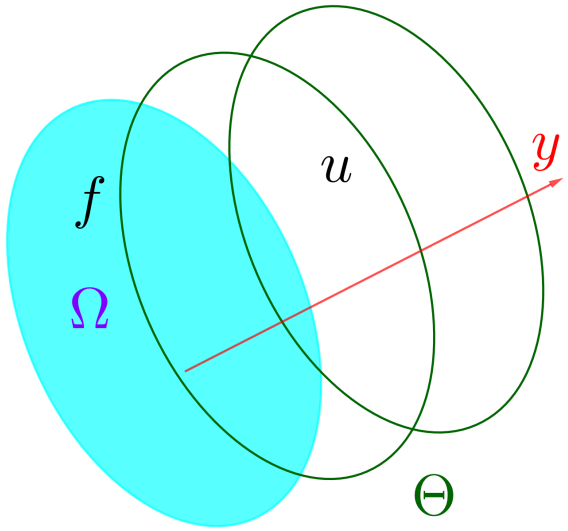

Figure 2.1: The original space Ω extended through the variable y. f is defined on Ω, u is defined on the entire space Θ.

$$(-\triangle)^{1/2} f(\mathbf{x}) = -\partial_y u(\mathbf{x}, y)\Big|_{y=0}, \tag{2.40}$$

because applying $(-\triangle)^{1/2}$ twice must equal to the integer laplacian. Indeed,

$$(-\triangle)^{1/2}(-\triangle)^{1/2} f(x) = \partial_y^2 u\Big|_{y=0} = -\triangle_d u = -\triangle_d f, \tag{2.41}$$

where in the second equality we used Eq. (2.39) and in the last one the boundary condition.
So we can see $(-\triangle)^{1/2}$ as a Dirichlet to Neumann operator: we start by defining a function with known values on the boundary, and we end by obtaining the square root of the laplacian of our function by reading the derivative of the extended function on the same boundary. Other powers of the laplacian are computed in a rather similar way, except that the requirement on u slightly changes. In general, for $0 < s < 1$, one needs

$$\begin{cases} \triangle_d U + \frac{1-2s}{y}\partial_y U + \partial_y^2 U = 0 \\ U(x,0) = f(x), \end{cases} \tag{2.42}$$

to get

$$(-\triangle)^s f = \frac{2^{2s-1}\Gamma(s)}{s\Gamma(-s)} \lim_{y\to 0} y^{1-2s}\partial_y U. \tag{2.43}$$

as proven in [78]. One way to see how a non-local problem in d dimensions can be turned into a local problem in $d+1$ dimensions is by looking back at the random walker analogy. A walker performing long jumps in one dimension can be seen as a walker performing short jumps in two dimensions: as it occasionally intersects the x axis, we can see the set of short 2d jumps between one intersection and the next as a single long 1d jump [79].

2.2.2 Fractional Laplacian as a scattering operator

Our case follows the same idea as the example above, but with some additional layers of mathematical complexity due to the presence of a curved metric on the original space Ω. To be specific, Ω must be a Riemannian manifold, i.e. a smooth manifold with a positive-definite metric g defined on its tangent space. This means that the extended space Θ must also include a non-trivial metric.
In the most general case, introduced in [80], the extended domain would not simply be a cartesian product of the original domain and an auxiliary variable, so identifying the boundary is more subtle. To do so, one introduces a so-called defining function $\rho(X)$ such that $\rho(X) > 0$ in the bulk (for $X \in \Theta \setminus \Omega$), vanishes on the boundary $\rho(X) = 0$ for $X \in \Omega$, and is regular on the boundary $d\rho \neq 0$ on Ω. In our case, we can simply select $\rho(X) = y$, the same auxiliary coordinate as the previous case.
The actual method we use to compute the fractional laplacian is not quite the one introduced by Caffarelli and Silvestre mentioned above, but rather it uses what is known as a scattering operator. The reader may now wonder why I reported all these other definitions of fractional laplacians since they do not seem relevant to our case: simply put, I found the definition below completely obscure without some preliminary explanation. This may not be the case for others, but I can hope this approach may be clearer. To recap, so far we have first introduced the fractional laplacian through the most intuitive definition, i.e. through the Fourier transform, and with an equivalent definition as a sort of integral of an incremental ratio that highlights its non-local nature. Next we have seen how a non-local problem in d dimensions can turn into a local problem in $d+1$ dimensions. Now we see a different definition which also exploits this increase in dimensionality, and we can prove it is equivalent to (2.42) in at least one case.

Following [81], to compute the fractional laplacian of a function f, we want to solve an eigenvalue problem for the integer laplacian $\triangle_{g_+}$ in the extended space Θ with metric $g+$, i.e. we want to find a function u such that

$$-\triangle_{g_+} u = s(d-s)u. \tag{2.44}$$

In particular, we are after a solution which, for a pair of functions F_I and F_O, takes the form

$$u = F_I y^{\Delta_\phi} + F_O y^{d-\Delta_\phi}, \qquad \text{with} \qquad F_I\Big|_{y=0} = f. \tag{2.45}$$

So the function f acts as boundary conditions for the problem. (As a reminder, s is the exponent of the fractional laplacian and $\Delta_\phi = d/2 - s$). If we can find such a solution, then we can define the scattering operator $S(s)$ as

$$S(s)f = F_O\Big|_{y=0}. \tag{2.46}$$

The scattering operator is almost the fractional laplacian, we just need to multiply by the appropriate constant:

$$P_s = 2^{2s}\frac{\Gamma(s)}{\Gamma(-s)}S(s). \tag{2.47}$$

We call the conformal fractional laplacian P_s to distinguish it from the fractional laplacian on flat space $(-\triangle)^s$. Of course, when $g_{ij} = \delta_{ij}$, $P_s = (-\triangle)^s$.
The name P comes from the Paneitz operator [82], which the conformal fractional laplacian generalizes: the Paneitz operator corresponds to P_2. The case $s = 1$ gives a slightly more familiar result:

$$P_1 = -\triangle + \frac{d-2}{4(d-1)}R, \tag{2.48}$$

which is the conformal laplacian. Still, for $s \neq 1$ there does not seem to be any reason why this operator should match the definition of fractional laplacian from Section 2.2.1. There is at least one important case in which we can confirm they are equivalent: when the extended space is a hyperbolic space, i.e.,

$$g_+ = \frac{dx_i^2 + dy^2}{y^2}, \tag{2.49}$$

where x_i, $i = 1 \dots d$ are the physical coordinates and y is the extension coordinate. To prove this, following [81], we start from the definition of conformal laplacian in $d+1$ dimensions:

$$L_{g_+} = -\triangle_{g_+} + \frac{d-1}{4d} R_{g_+}. \tag{2.50}$$

Since the extended system is a hyperbolic space, the Ricci curvature is known to be a negative constant: in particular,

$$R_{g_+} = -d(d+1). \tag{2.51}$$

Now we want to replace the "standard" laplacian in Eq. (2.44) with the conformal laplacian, since it transforms nicely under conformal transformations. we get

$$-L_{g_+} u = (s^2 - \frac{1}{4})u. \tag{2.52}$$

The hyperbolic metric is related to the flat euclidean metric by

$$g_{\text{eu}} = y^2 g_+, \tag{2.53}$$

which is a conformal transformation, under which the conformal laplacian transforms as

$$L_{g_+} f = y^{\frac{d+3}{2}} L_{g_{\text{eu}}}(y^{-\frac{d-1}{2}} f), \tag{2.54}$$

and of course the conformal laplacian for the euclidean metric is the "usual" laplacian, i.e.

$$L_{g_{\text{eu}}} = \triangle = \partial_x^2 + \partial_y^2. \tag{2.55}$$

Now, if we assume we have a solution u to (2.44) in the form (2.45), we can define

$$U = u y^{-\Delta_\phi} \tag{2.56}$$

and substitute it and Eq. (2.54) in Eq. (2.44), we get

$$\triangle_d U + \frac{1-2s}{y} \partial_y U + \partial_y^2 U = 0, \tag{2.57}$$

which is indeed (2.42). So the solution to the scattering problem is quite easily related to the solution of the Caffarelli-Silvestre extension problem, through Eq. (2.56). We still need to show how the function F_O contained in u (Eq. (2.45)) is the fractional laplacian of F_I. To do so, we can expand both in series of y:

$$F_I(x,y) = f(x) + f_2(x) y^2 + O(y^3), \qquad F_O(x,y) = p(x) + p_2(x) y^2 + O(y^3). \tag{2.58}$$

Which now means, by definition of the scattering operator, $S(s)f = p$. We also know that

$$U = y^{-\Delta_\phi} u = F_I + F_O y^{d-2\Delta_\phi} = F_I + F_O y^{2s}. \tag{2.59}$$

So now we can take the limit (2.43), $\lim_{y\to 0} y^{1-2s}\partial_y U$, and, up to multiplicative constants, using Eqs. (2.58) and (2.59), we get $F_O(x, y = 0)$, which proves that the value of the "output" function on the boundary is the fractional laplacian of the "input" function.
It may be helpful to slow down for a moment and think what we got so far: we started by the most intuitive definition of fractional laplacian, using Fourier transform. That does not tell us much, so we look for an equivalent definition, expressed as an integral: this suggests that it is a nonlocal operator. In the next step (Section 2.2.1), we find that we can turn a nonlocal problem in d dimensions into a local problem in $d + 1$ dimensions). We also see how our operator basically uses as input a Dirichlet problem and spits out a Neumann problem. This is still, sadly, not the correct definition for our purposes, but with each step we learned something more.
Finally, we find the definition we are looking for, which is again based on an extension to a $d + 1$-dimensional space and recycles the idea of Dirichlet-to-Neumann operators, but this time it uses scattering operators. I was tempted to start off with this definition, but that would have probably been incomprehensible by itself.

2.2.3 Fractional Q-curvature

The next problem is that the original Yamabe equation had a clear geometric meaning: finding the metric that makes the scalar curvature constant. Does the fractional Yamabe equation (2.34) have a similar meaning?
An important point to notice is that the equation now depends directly on the exponent Δ_ϕ, so rather than a single solution valid for any model in a given geometry, we are looking for a metric specific for one model (and therefore the corresponding scaling dimension of its order parameter field, for now) in one geometry. This may seem demotivating, as we cannot have a one-size-fits-all solution, but it actually makes more physical sense: for instance, the Ising model and the XY model, placed in, say, a $3d$ wedge, will have different correlations functions since they are different models, and we should therefore expect them to be described by different metrics. So, if the fractional Yamabe equation is to have any kind of meaning, it has be related to some measurement of curvature that also

depends on a parameter s. The answers comes in the form of a rather esoteric kind of curvature, called fractional Q-curvature, defined by applying the conformal fractional laplacian P_s to a constant [83]:

$$Q_s = P_s(\mathbb{1}). \tag{2.60}$$

As the name suggests, P_s transforms nicely under conformal changes of the metric, i.e. for

$$g \to g' = \frac{g}{w^2}, \tag{2.61}$$

where $w(x)$ is an arbitrary function, P_s changes as

$$P_s^{(g')}(w^{\Delta_\phi}\psi) = w^{d-\Delta_\phi} P_s^{(g)}(\psi), \tag{2.62}$$

where ψ is some function on which P_s acts. These exponents are the same as the ones that appear in Eq. (2.34), which is a good sign. In fact, if we rewrite the fractional Yamabe equation for a new metric g', we get

$$P_s^{(g')} \left(\frac{\gamma}{w}\right)^{-\Delta_\phi} = k \left(\frac{\gamma}{w}\right)^{-d+\Delta_\phi}. \tag{2.63}$$

This means we can pick $w(x) = \gamma(x)$ and the equation simplifies considerably:

$$P_s^{(g')}\mathbb{1} \propto \mathbb{1}. \tag{2.64}$$

So in the appropriate metric, the conformal fractional laplacian is the operator that, when acting on a constant field, produces a constant field. Finally, remembering Eq. (2.60), we obtain

$$Q_s \propto \mathbb{1}. \tag{2.65}$$

This seems too simple to give any insight, but it is actually the geometric interpretation for the fractional Yamabe equation that we were looking for! While a solution of the integer equation is a metric that makes the scalar curvature R constant, the solution of the fractional equation for an exponents $s = d/2 - \Delta_\phi$ is a metric that renders constant the corresponding fractional Q-curvature Q_s.
This concludes the mathematical detour on the definition of the fractional Laplacian. Some more specific details on how the fractional Yamabe problem can be solved in practice in our case are in Appendix 8.1.
Now that we understand the integer and the fractional Yamabe equations, we can see how effectively their solutions can describe bounded critical systems.

Chapter 3

Two dimensions

3.1 Liouville equation

The two-dimensional case is a good starting point for two reasons: first of all, the fractional Yamabe equation reduces to its integer version in two dimensions, since the constraint of constant scalar curvature also makes every other measure of curvature constant. Secondly, when exploring some new idea, it is always extremely helpful to see if it can recover some known results, before venturing into new territory. Indeed, as we are going to discuss in this Chapter, the critical geometry approach in two dimensions reproduces known results from boundary CFT.

To see what the Yamabe equation looks like in two dimensions, however, one cannot plug $d = 2$ into the equation directly; rather, a limit has to be performed:

$$\begin{aligned}
&\lim_{d\to 2}\left(\frac{4}{d(d-2)}\triangle\,\gamma(x)^{-\frac{d-2}{2}}\right)=\lim_{d\to 2}\gamma(x)^{-\frac{d+2}{2}}\\
&\lim_{d\to 2}\left(\frac{2}{d-2}\nabla\cdot\nabla e^{-\frac{d-2}{2}\log\gamma(x)}\right)=\gamma(x)^{-2}\\
&\lim_{d\to 2}\left(\triangle\log\gamma(x)e^{-\frac{d-2}{2}\log\gamma(x)}+(d-2)\left(\nabla\log\gamma(x)\right)^2 e^{-\frac{d-2}{2}\log\gamma(x)}\right)=\gamma(x)^{-2}\\
&\triangle\log\gamma(x)=-\gamma^2(x)
\end{aligned}\tag{3.1}$$

This is the Liouville equation, which is much more famous in physics than the more general Yamabe equation.

The most immediate check is to verify that $\gamma(z) = \mathrm{Im}z$ satisfies the Liouville equation, meaning that the equation for one-point function on the half-plane (1.59) is recovered. The half-plane can then be mapped to other domains, and solving the

Liouville equation in those domains is equivalent to finding the map $w(z)$ from the half-plane Z to the new space W, under which the fields transform as

$$\langle \phi(w) \rangle = \left(\frac{dw}{dz} \right)^{-h_\phi} \left(\frac{d\bar{w}}{d\bar{z}} \right)^{-\bar{h}_\phi} \langle \phi(z(w)) \rangle \,. \tag{3.2}$$

By comparing this to Eq. (2.18), we see that the scale function γ can be derived from the map $w(z)$ as

$$\gamma(w) = \mathrm{Im}(z(w)) \left| \frac{dz}{dw} \right|^{-1} . \tag{3.3}$$

We can now see a few specific cases of domains which can be mapped to the half-plane, which lead us to the solution of the Liouville equation in those domains without needing to solve the differential equation directly.

3.1.1 Liouville equation on a strip

The map from the upper half plane z to the strip $0 < \mathrm{Re}(w) < L$ is

$$w(z) = \frac{L}{i\pi} \log z, \tag{3.4}$$

so its inverse is

$$z(w) = e^{i\frac{\pi}{L}w}. \tag{3.5}$$

From this and Eq. (3.3), we get

$$\gamma(w) = \frac{L}{\pi} \sin\left(\frac{\pi}{L} \mathrm{Re}\, w \right). \tag{3.6}$$

As expected, the conformal factor only depends on the distance from the bottom edge of the strip $x = \mathrm{Re}w$, so that

$$\frac{d^2}{dx^2} \log \gamma(x) = -\frac{\pi^2}{L^2 \sin^2(\pi x/L)} = -\gamma(x)^2 \tag{3.7}$$

For a strip centered in the origin, $-1 < x < 1$,

$$\gamma(x) = \frac{2}{\pi} \cos\left(\frac{\pi}{2} x \right). \tag{3.8}$$

3.1.2 Liouville equation on a circle

The map from the upper half plane to a unit circle is a Möbius transformation

$$w(z) = \frac{2i}{i+z} - 1, \qquad z(w) = \frac{2i}{1+w} - i, \tag{3.9}$$

which leads to

$$\gamma(w) = \frac{1-|w|^2}{2} \tag{3.10}$$

This is the only solution that is also valid in higher dimensions, thanks to the fact that Möbius transformations are conformal even for $d > 2$.

3.1.3 Liouville equation on an annulus

An annulus of radii R_1 and $R_2 > R_1$ is topologically different from a half plane, so this time we will need to start from a strip $-1 < \mathrm{Re}\, z < 1$ with periodic boundary conditions in the imaginary direction, and use the map

$$w(z) = \sqrt{R_1 R_2} \exp\left(\frac{z}{2} \log \frac{R_2}{R_1}\right), \qquad z(w) = \frac{2}{\log \frac{R_2}{R_1}} \log \frac{w}{\sqrt{R_1 R_2}}. \tag{3.11}$$

From this we obtain

$$\gamma(w) = \frac{2}{\pi} \cos\left(\frac{\pi}{2} \mathrm{Re}(z(w))\right) \left|\frac{dz}{dw}\right|^{-1}, \tag{3.12}$$

which in turn gives

$$\gamma(w) = \log\left(\frac{R_2}{R_1}\right) \frac{|w|}{\pi} \cos\left(\frac{\pi}{\log(R_2/R_1)} \log \frac{|w|}{\sqrt{R_1 R_2}}\right). \tag{3.13}$$

The factor γ only depends on the radial distance $|w|$, and vanishes at both boundaries, as expected.

3.2 Correlation functions in 2d

So far we have seen that the Liouville equation can be solved in a few domains and its solution gives the correct behavior for one-point functions. Now we want do something more general, without specifying a domain and which is also valid for

two-point functions. Let us assume we have already solved the Liouville equation for a given geometry Z (like the half-plane, which is easy), obtaining $\gamma_Z(z)$. From that, we determine two-point functions on that geometry, up to a function $\mathcal{F}$ of the hyperbolic distance. Now we want to determine the same two-point function but for fields on a different domain W, which is related to the original one by a conformal map $z(w)$.

Hypotheses

- $\triangle \log \gamma(z) = -\gamma(z)^2$
- On the space Z,

$$\langle \phi(z_1)\phi(z_2)\rangle = \frac{\mathcal{F}(\mathfrak{D}_Z(z_1,z_2))}{\langle \phi(z_1)\rangle \langle \phi(z_2)\rangle} \tag{3.14}$$

What we want to prove is

Thesis

$$\langle \phi(w_1)\phi(w_2)\rangle = \frac{\mathcal{F}(\mathfrak{D}_W(w_1,w_2))}{\langle \phi(w_1)\rangle \langle \phi(w_2)\rangle} \tag{3.15}$$

Proof

First of all, we notice that the solution $\gamma_Z(z)$ transforms nicely for conformal maps, as it behaves like a local length scale:

$$\gamma_W(w) = \frac{\partial w}{\partial z}\gamma_Z\left(z(w)\right) \tag{3.16}$$

Quasi-primary fields are known to transform [70] as

$$\langle \phi(w_1)\rangle = \left(\frac{\partial w}{\partial z}\right)^{-\Delta_\phi}_{w_1} \langle \phi(z_1)\rangle\,, \tag{3.17}$$

$$\langle \phi(w_1)\phi(w_2)\rangle = \left(\frac{\partial w}{\partial z}\right)^{-\Delta_\phi}_{w_1} \left(\frac{\partial w}{\partial z}\right)^{-\Delta_\phi}_{w_2} \langle \phi(z_1)\phi(z_2)\rangle\,. \tag{3.18}$$

Substituting both into (3.14), the factors in front cancel out, so

$$\langle \phi(w_1)\phi(w_2)\rangle = \frac{\mathcal{F}(\mathfrak{D}_Z(z_1,z_2))}{\langle \phi(w_1)\rangle \langle \phi(w_2)\rangle}. \tag{3.19}$$

The thesis is now

$$\mathfrak{D}_Z(z_1, z_2) = \mathfrak{D}_W(w_1, w_2) \tag{3.20}$$

where $w_1 = w(z_1)$, $w_2 = w(z_2)$. For $z_1 = z_2$ the distances vanish and the equality is satisfied. So we can just prove

$$\partial_z \mathfrak{D}_Z(z, z_2) = \partial_z \mathfrak{D}_W(w(z), w_2). \tag{3.21}$$

By definition of distance, the l.h.s is just $1/\gamma(z)$. The r.h.s is

$$\partial_w \mathfrak{D}_W(w, w_2) \frac{\partial w}{\partial z} = \frac{1}{\gamma_W(w)} \frac{\partial w}{\partial z}. \tag{3.22}$$

This means we just have to prove

$$\gamma_W(w) = \frac{\partial w}{\partial z} \gamma_Z(z(w)), \tag{3.23}$$

which is exactly (3.16), proving (3.15). At first, I though I was heading the wrong direction when I encountered (3.21): conformal transformations are known to preserve angles, not distances! The catch is that our measuring tape is also changing accordingly: as we dilate distances, γ gets dilated by the same amount, so that the new distance measured with the metric is the same.
The nice thing about this is that not only can we determine correlations in any distance by knowing them in one geometry, but the function $\mathcal{F}$ remains the same. It is quite likely that a result like this was already proven without the use of the Yamabe equation, but I could not find it, and I consider this a rather cute proof.
So far we have seen that the conjecture for one-point function is consistent with the predictions of CFT, for any geometry in $d = 2$ and for any d on a half-space or a sphere. Now we would like to see a case which verifies the conjecture for two-point functions (2.21). As we have seen in Section 1.4, a two-point function on a half-space is equivalent to a four-point function on the whole space, so they are not exactly trivial to compute. Luckily, as usual, the Ising model comes to our aid: the two-point function for the Ising model on a half-plane $x > 0$, with diverging magnetization at the boundary, is known to be [70]:

$$\langle \phi(\{x, y\}) \phi(\{x', 0\}) \rangle = \frac{\alpha^2}{(x\, x')^{1/8}} \sqrt{\tau^{1/4} + \tau^{-1/4}}, \qquad \tau = \frac{y^2 + (x + x')^2}{y^2 + (x - x')^2}, \tag{3.24}$$

where α is a constant. This clearly contains the product of one-point functions $\langle \phi(\{x, y\}) \rangle = \alpha\, x^{-1/8}$, so we just need to show that τ is a function of the hyperbolic distance between the two points. The hyperbolic distance is

$$\mathfrak{D}\big(\{x,y\},\{x',0\}\big) = 2\,\mathrm{arcsinh}\left(\frac{1}{2}\sqrt{\frac{(x-x')^2+y^2}{x\,x'}}\right), \tag{3.25}$$

so $\tau = \coth^2(\mathfrak{D}/2)$. This means that (3.24) is in the form (2.21). In particular, while in the general case the function of the distance that appears in Eq. (2.21) is unknown, for this case we can conclude that

$$\mathcal{F}(\mathfrak{D}) = \sqrt{\left(\coth\frac{\mathfrak{D}}{2}\right)^{1/2} + \left(\coth\frac{\mathfrak{D}}{2}\right)^{-1/2}} \tag{3.26}$$

Finally, we can conformally map the half-plane into a strip $0 < x_1, x_2 < L$, and obtain a result which is still in the form (2.21):

$$\langle\phi(x_1,y)\phi(x_2,0)\rangle = e^{-\frac{2\pi}{L}(x_1+x_2)}\frac{1}{\sqrt{2}}\frac{1+\sqrt{\frac{\cosh\frac{\pi}{L}y-\cos\frac{\pi}{L}(x_1+x_2)}{\cosh(\pi y/L)-\cos\frac{\pi}{L}(x_1-x_2)}}}{\left(\frac{\cosh\frac{\pi}{L}y-\cos\frac{\pi}{L}(x_1+x_2)}{\cosh(\pi y/L)-\cos\frac{\pi}{L}(x_1-x_2)}\right)^{1/4}} \tag{3.27}$$

We can also check that for large parallel distance, the correlation decays exponentially, while for $y = 0$ and x_1 close to x_2, it diverges as $(x_1 - x_2)^{-1/2}$, in agreement with [70].

3.3 A numerical example: the Ising model

In the next chapter, we will compare predictions of the fractional Yamabe approach with Monte Carlo simulation of three-dimensional models. Before doing that, it is generally good practice to perform a test in a well-known case, so that if something is wrong it will be easier to notice. For this reason, we can start with some simple simulations of the two-dimensional Ising model on a strip at the critical temperature $T_c = 2/\log(1+\sqrt{2}) \approx 2.269$. The strip has transverse length L and parallel length $6L$: it is important the length alongside the strip be much larger than the transverse length, but we have seen numerically that increasing it above 6 does not alter the results, so for our purposes $6 \approx \infty$. The spins on the left and right border of the strip are fixed to the value $+1$, while in the other direction periodic boundary conditions are enforced. Since the simulation is rather light, there is no real need to come up with clever algorithms to speed it up.
After the system has thermalized, we can start measuring the magnetization: we average the value of the spins at a distance x from the left boundary, and store this as the x^{th} value of an array. We repeat this for all x, let the system evolve further,

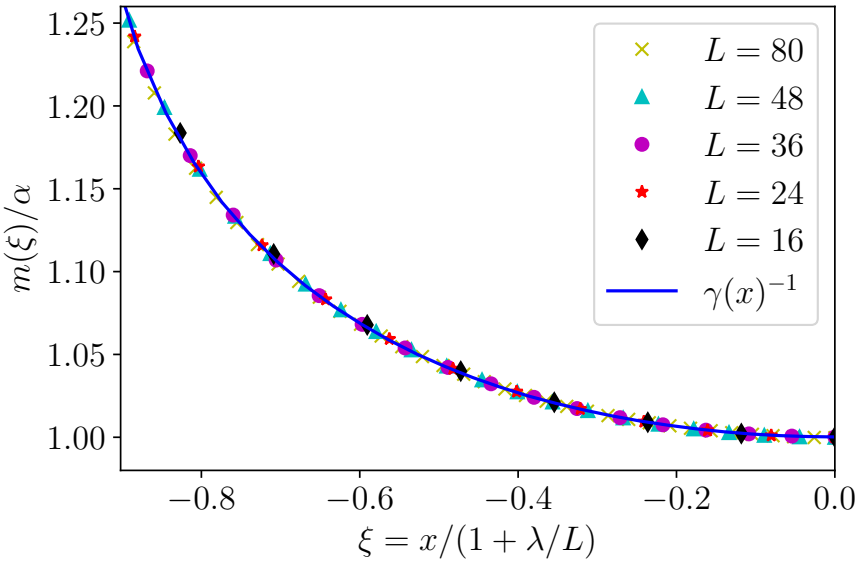

Figure 3.1: Magnetization profiles of the $2d$ Ising model on a strip for a few sizes, alongside the theoretical prediction from conformal field theory. The extrapolation length λ is about constant for the different sizes, ($\lambda = 0.933$ for $L = 16$ and $\lambda = 0.923$ for $L = 80$).

and then repeat the measurements. Once enough data are collected, the array contains our magnetization profiles. The point at distance x and $L - x$ from a boundary can be averaged together, as the profiles will be symmetric around the center. For this reason, we always make sure to select even value of L and build lattices where $x = 0, \ldots, L$, so that the profile consists of an odd number of sites, and we only plot the left half of the profile, as seen in Fig. 3.1.
Using the equation for one-point function (2.18) for the case of a strip (3.8), we expect the profile to be described by the function

$$m(x) = \alpha\gamma(x)^{-\Delta_\phi} = \alpha \cos\left(\frac{\pi}{2}x\right)^{-\Delta_\phi}, \tag{3.28}$$

for some constant α and the exponent is known to be $\Delta_\phi = 1/8$. x has been divided by the transverse half-length L so that $x \in [-1, 1]$. There is still an important detail missing: the theoretical profile diverges at the boundaries, but on a lattice the order parameter cannot diverge: the magnetization at the boundaries will be ± 1. More in general, the only conformally-invariant boundary conditions are $\langle\phi\rangle = \infty$ or $\langle\phi\rangle = 0$, but lattice simulation and experiments will of course finite values. This is where the extrapolation length λ, introduced in Chapter 1.3.2, comes into play: if the lattice magnetization profile were prolonged by λ sites beyond the boundary, these singularities would appear [55]. So in our case, with boundaries where we fixed the spins at $x = 0$ and $x = L$, after we fit the resulting profile $m(x)$, we would see divergences at $m(-\lambda)$ and at $m(L + \lambda)$. In the $L \to \infty$ limit, $\lambda \to 0$ and the magnetization diverges at the boundaries.
The function we need to use for regression is then

$$m(x) = \alpha\gamma \left(\frac{x}{1 + \lambda/L}\right)^{-\Delta_\phi}. \tag{3.29}$$

After determining the fit parameters α and λ for each size, we can rescale both x and the magnetization and see that the different profiles now lie on the same line, which is indeed Eq. (3.8): the collapse proves that we are at the critical point, and the agreement between points and the line shows the validity of Eq. (3.8). The two-dimensional check is therefore successful, and we can apply a similar method in three dimensions.

Chapter 4

Three dimensions: XY model and percolation

Even disregarding the boring detail that we happen to live in three dimensions, the $3d$ case happens to be the most interesting case, by virtue of being by far the most hostile: the usual statistical models currently have no exact solution in $3d$ and exact results in general are very sparse; we lack the comfort of an infinite-dimensional conformal group that simplifies life in two dimensions considerably, but we are below the upper critical dimension for ϕ^4 models. This case can therefore serve as the most challenging test of this approach, especially if one considers that the entire fractional laplacian construction becomes necessary specifically for $d = 3$ (although for percolation it would be needed for $d = 4$, 5 as well).

Numerical simulations for the three-dimensional Ising model had already been performed in [1]. The new results below are for the XY model and percolation, published respectively in [2] and [3].

4.1 XY model

A general introduction to the XY model can be found in Section 1.2.1. Here we start the discussion by motivating study of the XY model in a bounded system, and in particular why it is sensible to start from the slab geometry.

4.1.1 XY model with boundaries

The XY model in a slab is used to model the Casimir effect in Helium near the superfluid transition. Different kinds of boundary conditions can be used to

describe the various surface universality classes [67], defined in Chapter 1. In an ordinary transition, the bulk orders in the presence of a disordered surface: this corresponds to Dirichlet boundary conditions and is used to describe a pure ^{4}He fluid, whose wave function vanishes at the boundary [84]. Enhancing the surface coupling up to a critical value causes the boundary and the bulk to order at the same temperature; this special transition is characterized by Neumann boundary conditions [85]. Finally, if the boundary coupling is enhanced further, or a magnetic field is added at the boundaries, the surface will order at higher temperatures than the bulk. The transition of the bulk in the presence of an ordered surface is called extraordinary transition, and is associated with a diverging order parameter at the boundaries. In the presence of two ordered boundaries, we must then distinguish the case in which the respective spins are aligned (labeled $++$) from the case where they are antiparallel ($+-$). The latter case describes experiments with mixtures of two liquids, attracted to opposite surfaces [52, 86, 87]. The former case has also been studied experimentally [88]. We are going to focus on the $++$ case for the XY model. It should be added that, while measuring bulk quantities in an extraordinary transition, it does not matter *how* the surface order was achieved, whether it is by stronger couplings or by magnetic fields localized on the boundaries [89]. In our case, surface order can only be obtained through surface (magnetic) fields, since the surfaces are $2d$ and the XY model has a continuous symmetry: stronger couplings alone could not produce nonvanishing magnetization. We refer to [90] for a detailed analysis of the boundary phase diagram of the $3d$ $O(n)$ model for varying n.

4.1.2 $(N+1)$-state clock model

The spins in the XY model take value in $[0, 2\pi)$. Continuous variables are, however, inconvenient for numerical simulations, as generating them and computing Monte Carlo weights takes longer. Universality comes to our aid, providing a way to bypass this difficulty: we can obtain the same critical exponents and correlation functions while considering a different model in the same universality class as the XY model. A good candidate is the N-state clock model: it has the same Hamiltonian as the XY model, but the spins can take only N possible values, the vertices of a regular N-sided polygon:

$$\beta H = -\beta \sum_{<ij>} \vec{s}_i \cdot \vec{s}_j, \quad s_i = \left(\cos \frac{2\pi m}{N}, \sin \frac{2\pi m}{N} \right), \quad m \in \{0, \dots, N-1\}. \tag{4.1}$$

It has been shown [91] that the $3d$ clock model can be seen as an XY model with an

additional crystal field, which reduces the symmetry of the system from $O(2)$ to Z_N: at the critical point, this field becomes irrelevant as long as $N > 4$, meaning that it does not alter the universal properties we are seeking. In general, however, models with Z_N symmetry may have different properties than models with $O(2)$ symmetry, as seen in [92].

In any numerical simulation, the free energy per site and other quantities contain a leading term which is the thermodynamic limit, plus various finite-size corrections. Following [23], we take measures to reduce these corrections: the Hamiltonian is further modified by introducing vacancies. Placing a spin in any given site lowers the energy of the system by some amount D; by tuning this parameter, one can find a point D^* where the leading corrections to scaling vanish. The final Hamiltonian is then

$$\beta H = -\beta \sum_{<ij>} \vec{s}_i \cdot \vec{s}_j - D \sum_i s_i^2, \quad \vec{s}_i \in \{(0,0)\} \cup \left\{ \left(\cos \frac{2\pi m}{N}, \sin \frac{2\pi m}{N} \right) \right\}_{m=0,\ldots,N-1}. \tag{4.2}$$

To fully define the model, it is also necessary to specify the probability measure of each spin: the $(0,0)$ state is chosen to have the same weight as all the other states combined, so

$$w(\vec{s}_i) = \frac{1}{2}\delta_{s_i^2,0} + \frac{1}{2N}\delta_{s_i^2,1} \; ; \tag{4.3}$$

the partition function is then

$$Z = \sum_{\{\vec{s}\}} \left(\prod_i w(\vec{s}_i) \right) e^{-\beta H}. \tag{4.4}$$

4.1.3 Monte Carlo simulation

The geometry of the system is a slab of sizes $(L+1) \times 6L \times 6L$ (in the x, y, and z directions respectively), with periodic boundary conditions in the parallel (y and z) directions and fixed boundary conditions in the transverse direction. The values used for L are $32, 48, 64, 96, 128$. Like in the $d = 2$ case, the parallel directions have been chosen to be six times larger than the transverse one as they provide an excellent representation for the system with infinite transverse directions for the observables under scrutiny: indeed, we checked that further increasing the size of the parallel directions does not alter the magnetization profile. The model was simulated at the bulk critical temperature, using the values of $\beta_c = 0.56379622(10)$ and $D = 1.02$

obtained in [23]. We also used the same three kinds of Monte Carlo moves: two types of single-spin flip moves, and a cluster update.

The quickest spin flip move consists in proposing to empty the chosen site if it contains a spin, or fill it if empty, with a spin uniformly chosen out of the N values. This move, however, does not guarantee ergodicity, which is why we also use the second, more standard, type of move. In this second case, once a site is picked, regardless of the value of the spin we generate a new spin according to Eq. (4.3): an empty site half the time, a random spin, uniformly chosen out of the N possible ones, the other half. In either case, the move is then accepted or refused with the usual criterion of the Metropolis algorithm.

One of the well-known problems of simulating systems at the critical point is the critical slowing down effect: since the autocorrelation time diverges, even after many single-spin flips we still have samples correlated to the previous ones, and therefore unfit for new measurements. This problem can be ameliorated through moves that update large (correlated) chunks of the lattice at once, using the Wolff algorithm [93]. First, we select a reflection axis by picking a vector $\vec{r} = \left(\cos\frac{2\pi m}{N}, \sin\frac{2\pi m}{N}\right)$ uniformly in $m \in \{0, \ldots, N-1\}$. Then, we pick a random spin, mark it as part of the cluster and mirror it with respect to $\vec{r}$: $\vec{s}_i \to \vec{s}_i - 2(\vec{s}_i \cdot \vec{r})\vec{r}$. Next, we try and add to the cluster every neighbor of site i, according to the bond probability

$$P(\vec{s}_i, \vec{s}_j) = 1 - \exp\left(\min(0, 2\beta\, \vec{r}\cdot\vec{s}_i\ \vec{r}\cdot\vec{s}_j)\right). \tag{4.5}$$

The sites that have been added to the cluster are flipped, and the procedure continues in the same way. Once a spin has been added to the cluster and flipped, it cannot be selected or flipped again. To save time, the bond probabilities are computed once, at the beginning of the simulation.

A difference worth highlighting, with respect to the case with periodic boundary conditions, is that the cluster may reach a spin on the boundary. To overcome this difficulty we use the recent extension of the Wolff algorithm to the inclusion of arbitrary fields recently proposed in [94]. When the cluster touches the boundary all spins on both boundary planes must be treated as a single spin $\vec{S}_B$, which gets flipped according to the same rule. All boundary spins are added to the cluster, which can then keep growing from each boundary spin. The value of the new boundary spin is then stored to be used in future measurements. For instance, whenever the magnetization of a yz plane, at a given distance x from a boundary, is computed, this must be taken as the angle between the spins on the plane and the current boundary spin

$$m_x = \sum_{y,z} \vec{s}_{x,y,z} \cdot \vec{S}_B. \tag{4.6}$$

Once enough data are measured, we can obtain the magnetization profiles.

4.1.4 Magnetization profiles

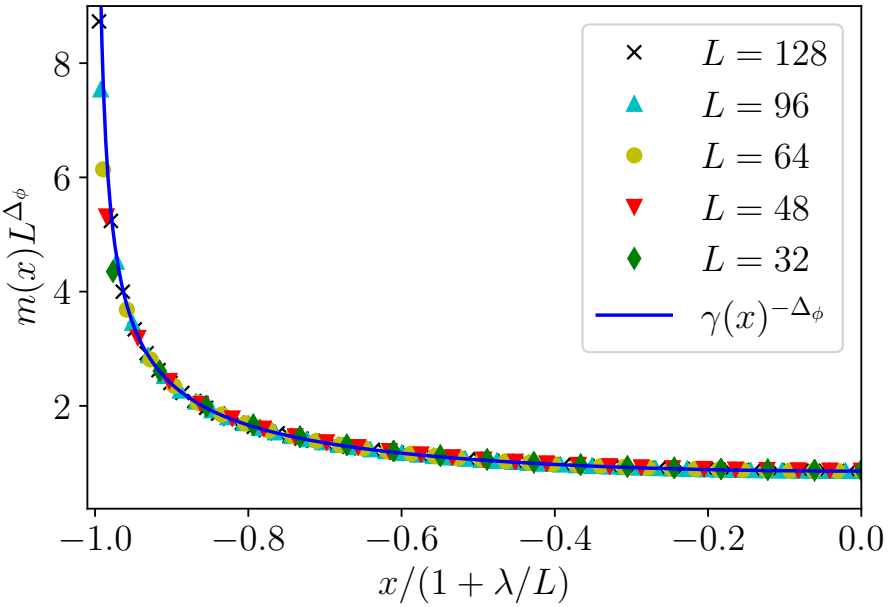

Figure 4.1: Magnetization profiles for different sizes, rescaled by L^{Δ_ϕ} and with the extrapolation length to show the collapse. The transverse direction of the slab is $x \in [-1, 1]$; the values of the magnetization at x and $-x$ have been averaged, so we plot only the left half of the profile.

By measuring the magnetization on various planes parallel to the boundaries, we obtain a function of the transverse distance, $m(x)$ (as a reminder, we use x to refer to the transverse distance).

After the magnetization data have been obtained, an additional step is needed before performing the fit. The points closest to the boundary are most affected by finite-size effects. Therefore, despite having smaller errors than the central points, a few of them have to be discarded. In order to determine how many to discard in an unbiased way, as well as to avoid a sharp distinction between discarded and included points, we introduce a window function $w(x)$. The weight of each point in the fit is given by the square of the ratio between this function and the error of that point. This function starts off from 0 at the boundary, ramps linearly to 1

around a movable point t, and maintains the value 1 up to the center of the slab. To determine the location of the point t, we start from $t = -1$ (the boundary point) and gradually move towards $t = 0$. For each value of t we compute the χ^2 of our data, and the corresponding p-value. We stop once the p-value reaches the reference value of $p = 0.95$, i.e. $\int_0^{\chi^2} p_{\chi^2}(\xi)d\xi \geq 0.95$.

At this point, the profile can be fitted by

$$\langle\phi(x)\rangle = m(x) = \alpha \left[L\ \gamma_{(\Delta_\phi)} \left(\frac{x}{1+\lambda/L} \right) \right]^{-\Delta_\phi}. \tag{4.7}$$

The fit parameters are a multiplicative constant α, the scaling dimension of the field Δ_ϕ and the extrapolation length λ, whose role was explained in Chapter 3.3. We notice that the extrapolation length remains roughly constant as the system size is increased, meaning that larger sizes capture a greater fraction of the continuum profile.

In Figure 4.1, we plot the magnetization profiles for different system sizes, appropriately rescaled by multiplying each profile by L^{Δ_ϕ}. The x coordinate has also been rescaled, to take into account the extrapolation length of each size. First of all, we notice a clear collapse of the different profiles onto the same curve, proving that we are at the critical point. For each system size, the fit using (4.7) gives us a value of the scaling dimension Δ_ϕ, as shown in Table 4.2.

As our final estimate, we take the average of the different values, obtaining

$$\Delta_\phi = 0.5206(15). \tag{4.8}$$

The error on Δ_ϕ is the standard deviation σ of the set $\{\Delta_\phi(L)\}$. Since their errors are too small for them to be compatible with one another, σ was not divided by the square root of the number of data points.

This is compatible, to one standard deviation, with the most precise estimate $\Delta_\phi^{CB} = 0.519088(22)$, obtained through conformal bootstrap [12]. This result should be intended as a check of the theory, since obtaining critical exponents is far from the only use of the critical geometry approach. Details on the data analysis are found in Appendix 8.2.

4.1.5 Correlation functions

Testing (2.21) is slightly more subtle because we cannot determine the function $\mathcal{F}$. Once the correlation data are divided by the product of one-point functions, i.e.,

$$r(\mathbf{x}, \mathbf{x}') = \frac{\langle\phi(\mathbf{x})\phi(\mathbf{x}')\rangle}{\langle\phi(\mathbf{x})\rangle \langle\phi(\mathbf{x}')\rangle}, \tag{4.9}$$

L	Δ_ϕ
32	0.5227(7)
48	0.5207(3)
64	0.5194(2)
96	0.5205(2)
128	0.5193(2)

Table 4.1: Scaling dimensions obtained from the fit for each system size. As final value, we take their average: $\Delta_\phi = 0.5206(15)$.

they will depend only on the distance between the points computed with our metric g. This means that the points will collapse onto a single line if plotted as a function of this distance, while they will appear scattered if plotted as a function of any other (nonequivalent) distance. The data we collected is averaged over the parallel directions:

$$C(x, x', \Delta y, \Delta z) = \frac{1}{(6L)^2} \sum_{y,z=1}^{6L} \langle \phi(x, y, z)\phi(x', y + \Delta y, z + \Delta z)\rangle \,. \tag{4.10}$$

To limit the volume of data, we measured correlations only in a $15 \times 15 \times 15$ grid: $x, x' = (i + 1)L/16$, $\Delta y, \Delta z = iL/16$, where $i = 0, \ldots, 14$. Once we take $x \geq x'$, we consider the points $C(x, x', \Delta y, \Delta z)$ and $C(x, x', \Delta z, \Delta y)$ to be the same data point, and exclude coinciding points, we get 7672 independent correlators. The fractional Yamabe distance between the points was computed via Surface Evolver [95] using as metric $g = \delta/\gamma^2_{(\Delta^{CB}_\phi)}$.

The correlation ratio as a function of the distance $\mathfrak{D}_g(x, y)$ are shown in the left pane of Figure 4.2: we see a clear collapse onto a single line. The value chosen for the scaling dimension Δ_ϕ affecting $\gamma_{(\Delta_\phi)}(x)$ and in turn the distances $\mathfrak{D}$ is Δ^{CB}_ϕ; however taking our best estimate (4.8) makes actually no visible difference. To see what would happen for a different, wrong from the outset, metric, we also plotted the same points as a function of the euclidean distance between them, in the right pane of Figure 4.2: a collapse is absent and the point are scattered.

To quantify the goodness of the collapse, we fit the points in 4.2 with the function $f(\xi) = 1+a_1e^{-b_1\xi}+a_2e^{-b_2\xi}$, and then compute the mean square displacement between the points and the curve ($n_{\text{d.o.f}}$ are the independent degrees of freedom):

$$\sigma = \sqrt{\frac{\left[r - f(\mathfrak{D}_g)\right]^2}{n_{\text{d.o.f}}}}. \tag{4.11}$$

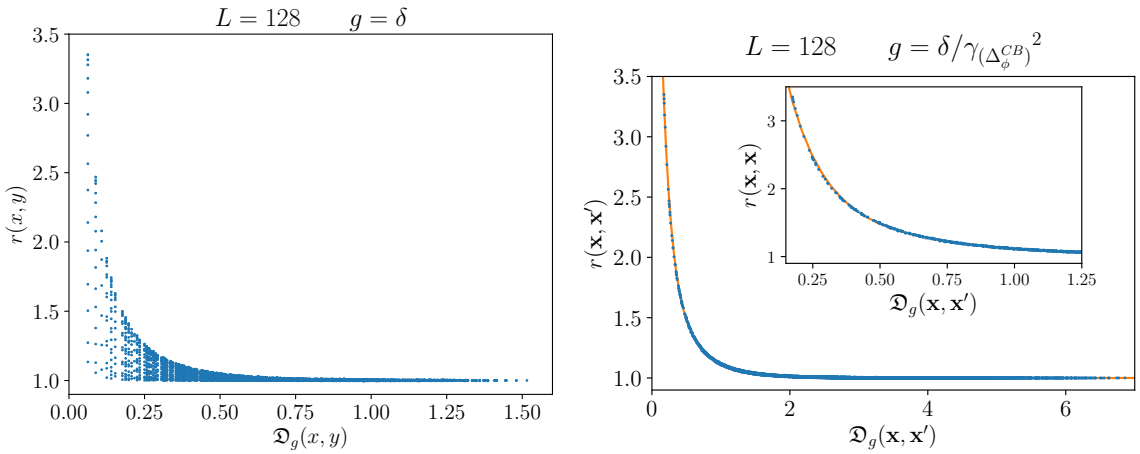

Figure 4.2: Correlation ratio $r(\mathbf{x}, \mathbf{x}') = \langle\phi(\mathbf{x})\rangle^{-1} \langle\phi(\mathbf{x}')\rangle^{-1} \langle\phi(\mathbf{x})\phi(\mathbf{x}')\rangle$: on the left, plotted as a function of the euclidean distance: since that is not the "correct" metric, the points are scattered. On the right, the same points plotted as a function of the distance $\mathfrak{D}_g(\mathbf{x}, \mathbf{x}')$, computed with the metric which solves the fractional Yamabe equation for $\Delta_\phi = \Delta_\phi^{CB}$, the most accurate estimate. The points collapse onto one line. In the inset a zoom of the region where the ratio displays more pronounced variations is shown.

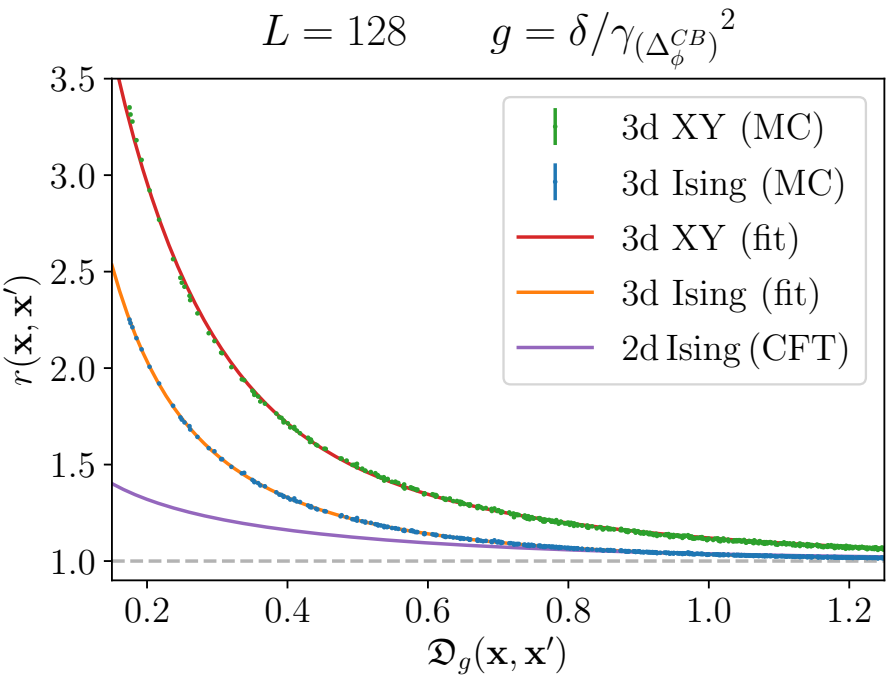

Figure 4.3: Correlation ratio of the $3d$ Ising and clock models, each computed as a function of the respective fractional Yamabe distance. The lines shown under the numerical data are fitting functions. The exact function is shown also for the Ising $2d$ as obtained exactly from CFT, see (3.24).

We obtain $\sigma = 0.0077$ for $L = 32$, $\sigma = 0.0036$ for $L = 64$ and $\sigma = 0.0029$ for $L = 128$: the fact that displacements become smaller for larger sizes lends quantitative support to the collapse. Notice that the chosen fitting function f correctly captures the long (mutual) distance limit of the correlation ratio, that is $r \to 1$ as $\mathfrak{D} \to \infty$. Concerning the short distance properties, the operator product expansion structure should be retrieved; this, however, is not the focus of the present investigation, since short distance behavior is not crucially affected by the curved space properties we are interested in, as well as being challenging to retrieve from lattice approaches.

4.1.6 Comparison with the Ising model

As we mentioned, the function $\mathcal{F}(\mathfrak{D}_g)$ of the distance between the points is not known in $d \neq 2$ and our approach cannot determine it without using the input from the numerical simulations. Figure 4.2 shows the existence of $\mathcal{F}$ through the collapse

of the data. One sees that we can obtain a precise numerical estimate of it.

To put in context the result obtained for the $\mathcal{F}$ of the $3d$ XY model, we can now set it side by side with the same function for the Ising model. In Figure 4.3, we compare the correlation ratio r we obtained for the XY class with the corresponding profiles for the $3d$ Ising model (obtained in [1]). We see qualitatively similar curves in the two cases, with greater correlation ratio for the XY model with respect to the Ising one. The quality of the collapse in $3d$ both for the XY and the Ising models is similarly convincing. Notice that the metric for the Ising model is different from the one for the XY model, since they have different scaling dimensions, producing distinct fractional Yamabe equations and yielding in turn different collapse distances. As expected, both correlation ratios tend to 1 for large $\mathfrak{D}$.

4.2 Percolation

Now we can move to the next three-dimensional model, percolation, introduced in Chapter 1.2.2. We are going to focus on the order parameter profile, which one can be interested in for two reasons: from one side, if one assumes the value of the critical exponent η available in literature, then the equation for the one-point function (2.18) gives predictions for the order parameter at criticality, which are not easy to obtain for percolation in dimension greater than 2 with other approaches. From the other side, for percolation in $d = 3$ the exponent η is known with much lower precision than the corresponding exponent in other models, such as the Ising model [96]; one reason for this is the fact that the most accurate critical exponents currently available for the three-dimensional Ising [97] and XY model [12] come from the conformal bootstrap [98], which however cannot be applied straightforwardly to non-unitary models such as percolation. So, a truly challenging task for the critical geometry approach is to determine η for $3d$ percolation. Further direct determinations of η, obtained through other methods, could provide a stringent test for critical geometry. Independently from this test, checking scaling and hyperscaling relations using the values of the other critical exponents also puts a bound on the validity of the critical geometry approach. At the same time, one obtains in this way as a by-product predictions for the critical order parameter profile.

4.2.1 Continuum percolation

The discussed approach could be applied to simulation of lattice percolation at the critical point. However, since this approach uses as input continuous order parameter profiles at criticality, it is advantageous to extract these profiles from simulations

performed with objects placed continuously in space [99, 100, 101], which is commonly referred to as continuum percolation [30]. The algorithm is straightforward: d-dimensional balls with unit diameter are generated, one at a time. The center of each is picked randomly, with uniform probability within a slab. If the ball intersects another one, it is added to the cluster of the latter. If it intersects two or more balls belonging to different clusters, the clusters are merged, as explained in Appendix 8.3. We stop adding objects once the product of their number and the relative volume of one object reaches the critical filling fraction η_c, which means we are at the critical point: measurements can then begin. Objects other than balls could be used, as these other models would belong to the same universality class, but determining intersections would become more challenging.

The order parameter $\langle\phi(x)\rangle$ is the density of the giant cluster, function of the distance from one boundary parametrized by x. What we call "giant cluster" may not be apparent at first, due to the need to impose fixed boundary conditions. In percolation in general, the giant cluster which emerges at the critical point is the one which contains a finite fraction of all the lattice points (or objects, in our case) even in the thermodynamic limit. If percolation is simulated in a large but finite system, this cluster is also the one which connects the boundaries.

In our case, however, we want to have a diverging order parameter at the boundary: in spin models, this of course meant fixing all the spins to be aligned. In percolation, what we have to do is impose from the beginning that each ball which intersects either boundary automatically belongs to the same macroscopic cluster. One can visualize this by imagining that the boundaries are a single object, as if they were joined in a way that does not alter the density of objects (I picture a thin thread connecting them). This way, sets of balls which intersect the boundary at different points are treated as part of the same cluster, even though they may not intersect each other directly. This means that close to the boundary the density of the giant cluster is maximum, and it decays as one approaches the center. Like in the spin cases, the resulting order parameter profile is symmetric around the center.

The order parameter at a point x is obtained by slicing the giant cluster with a plane, a distance x from one boundary, and then measuring the total area (in $2d$, length) obtained as intersections between the objects and the plane. This means that the profiles generated by the simulations are continuous themselves, lifting discretization effects (finite-size effects being of course still present).

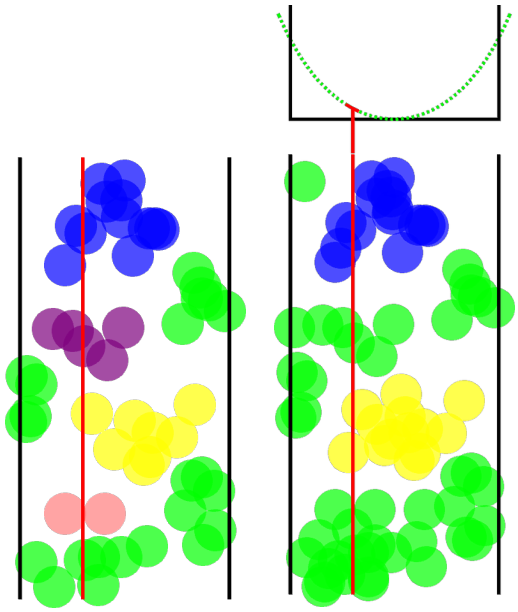

Figure 4.4: Continuum percolation in $2d$. Fixed boundary conditions are enforced: when a circle intersects either boundary, it gets added to the giant cluster (green). Left: $\eta < \eta_c$ — Right: $\eta = \eta_c$. The segments obtained as intersection between the red line and the green balls contribute to the profile sketched above, obtained by averaging different realizations. The dashed line illustrates the average on different realizations, as shown by the data plotted in Fig. 4.5; it extends beyond the slab boundaries to illustrate the effect of the extrapolation length λ.

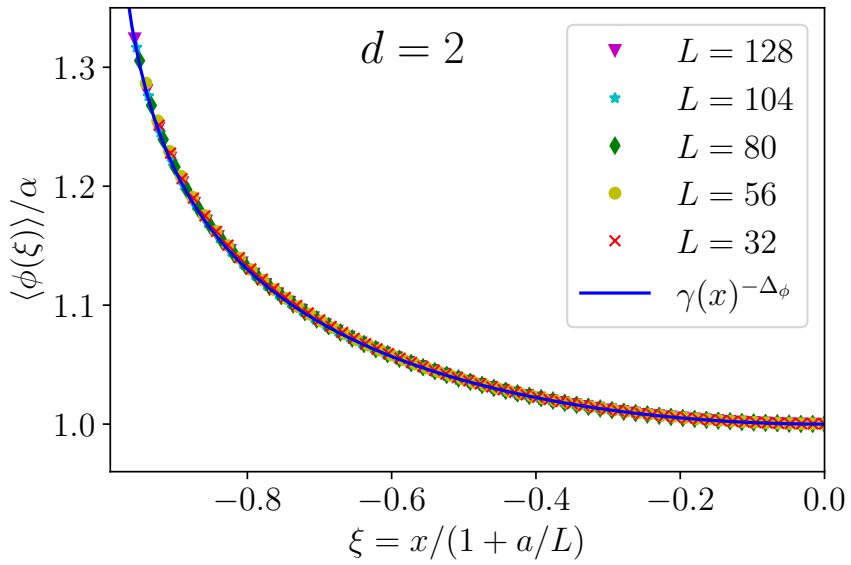

Figure 4.5: Order parameter profile for selected sizes, in $d = 2$. We see a clear collapse of the points for different sizes, proving that we are at the critical point. The theoretical curves fit the data points accurately.

4.2.2 $2d$ percolation

Before venturing into the $3d$ case, we consider percolation in two dimensions, where several exact results for crossing probabilities and correlation functions are available (e.g. [102, 103, 104, 105]). In particular, we want to ensure that our method gives a value for the exponent Δ_ϕ in agreement with the analytical prediction.

The system is a strip of sizes (in units of the diameter of a sphere) L in the transverse direction x and $4L$ in the parallel direction y, along which periodic boundary conditions are imposed. Different ratios between the two sizes have been tested: increasing this ratio beyond 4 does not alter the results. The density of critical percolation clusters in $2d$ strips was also studied in [73]. L ranges from 16 to 128, in steps of 8. The critical filling ratio we used [100] is $\eta_c^{2d} = 1.12808737$ (the error on η_c does not meaningfully alter our results, as seen in Appendix 8.4. Continuous percolation allows us to get comparable results for different sizes, by measuring the order parameter $\langle\phi(x)\rangle$ across a fixed odd number $2n - 1$ of planes for every system size (even for small L), equally spaced throughout the slab. By symmetry, the values x and $L - x$ have been averaged: each profile consists of n points.

We can perform a similar fit as before, using Eq. (4.7). Again, the profiles for

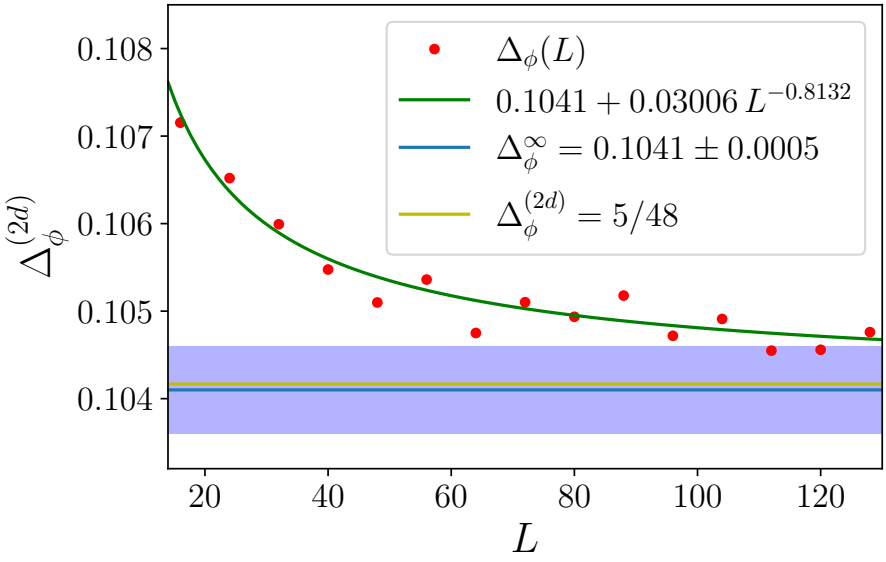

Figure 4.6: Fit results $\Delta_\phi(L)$ as the system size L increases in $d = 2$ (red dots). The green line is the extrapolation fitting function (4.12) while the blue line is our best estimate Δ_ϕ^∞ with the shading representing the error σ on Δ_ϕ^∞. The yellow line is the exact value. Despite relatively small system sizes, Δ_ϕ^∞ is convincingly close to the exact value.

different sizes have been rescaled by multiplying each by $L^{-\Delta_\phi}$ and by plotting them as a function of $\xi = x/(1 + a/L)$, so they collapse onto the same curve, $\alpha/\gamma(\xi)^{\Delta_\phi}$, as seen in Fig. 4.5; each size gives a corresponding $\Delta_\phi(L)$.

We notice in Fig. 4.6 a decay of the fit parameter $\Delta_\phi^{(2d)}(L)$ as the size L increases. To extrapolate the correct value, free of finite-size effects, we perform a fit in the form of a power law:

$$\Delta_\phi(L) = \frac{c}{L^k} + \Delta_\phi^\infty, \tag{4.12}$$

with c, k, and Δ_ϕ^∞ as fit parameters. This gives $\Delta_\phi^\infty = 0.1041(5)$, a good estimate, relative to the small numerical effort, of the exact value $\Delta_\phi^{(2d)} = 5/48 \approx 0.10417$. This procedure differs from what was previously done for the clock model: the different method follows from the data and the respective errors. It seems logical to believe that by computing critical exponents numerically from finite-size simulations, one obtains a monotonous function $\Delta_\phi(L)$ the converges to the exact value Δ_ϕ in the limit $L \to \infty$. In the case of the clock model, however, the difference between $\Delta_\phi(L)$ and the exact Δ_ϕ^∞ was due to numerical error more than finite-size corrections. For

this reason, the plot of various exponents as a function of the system size lacked a monotonous behavior, and it was therefore impossible to extrapolate the $L \to \infty$ value. The best we could do in that case was to assume finite-size effects are negligible compared to the errors and obtain our estimate for Δ_ϕ^∞ as the weighted average of the exponents for the various sizes.

4.2.3 $3d$ percolation

The same can now be done for a $3d$ slab (see Fig. 4.7) of sizes $L\times 4L\times 4L$; L ranges from 16 to 100 in steps of 4, and the critical filling fraction used is $\eta_c^{3d} = 0.341888$, currently the most precise estimate [106]. Like for the $3d$ clock model and unlike the two-dimensional case, we need to solve the fractional Yamabe equation for a range of values of Δ_ϕ roughly centered around the current best estimates. We thus obtained a solution $\gamma_{(\Delta_\phi)}(x)$ that varies smoothly for $\Delta_\phi \in [0.46, 0.5)$. While it would have been convenient, we cannot obtain a solution which can be used both for the XY model and percolation, since the value $\Delta_\phi = 1/2$ is special as the fractional equation reduces to the integer one.

We obtain another clear collapse of the profiles in Fig. 4.8. The data are indeed described in an excellent way by the fitting function (4.7). For each system size values of Δ_ϕ are obtained. Similarly to the $2d$ case a slight decay with L (Fig. 4.9) is observed. By using a similar infinite-size extrapolation (4.12) we obtain our estimate for the scaling dimension:

$$\Delta_\phi = 0.47846(71), \tag{4.13}$$

where the uncertainty is the statistical error on the fit parameter. From the definition $\Delta_\phi = \frac{d-2+\eta}{2}$, we get the corresponding anomalous dimension:

$$\eta = -0.0431(14). \tag{4.14}$$

In Table 4.2 we see that our result compares favorably to other determinations of η. Future high-precision determinations of η, using different methods, could give further support to the validity of the uniformization hypothesis if compatible, or disprove it if not.

4.2.4 Scaling relations

Critical exponents are connected by well-known scaling relations [67], which we can exploit to check the validity of our result. The scaling relation involving η and independent from d is

$$(2-\eta)\nu = \gamma; \tag{4.15}$$

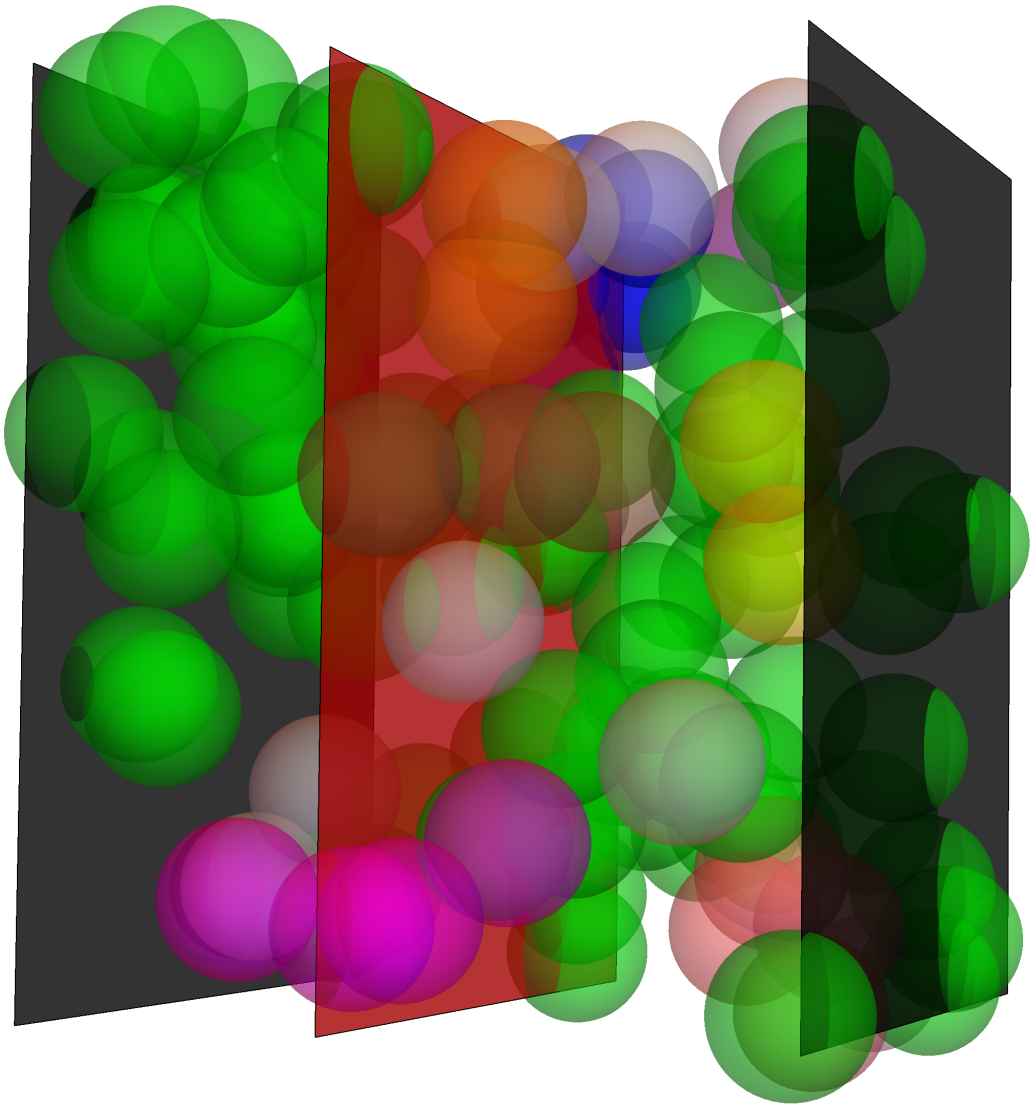

Figure 4.7: Giant cluster (green spheres) sliced by a plane (red). The black planes are the system boundaries: balls intersecting either belong to the giant cluster. This figure is so big because it took me a while to make, so now I enjoy looking at it.

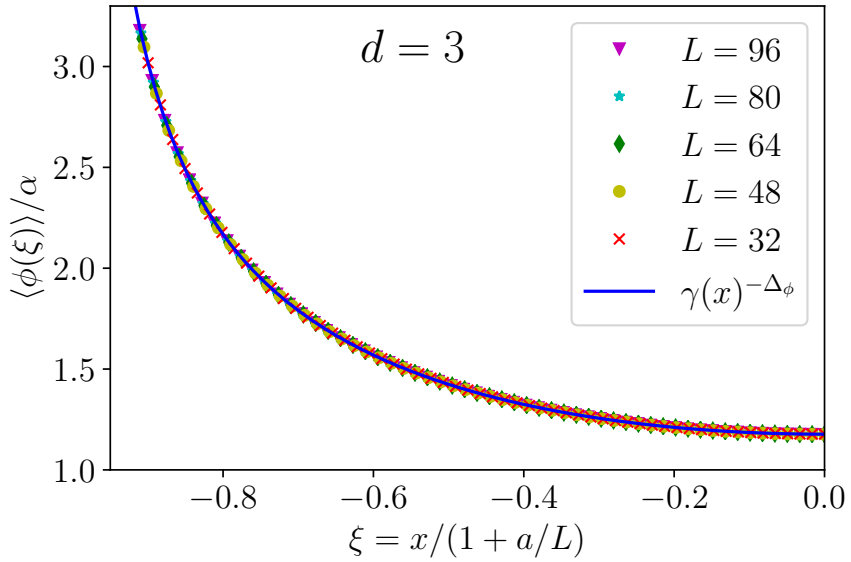

Figure 4.8: Order parameter profiles in $d = 3$. Once again, the theoretical curve fits the data points accurately.

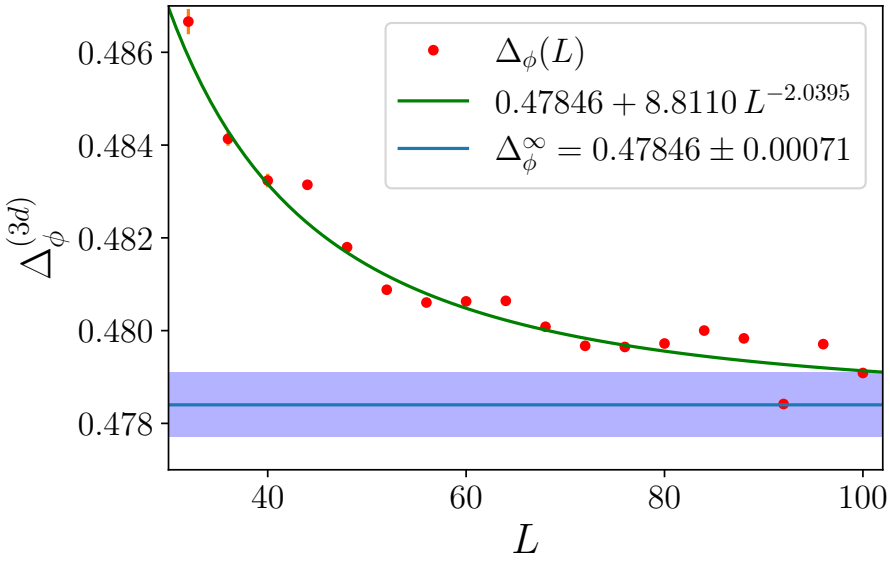

Figure 4.9: Finite size estimates $\Delta_\phi(L)$ for the $d = 3$ slab (red dots) as a function of L. The extrapolation curve (4.12) is the continuous green line while the infinite size value Δ_ϕ^∞ is the dashed blue line. The shaded area represents the error σ on Δ_ϕ^∞.

Reference	year	Method	η
Adler et al. [107]	1990	Moment expansion	$-0.07(5)$
Lorenz & Ziff [108]	1998	MC, bond percolation	$-0.046(8)$
Jan & Stauffer [109]	1998	MC, site percolation	$-0.059(9)$
Xu et al. [110]	2013	MC, multiple lattices	$-0.0458(2)$
Ballesteros et al. [111]	1999	MC, site percolation	$-0.04602(34)$
Gracey [112]	2015	4-loop RG	-0.0470
Borinsky et al. [113]	2021	5-loop RG	$-0.06(10)$
This work [3]	2022	Critical geometry	$-0.0431(14)$

Table 4.2: Comparison of the value of the anomalous dimension obtained with various methods. The results above the solid line make use of hyperscaling equalities in different ways: [107] uses (4.15) but determines ν through a hyperscaling relation involving β; [108] and [109] determine the Fisher exponent τ, related to the size distribution of clusters, and relates it to η through the fractal dimension d_f, while [110] measures d_f directly. From that one gets η using $\eta = 2 + d - 2d_f$. [111] determines η using the scaling relation (4.15). Below the dashed line are the direct determinations of η using loop expansions [112, 113] and our result.

substituting our result, alongside $\gamma = 1.805(20)$ [107] and $\nu = 0.8762(12)$ [110], we get $1.790(2) = 1.805(20)$, meaning the equality is satisfied to one standard deviation.

Another class of relations between critical exponents is given by the hyperscaling relations [67], where the dimensionality of the system enters explicitly. While they take the form of inequalities [114], current results suggest they saturate. Out of the seven inequalities given in [114], two of them involve the exponent μ, related to percolation with an "external field". Four of them contain the rarely used exponents δ_r and Δ ($\Delta \equiv \beta + \gamma$). Another relation depends on ν but not on η. The remaining one, dependent on d, is

$$(d - 2 + \eta)\nu - 2\beta \geq 0. \tag{4.16}$$

With our value of η and using $\beta = 0.41(1)$ [115], one gets $(1-\eta)\nu - 2\beta = 0.018(22)$, so the left-hand-side of (4.16) is compatible with 0.

If the hyperscaling equalities could be shown to hold, η could be indirectly determined by measuring the fractal dimension d_f. Using then the relation $\eta = 2 + d - d_f$ and the value $d_f = 2.52293(10)$ from [110], one would obtain $\eta = -0.04586(20)$, which is compatible with our results within two standard deviations.

To summarize, in this chapter we have seen how the uniformization approach performs in three dimensions, which is both the most interesting case and the hardest one to study, because of the lack of exact results and the need to modify the Yamabe

equation to account for the anomalous dimension of the fields. It is particularly rewarding to have described a purely geometrical model like percolation using this geometrical theory. While the determination of correlation functions continues to be the main goal of this theory, the results for the exponent Δ_ϕ for the two models provides additional pieces of evidence which qualitatively and quantitatively support the critical geometry approach.

Chapter 5

Upper critical dimension

At the upper critical dimension, the anomalous dimension of the field vanishes, meaning that the order parameter has scaling dimension $\Delta_\phi = (d-2)/2$, so it should solve the integer Yamabe equation. This chapter is devoted to this investigation.

Working at the upper critical dimension has the important advantage that analytical calculations can be performed, unlike lower dimensional cases. These results can also be a useful starting point for calculation of critical magnetization profiles at lower dimensions, as they give the background on top of which other terms can be added.

Like in the previous chapter, the geometry we will consider is that of a slab. However, this time we can study more than just ++ boundary conditions, as we will be able to see the other scale-invariant cases: opposing $(+-)$, open (00) and mixed $(+0)$ BCs. For these cases, we will derive the magnetization profiles at the upper critical dimensions $d = 3,\ 4,\ 6$, and relate them to the Yamabe equation. From the saddle-point equations for the magnetization, we find general formulas in terms of Weierstrass elliptic functions, which as far as we know are new for the case of percolation. The zeros and poles of the Weierstrass elliptic solutions can be put in direct connection with the boundary conditions.

For the specific case of the 4-dimensional Ising model with fixed boundary conditions, we can then compare the predicted magnetization profiles with Monte Carlo simulations.

5.1 Magnetization profiles

In the following, we study exact solution for the critical magnetization profiles for models living at their upper critical dimension. We can start by generalizing the

action from Eq. (1.16) into something that can also work for $d = 3$:

$$S = \int d^d x \left[\frac{1}{2}\phi(-\triangle)\phi + \frac{1}{2}\mu^2\phi^2 + g\, c_d\, (\phi^2)^{\frac{d}{d-2}} \right], \tag{5.1}$$

as the exponent in the potential term is chosen so that the coupling is marginal. We see that the field ϕ has $\mathbb{Z}_2$ symmetry: the case of a ϕ^3 theory, describing percolation (lacking this symmetry), has to be treated separately with the introduction of a similar action in $d = 6$.

The action can be generalized to a vector field $\vec{\phi}$ with N components: in this case, ϕ^2 in the potential term is replaced by $\sum_{i=1}^{N} \phi_i^2$. In (5.1) the factor

$$c_d \equiv \frac{(d-2)^2}{8}$$

in the interaction constant has been chosen for convenience, as it will appear later. The exponent in the potential term of Eq. (5.1) is written so that we are at the upper critical dimension. The mass term $\propto \phi^2$ is also included, although it will not appear as all the calculations are performed at the critical point where it vanishes [67, 116].

The saddle-point equation for the action (5.1) at the critical point reads

$$\triangle m(\mathbf{x}) = g\frac{d(d-2)}{4} m(\mathbf{x})^{\frac{d+2}{d-2}}, \tag{5.2}$$

with $m(\mathbf{x}) = \langle \phi(\mathbf{x}) \rangle$.

We will now specialize the study of the saddle-point approximation for the action (5.1) for the physical dimensions taking the values $d = 3$, 4, and 6. This is firstly due to their physical relevance, but also for the striking mathematical properties they display only for these values of d. The peculiarity amounts to the fact that they are the only dimensions where the magnetization profiles can be expressed as suitable powers of the elliptic Weierstrass function $\wp$ (see Appendix 8.5 and [117] for reference).

5.1.1 Boundary conditions

We briefly touched on boundary conditions in Chapter 1, but so far all we needed to know is that the uniformization approach works for Fixed Boundary Conditions (FBC). Here, however, we can explore more options. On a slab, and focusing on the Ising model for simplicity, FBC include both forcing the spins on the two boundaries to be aligned (all up or all down, which we can label ++ FBCs), the case we

considered so far, but one can also force the spins on the two boundaries to be antiparallel, leading to $+-$ FBCs. The corresponding magnetization profile vanishes in the center, so either half of this profile could be obtained by fixing the spins on one boundary, and leaving the other boundary free (Mixed Boundary Conditions, $+0$.) Finally, if we allow the spins on both boundaries to take any value, we get Open Boundary Conditions (OBC, 00). However, in this case, the magnetization profile is trivially $m(x) = 0$ throughout the slab since the system is at the critical temperature (see [118] for example). Obtaining a nonzero magnetization profile for OBC requires the introduction of a magnetic field, vanishing at the boundaries, turning Eq. (5.2) into

$$m''(x) = g\frac{d(d-2)}{4}m(x)^{\frac{d+2}{d-2}} - h(x), \tag{5.3}$$

The shape of the 00 profile will then depend on the choice of magnetic field $h(x)$, mentioned below. From the scaling dimension Δ_ϕ of the order parameter, we can also obtain the behavior near the boundary. The possible cases are:

BC	Lattice	$m(x \to 0)$	$m(x \to L)$
$++$	$\uparrow \dots \uparrow$	$x^{-\Delta_\phi}$	$(L-x)^{-\Delta_\phi}$
$+-$	$\uparrow \dots \downarrow$	$x^{-\Delta_\phi}$	$-(L-x)^{-\Delta_\phi}$
00	$0 \dots 0$	x	$L-x$

Table 5.1: Labels for the possible boundary conditions, with the corresponding spin configuration and behavior of the continuous profile near the boundaries. "0" refers to spins being left free.

If we were to consider $O(N)$ models with $N > 1$, there would be an additional degree of freedom in the choice of boundary conditions: the angle between the spins on the two boundaries. The magnetization becomes then a vector in the plane spanned by the boundary spins, and the saddle-point becomes a system of two equations. So, while the $+-$ solution is specific to the Ising model, the $++$ one is valid for any $O(N)$ model with parallel boundary spins. Here we focus on conformally invariant boundary conditions (FBC, OBC and mixed BC), which are homogeneous on the slab plates. Other boundary conditions are possible, such as the one considered in [119] to enforce a topological excitation.

5.1.2 ϕ^4 theory in four dimensions

In four dimensions the action (5.1) reads

$$S = \int d^4x \left[\frac{1}{2}\phi(-\triangle)\phi + \frac{1}{2}\mu^2\phi^2 + \frac{1}{2}g\,\phi^4 \right]. \tag{5.4}$$

As seen in Chapter 1.1.4, this action can be used to describe the Ising model. Since the theory is at the upper critical dimension, we proceed by writing the saddle-point equation. The saddle-point equation for the action at the critical point $\mu = 0$ is

$$\triangle m(\mathbf{x}) = 2\,g\,m(\mathbf{x})^3. \tag{5.5}$$

We are interested in solving equation (5.5) in the case of a slab domain $[0, L] \times \mathbb{R}^3$. The magnetization $m(\mathbf{x})$ only depends on the transverse direction x, so the Laplacian $\triangle$ reduces to ∂_x^2. The different solutions for various boundary conditions will be analyzed and compared in the rest of the this section. In Section 5.4 we will compare the analytical results so obtained with Monte Carlo simulations for the Ising model on a $4d$ slab geometry with fixed boundary conditions.

Notice that given a solution $m(x)$ of (5.5) we can generate other solutions by translation and rescaling ruled by the parameters x_0, β, and λ, all of them being possibly complex:

$$m(x) \to \beta\, m(\lambda\,(x - x_0)) \qquad g \to g\,\beta^{\frac{-4}{d-2}}\,\lambda^2. \tag{5.6}$$

This allows us to change the domain/coupling constant as desired; for convenience we set $g = 1$. In general such scaling will alter the boundary conditions, however scaling invariant conditions, i.e. $m = 0$, ∞, are left unchanged. We remark that the scaling (5.6) applies also to other values of d and it will thus be useful for the other values of d considered.

The general solution to Eq. (5.5) (with $g = 1$) is

$$m(x) = \lambda \wp_l(\lambda(x - x_0))^{1/2}, \tag{5.7}$$

where $\wp_l$ is the Weierstrass $\wp$ function with invariants $(g_2, g_3) = (1, 0)$. This is the so-called lemniscatic case. When it is written in terms of the complex variable z as $\wp_l(z)$, it corresponds in the complex plane to a square lattice, with a real half-period $\omega_l = \Gamma(\frac{1}{4})^2/(4\sqrt{\pi})$.

The Weierstrass elliptic $\wp$, whose basic properties are refreshed in Appendix 8.5, is a doubly periodic function. Within one of its domains in the complex plane, it has a double pole and two zeros possibly coinciding (as here): taking segments

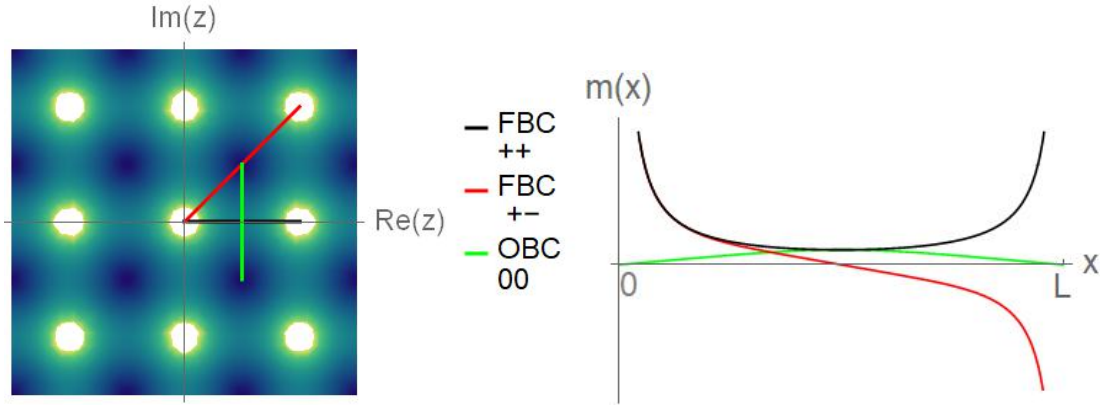

Figure 5.1: $d = 4$ — Left: modulus of the square root of the lemniscatic elliptic function, poles are white and zeros blue. Right: magnetization profiles for the different boundary conditions discussed in the text. The maximum of the OBC profile is a saddle point, so it is also the minimum of the ++ profile: its value is $\wp(\omega_l)^{1/2} = 1/\sqrt{2}$.

with poles/zeros as their endpoints gives solutions with various boundary conditions. Along the segments the function has to be real or have a constant phase (which can removed) in order to be interpreted as magnetization profiles.

The corresponding (unscaled) solutions are

$$\begin{aligned} m_{++}(x) &= \wp_l(x)^{1/2} && x \in (0, 2\,\omega_l) \\ m_{+0}(x) &= \wp_l(x\,e^{i\pi/4})^{1/2} e^{i\pi/4}, && x \in (0, \sqrt{2}\,\omega_l] \\ m_{00}(x) &= \wp_l(\omega_l + i\,x)^{1/2}, && x \in [-\omega_l, \omega_l]. \end{aligned} \tag{5.8}$$

By extending the $m_{+0}(x)$ solution to the interval $x \in (0, 2\sqrt{2}\omega_L)$ we indeed generate a solution m_{+-} connecting the $+$ and $-$ boundary states. This reflects the $\mathbb{Z}_2$ symmetry of the model as it is apparent in the saddle-point equation (5.5) with $m(x) \to -m(x)$. We have yet to specify how to find m_{00} in (5.8). This profile satisfies the saddle-point equation

$$m''_{00}(x) = -2g m_{00}(x)^3, \tag{5.9}$$

i.e. (5.5) with the *opposite* sign. The magnetic field needed to obtain the m_{00} solution listed in 5.8 has to be a power of m_{00} itself; in particular, $h(x) = 4g m_{00}^3(x)$, so that Eq. (5.3) is solved by $m(x) = m_{00}(x)$. Numerical solutions on the Ising model confirmed the existence and correctness of the solution m_{00} in (5.8). Other magnetic fields could be chosen, however the corresponding magnetization profile would in general no longer be an elliptic function.

One can give the following argument for the the aforementioned choice of $h(x)$ leading to the 00 solution. The function m_{00} is nothing but the reciprocal of the $++$ solution, up to a constant: shifting the argument of the function by half a period has the same effect as taking its inverse, since both operations swap poles and zeros. This is because the fundamental domain of $\wp_L$ is a square, as square lattice tessellation of the plane is self-dual. This is represented in Fig. 5.1, together with the plot of the solutions for the different boundary conditions.

This peculiarity of the elliptic functions must reflect in a property of the saddle-point equation, valid only for $d = 4$ and when the Laplacian reduces to an ordinary second derivative: if $\phi(x)^{-1}$ is a solution, then so is $\mathcal{K}\,\phi(x)$, for an appropriate $\mathcal{K}$. It is

$$\frac{d^2}{dx^2}\phi(x)^{-1} = 2\phi(x)^{-3}, \tag{5.10}$$

from which

$$\phi\phi'' - 2(\phi')^2 + 2 = 0 \tag{5.11}$$

(where $\phi'' = \frac{d^2}{dx^2}\phi$). Taking another derivative gives

$$\frac{\phi'''}{\phi''} = 3\frac{\phi'}{\phi}, \tag{5.12}$$

and, after integrating and exponentiating, we are left with

$$\phi''(x) = \mathcal{K}\,\phi(x)^3, \tag{5.13}$$

which is the saddle-point equation for $\sqrt{\frac{2}{\mathcal{K}}}\,\phi(x)$.

5.1.3 ϕ^6 theory in three dimensions

A ϕ^6 theory has upper critical dimension $d_c = 3$. The steps of the previous section can be repeated in this case. We start from the Landau-Ginzburg action at the critical point, where the couplings of the ϕ^2 and ϕ^4 terms vanish:

$$S = \int d^3x \left[-\frac{1}{2}\phi(-\triangle)\phi + \frac{g}{8}\,\phi^6\right]. \tag{5.14}$$

On the slab geometry $[0, L] \times \mathbb{R}^2$, we get the saddle-point equation

$$m''(x) = \frac{3}{4}\,g\,m^5, \tag{5.15}$$

where again due to the scaling property (5.6) we set $g = 1$. The solution is

$$m(x) = \lambda^{1/2} \wp_e(i\,\lambda\,(x - x_0))^{-1/2}. \tag{5.16}$$

In the present case, the invariants of the Weierstrass function $\wp_e$ are $(g_2, g_3) = (0, 1)$, from which its real half-period is $\omega_e = \Gamma(\frac{1}{3})^3/(4\pi)$.

The above case $\wp_e$ of the Weierstrass function is the so-called equiharmonic case, where the lattice used to define the elliptic function is the regular triangular tiling of the plane, see Fig. 5.2.

Remarkably, the solution for $d = 6$, presented in the next subsection, will turn out to be dual to this one. Again, looking at the poles and zeros of $m(z)$, we obtain solutions for the possible boundary conditions:

$$\begin{aligned} m_{++}(x) &= \wp_e(\omega_e + i\,x)^{-1/2} && x \in (-\frac{\omega_e}{\sqrt{3}}, \frac{\omega_e}{\sqrt{3}}) \\ m_{+0}(x) &= \wp_e(x\,e^{i\pi/6})^{-1/2} e^{-i\pi/6} && x \in (-\frac{2\omega_e}{\sqrt{3}}, 0] \\ m_{00}(x) &= \wp_e(x)^{-1/2} && x \in [0, 2\omega_e]. \end{aligned} \tag{5.17}$$

These solutions could also be expressed through Jacobi elliptic functions, as was done for the ++ solution in [120], through Fisher-De Gennes theory [121]. Again due to $\mathbb{Z}_2$ invariance, reflected in the $m(x) \to -m(x)$ symmetry in the saddle-point equation, the $m_{+0}(x)$ can be extended further in the interval $x \in (-\frac{2}{\sqrt{3}}\omega_e, \frac{2}{\sqrt{3}}\omega_e)$ yielding a $m_{+-}(x)$ profile. Obtaining the OBC solution requires, again, a magnetic field, of the form $h(x) = \frac{3}{2} g m_{00}(x)^5$.

5.1.4 ϕ^3 theory in six dimensions

In $d = 6$, we consider an action with cubic potential:

$$S = \int d^6x \left[\frac{1}{2}\phi(-\triangle)\phi + 2\,g\,\phi^3 \right], \tag{5.18}$$

which is used to describe percolation at the upper critical dimension [122, 123]. This action is not obtained directly by plugging $d = 6$ into (5.1), so it differs from the previously considered $d = 3$, 4 cases; since the potential is odd, it lacks $\mathbb{Z}_2$ symmetry. This implies the absence of opposing $(+-)$ boundary conditions, which becomes clear when one thinks of the possible boundary conditions for percolation: one can either force a boundary to belong to the percolating cluster $(+)$, or leave

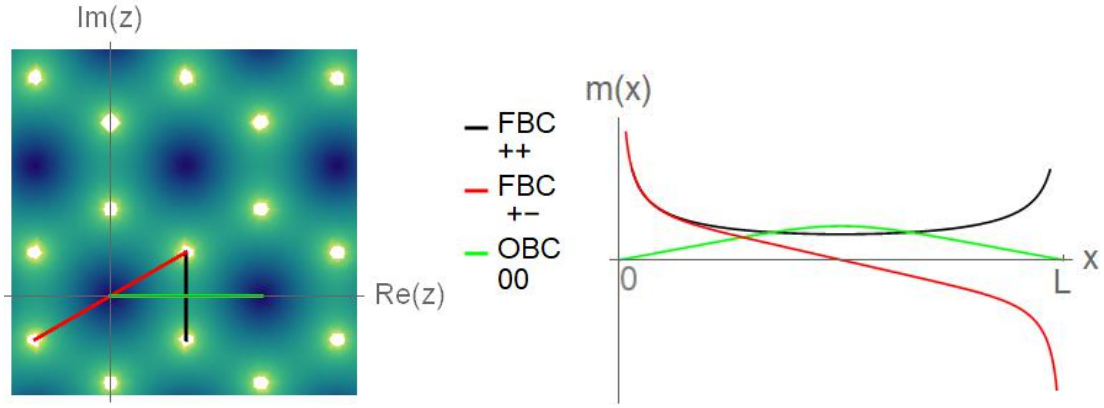

Figure 5.2: As in Fig. 5.1, but here for $d = 6$, the modulus of $m(z)$ in the complex plane, with the solutions for the different boundary conditions.

it free, but opposing boundaries no longer make sense. However, we can still find a solution connecting the + and 0 boundary states. The saddle-point equation now is

$$m''(x) = 6\, g\, m(x)^2. \tag{5.19}$$

The general solution is actually (taking $g = 1$ as in the previous cases) the function $\wp_e$:

$$m(x) = \lambda^2 \wp_e(\lambda\,(x - x_0)), \tag{5.20}$$

meaning that the profiles are just the square of the reciprocal of the ϕ^6 results, as evidenced in Fig. 5.3. Now the double pole in the origin directly yields the expected divergence for the m_{++} order parameter profile, since the dimension of the field is $\frac{d-2}{2} = 2$. The three profiles are now $m_{++}(x)$, $m_{+0}(x)$ and $m_{00}(x)$ and are the following:

$$\begin{aligned} m_{++}(x) &= \wp_e(x) && x \in (0, 2\omega_e), \\ m_{+0}(x) &= \wp_e(x\, e^{i\pi/6}) e^{i\pi/3} && x \in (0, \frac{2\omega_e}{\sqrt{3}}], \\ m_{00}(x) &= \wp_e(\omega_e + i\, x) && x \in [-\frac{\omega_e}{\sqrt{3}}, \frac{\omega_e}{\sqrt{3}}], \end{aligned} \tag{5.21}$$

with the m_{00} solution obtained with a magnetic field $h(x) = 12 g m_{00}(x)^2$.

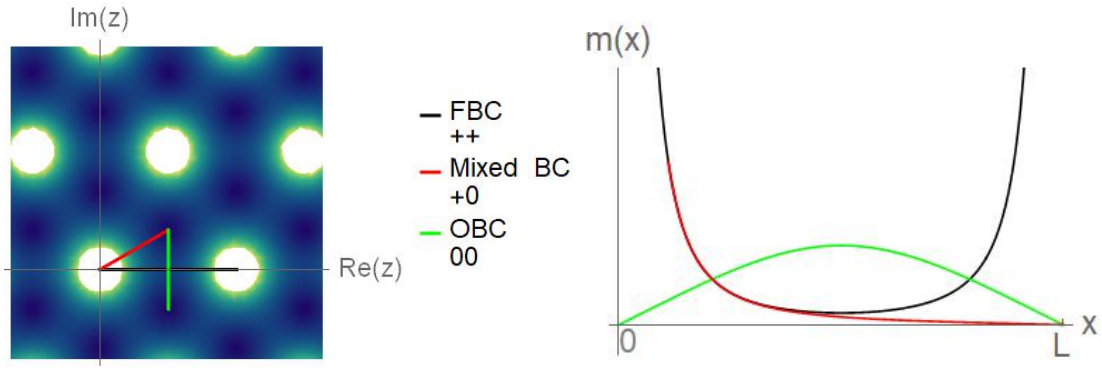

Figure 5.3: The zero and pole structure for $d = 6$ is inverted with respected to Fig. 5.2: this means that the segment representing $++$ BCs now represents 00 BCs. What would be the $+-$ profile now ends at 0, giving the mixed boundary condition $+0$.

5.2 Analytical results for the slab geometry

For the slab geometry we can actually obtain the solution for general dimension d in implicit form. We denote the solution of the Yamabe equation with $\gamma_d(x)$ to emphasize the dependence on the dimension d. For convenience we assume $x \in [0, 2]$ (i.e., $L = 2$), so that the center of the slab is in $x = 1$.

For $x \in [0, 1]$ and FBC, the relation between x and γ_d is given in terms of the ${}_2F_1$ hypergeometric function for FBC. From the Yamabe equation one straightforwardly finds

$$x = {}_2F_1\left(\frac{1}{d}, \frac{1}{2}; 1 + \frac{1}{d}; \left(\frac{\gamma_d}{\gamma_m}\right)^d\right) \gamma_d. \tag{5.22}$$

By reflecting x around 1: $x \to 2 - x$ the other branch is obtained. The constant

$$\gamma_m = \frac{\Gamma\left(\frac{1}{2} + \frac{1}{d}\right)}{\sqrt{\pi}\,\Gamma\left(1 + \frac{1}{d}\right)} \tag{5.23}$$

is the (maximum) value acquired by the conformal factor at the center of the slab. Equation (5.22) is valid for *any* $d \geq 2$, including the cases $d = 4, 6, 3, 2$ and also real values of d. Notice that a slab configuration cannot be defined for $d < 2$. The formulas for other boundary conditions are written below.

We pause here to point out a possible minor advantage using the Yamabe equation in the form (2.11) instead of using directly the saddle-point equation (5.2). The former, when written in the slab geometry, gives rise to the so called Emden-Fowler equation [124]. The latter, for a function $m(x)$, reads in its canonical form $m''(x) =$

$A\,x^{\mathcal{N}} m(x)^{\mathcal{M}}$ [124], with our case corresponding to $\mathcal{N}=0$ and $\mathcal{M}=(d+2)/(d-2)$. The case $\mathcal{N}=0$ can be solved by quadrature [124], writing the solution in term of an integral and for certain values of $\mathcal{M}$ the corresponding analytical expressions are tabulated [124]. However, solving the Yamabe equation (2.11) and using the procedure prescribed in ordinary differential equations textbooks one finds that the solution is given by the inverse of the hypergeometric function ${}_2F_1$ for any d. Therefore, rewriting m in terms of γ via the equation (2.18) may also help to find easier analytical solutions, as the case of the slab geometry shows.

Let us now discuss how to relate the result (5.22) to different boundary conditions. We write the magnetization via (2.18) as $m_d(x)=\gamma_d(x)^{-\Delta_\phi}=\gamma_d(x)^{-\frac{d-2}{2}}$ where $\gamma_d(x)$ is given in (5.22). If in $m_d(x)$ we set $d=3$, 4, and 6 and aptly rescale the x domain we recover the $++$ boundary magnetization profiles given in Section 5.1. This can be achieved by using the identities reported in Appendix 8.6. The other profiles, referring to different boundary conditions, can be found by taking x in (5.22) to be complex according to the following scheme:

$$\begin{aligned} &m_{++}(x)=m_d(x) && x\in(0,2),\\ &m_{+0}(x)=m_d(x\,e^{i\,\pi/d})e^{-i\,\pi\Delta_\phi/d} && x\in(0,\sec(\pi/d)],\\ &m_{00}(x)=m_d(1+i\,x) && x\in[-\tan(\pi/d),\tan(\pi/d)], \end{aligned}$$

where, again, $m_{00}(x)$ solves the saddle-point equation with opposite sign. It is worth observing that the three BCs can be found by evaluating γ on the right triangle $\mathbf{T}=(0,1,1+i\tan(\pi/d))$. Indeed the function $z(w)=w^{1/d}{}_2F_1\left(\frac{1}{d},\frac{1}{2};1+\frac{1}{d};w\right)$ appearing in (5.22) is nothing but the Schwarz function mapping the upper-half-plane (w variable) onto $\mathbf{T}$ (z variable, also x when real) keeping $z=0$ and $z=1$ fixed. In the convenient variable z we have that $\gamma=w^{1/d}$ and $m=w^{-\Delta_\phi/d}=w^{-\frac{d-2}{2d}}$. The above consideration should shed some light on the appearance of the Weierstrass functions $\wp_e$, $\wp_l$ in Section 5.1 and on the peculiarity of $d=3,4,6$: for those values, copies of the triangle $\mathbf{T}$ create a regular tessellation of the complex plane.

Indeed, we can see what the general result (5.22) simplifies to when we substitute $d=4,3,6,2$:

$d=4$: the inverse of (5.22) is $\wp_l(x)^{-1/2}$, the lemniscatic Weierstrass function used in (5.5), see Appendix 8.6.

$d=6$: the inverse is the equiharmonic elliptic function $\wp_e(x)$ as seen in (5.20).

$d=3$: this case is dual to the $d=6$ case, since the solution here is simply the square root of the reciprocal of the previous solution.

$d = 2$: we have seen in Chapter 3 that the value $d = 2$ cannot be directly chosen in the Yamabe equation (2.11): a limit has to be performed, yielding the Liouville equation (3.1). One may then assume that plugging $d = 2$ into (5.22) will give an incorrect result. Surprisingly, that is not the case: for $d = 2$, the function ${}_2F_1(\frac{1}{2}, \frac{1}{2}; \frac{3}{2}; \gamma^2\frac{\pi^2}{4})\gamma$ reduces to the inverse sine: indeed, $\gamma_2(x) = \frac{2}{\pi}\sin(\pi x/2)$, matching (3.6).

They agree with previous results obtained in particular cases: profiles for $++$ and $+-$ boundary conditions were found for $d = 4$ in [125], and for $d = 2$ in [126]; the $++$ profiles for $d = 2, 3, 4$ are also found in [120]. In both [125] and [120] Jacobi functions were used. Switching to Weierstrass functions allowed us in the present paper to write profiles for various dimensions in a compact way, retrieving the previously listed known results, finding new results for all the conformally invariant boundary conditions. We also obtain new results for all the critical magnetization profiles in $d = 6$.

5.3 Solution of lattice mean-field equations

In this section we discuss the solution of the mean-field equations for the Ising model in a slab geometry directly on the lattice. The goal is to see how lattice profiles can be accurately described by a continuous function from field theory in the thermodynamic limit. For this reason in this section we take the slab coordinate x to be an integer variable, going from 1 to L, and then take $L \to \infty$. In this calculation it is not necessary to specify the number of sites in the directions perpendicular to x, since we can assume that the probability distribution function P of any spin depends only on its transverse coordinate x. For this reason we put

$$P(s_i) = \frac{1 + m_x}{2}\delta_{s_i,1} + \frac{1 - m_x}{2}\delta_{s_i,-1}, \tag{5.24}$$

where $s_i = \pm 1$ is the Ising variable in the site i having x as coordinate along the direction of the slab.

We can find the discrete magnetization profile $m_x = \langle s_i \rangle$ minimizing the free energy. The mean-field equation differs slightly from (1.13) as, due to the boundaries, the magnetization is not homogeneous, so we should use Eq. (1.36) for the case of equal couplings everywhere, getting

$$m_x = \tanh\left(\beta \sum_j \langle s_j \rangle\right). \tag{5.25}$$

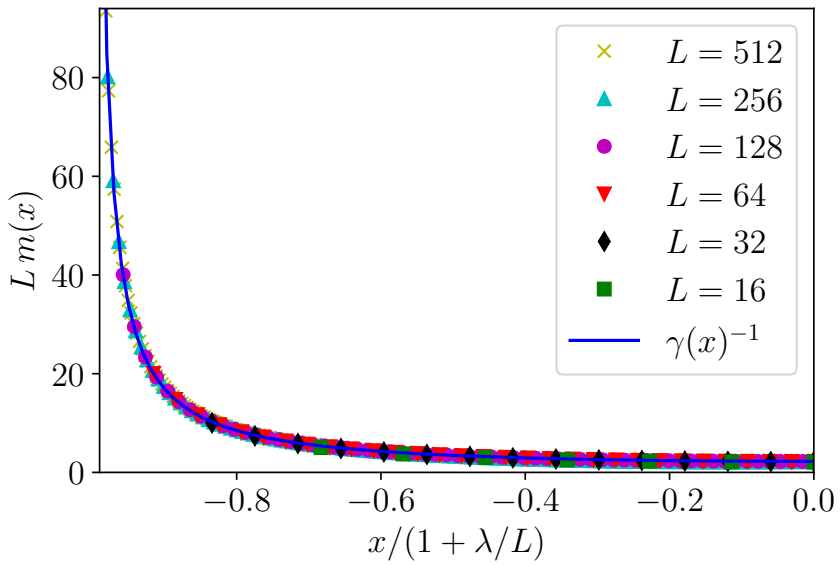

Figure 5.4: Collapse of the mean-field magnetization profiles. Since they are symmetric around the center of the slab, we only plot the left half. Each set of magnetization values has been rescaled by a factor L, while the x coordinate has been rescaled through its extrapolation length.

In a four dimensional slab with $d = 4$, this becomes

$$m_x = \tanh\left[\beta(6m_x + m_{x+1} + m_{x-1})\right]. \tag{5.26}$$

For the case of FBC $m_1 = m_L = 1$, this equation can be solved iteratively until the difference between the two sides is smaller than a fixed threshold. The value of the mean field inverse critical temperature, as found in Section 1.1.3, is $\beta = 1/(2d)$, which of course differs from the actual Ising model critical temperature.

The value of the magnetization at the center of the slab decays, as the system size increases, as $1/L$. Since profiles for different sizes must have the same functional shape at the critical point, we rescale them by multiplying each profile by its corresponding size L. This also clarifies the correspondence between fixing the boundary spins to $+1$ in the lattice model and diverging boundary conditions in the field theory. As the size increases, the rescaled boundary magnetization grows proportional to L.

At the same time, as L increases, the extrapolation length λ [55] remains roughly constant, meaning that λ/L decreases and the point where the profile diverges gets closer to the lattice boundaries. In the limit $L \to \infty$, $\lambda/L \to 0$ and $m(0) = m(L) \to \infty$.

Once the rescaling is done, we clearly see a collapse of the various profiles, showing that we are at the critical point. The corresponding results are in Fig. 5.4. For large L, the extrapolation length vanishes and the mean-field profile coincides with the saddle-point solution. We also studied the solutions of the lattice mean-field equations for $+0$ boundary conditions, finding a similarly good agreement between them and the solution of the corresponding Yamabe equation.

5.4 Simulations of the $4d$ Ising model

The previous predictions have been obtained by performing the saddle-point approximation on the action (5.1). It is very well known that in four dimensions for the ϕ^4 theory, and in general at the upper critical dimension, the critical exponents are the mean-field ones [67, 116, 127, 128]. This is routinely exploited in conformal bootstrap calculations for the bulk geometry, where in $d = 4$ the critical theory is Gaussian [129]. However, in a bounded domain—to the best of our knowledge—there is no proof that the critical magnetization profile in the thermodynamic limit given by the saddle-point approximation is exact in $d = 4$ for the ϕ^4 theory, although it is expected. For this reason we decided to numerically test the saddle-point findings by Monte Carlo simulations and validate our predictions via numerical experiments. In

order to obtain a numerical check of the magnetization profiles, we will concentrate on the Ising model on the slab geometry with FBC. Notice that explicit numerical investigations for high dimensions of phenomena arising from inhomogeneities are rather sparse especially if compared to two-dimensional systems. Three-dimensional models did receive of course attention, and basic predictions from scale/conformal invariance have recently been tested [101, 130].

We performed Monte Carlo simulations of the Ising model at its upper critical dimension, 4, in a slab of sizes L in the transverse direction, and $4L$ in the other three directions; L ranges from 16 to 56. The FBC are implemented by fixing the spins to the same (+1) or opposite ($\pm$1) value on the two faces in the transverse direction, while the other directions have periodic boundary conditions. We can then expect the $++$ and $+-$ magnetization profiles from (5.8). The critical inverse temperature β_c is taken to be $\beta_c = 0.1496927$ from [131], see also [132, 133].

The simulation uses the standard Metropolis algorithm, whose moves are single spin flips. After a thermalization time, we measured the average magnetization and local energy along hyperplanes parallel to the boundaries. As explained in Sections 5.1 and 5.3, since the spins are fixed at the edge faces and one is at the bulk critical temperature, the magnetization profile will start from the value 1 at one boundary, will decrease as one approaches the center, should reach a value of order of $1/L$, and then rise again up to 1 in the other slab boundary. One can rescale the numerical data in a way that the value of the magnetization at the center is constant, meaning that the boundary magnetization increases with L.

L	λ	λ/L
16	3.944	0.2465
24	4.1376	0.1724
32	3.6205	0.1314
40	4.28	0.1070
48	4.2432	0.0884
56	2.2624	0.0404

Table 5.2: Extrapolation lengths as the size increases (++BC): for larger sizes, λ remains of the order of a few lattice sizes, meaning the fraction of the continuous profile accessible to the numerical data widens, as it equals $1/(1 + \lambda/L)$.

Similarly to the previous chapter, the magnetization data is then fitted with

$$m(x) = k \left[\gamma \left(\frac{x}{1 + \lambda/L} \right) \right]^{-1} . \tag{5.27}$$

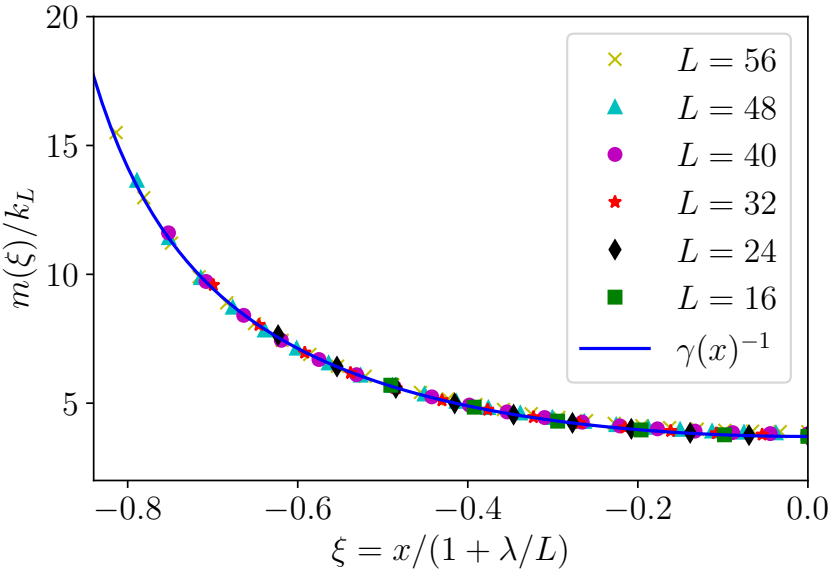

Figure 5.5: Collapse of the critical magnetization profiles in the four-dimensional Ising model for slabs of different sizes with ++ boundary conditions. Again, we only plot half the profile. Each set of points has been rescaled with a multiplicative constant and its extrapolation length, obtained from the fit (5.27).

In Table 5.2, we see that the extrapolation length remain roughly constant as the size grows, meaning that the λ/L ratio becomes smaller as L grows, so larger sizes describe a larger portion of the saddle-point profile. In Fig. 5.5 and 5.6, we plot the magnetization profiles obtained for different sizes, compared with the prediction from (2.18). The magnetization $m(x)$ for different sizes are plotted as functions of the respective rescaled variable $\xi = x/(1 + a_L)$, which highlights the collapse. Simulations with +0 boundary conditions would look like half of the profile shown in Fig. 5.6.

Despite qualitative agreement between the prediction and the numerical data, the distance between raw data points and the theoretical curve is larger than the estimated numerical error (in Figs. 5.5, 5.6 smaller than the point sizes). This is to be expected: while (2.18) gives the correct mean-field behavior, observables at the upper critical dimension also include some logarithmic corrections. To account for them, we proceed as in [131]. At the critical temperature, the main finite size

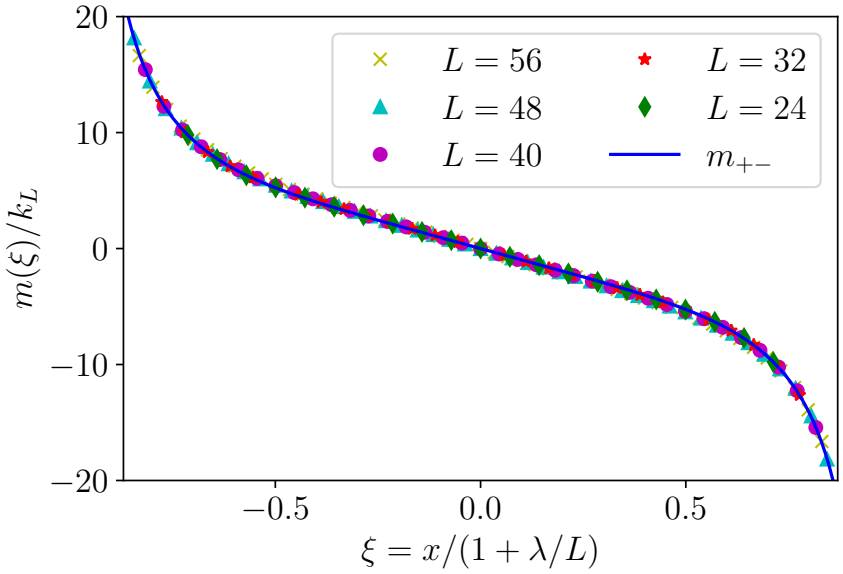

Figure 5.6: Collapse of the critical magnetization profiles in the four-dimensional Ising model for $+-$ boundary conditions.

corrections to the bulk magnetization take the form

$$m = c\frac{(\ln L)^{1/4}}{L}\sqrt{b_0 + \frac{b_1}{\ln L} + \frac{b_2}{(\ln L)^2}}, \tag{5.28}$$

where terms with higher powers of $1/\ln L$ have been neglected. In our case, the magnetization is a function of x (or rather of the rescaled coordinate ξ), and therefore so are b_0, b_1 and b_2. For every ξ we find the values of $b_0(\xi)$, $b_1(\xi)$ and $b_2(\xi)$ which best fit $m(\xi, L)$, seen as a function of $L = \{16, 24, 32, 40, 48, 56\}$ [1].

In order to compare with the analytical prediction (5.8) for $++$ BC, the constant c in (5.28) is chosen so that $\sqrt{b_0(0)} = m(0)$. We then plot, in Fig. 5.7, the ratio $\sqrt{b_0(\xi)}/m(\xi)$, and we see that it remains close to 1. As we approach the boundaries, the value of the first logarithmic correction b_1 grows, explaining the deviation of the ratio from 1. Larger values of b_1 simply imply that it is numerically harder to measure the values predicted by (2.18) near the boundaries, as it requires simulating even larger systems.

[1] Notice that in [131] the (bulk) $4D$ Ising model at criticality is studied for linear sizes L' from 2 up to 48 (to match with our notations, the hypercube in [131] is $L' \times L' \times L' \times L'$, while our slab is $4L \times 4L \times 4L \times L$).

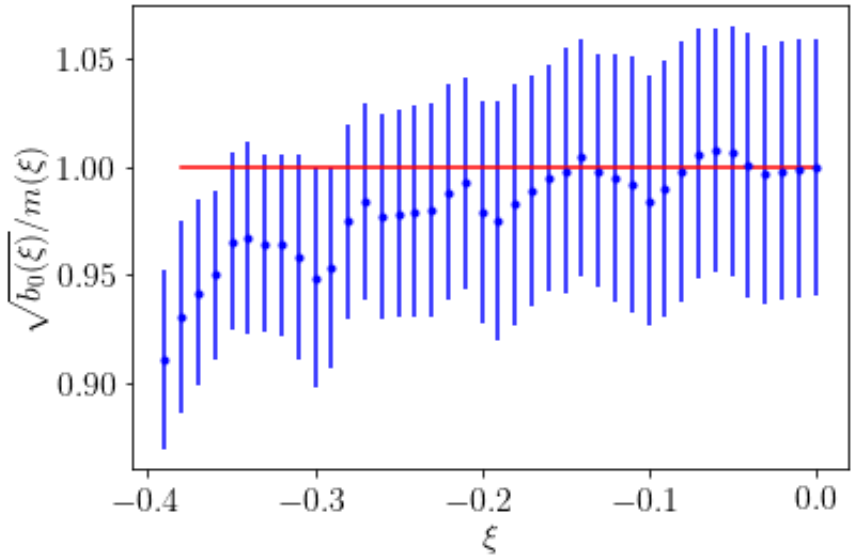

Figure 5.7: Ratio of the square root of the fit parameter b_0 and the expected magnetization (++BC). The boundary $x = -1$ correspond to $\xi = -1/(1 + a_L)$, and the first few points close to the boundary must be discarded, so the plot starts from $\xi = -0.39$.

From $\xi = -1$ to $\xi = -0.4$ we decided not to plot the ratio $\sqrt{b_0(\xi)}/m(\xi)$ since, due to the values of the extrapolation length, for these ξ's we do not have points for each of the considered values of L. We remind that we are in the left part of the slab geometry, $\xi = 0$ corresponding to the center and $\xi = -1$ to the left edge (we discretize ξ in steps of 0.01). We notice that by fitting the points from the magnetization using (5.28) without the logarithmic corrections one obtains a clearly worse estimate of the χ^2, confirming the validity of the fitting function (5.28). Moreover, for any ξ we find $b_0 > b_1/\ln L_{max} > b_2/(\ln L_{max})^2$, where $L_{\max} = 56$ is the maximum value of L we were able to simulate. This shows that each successive term is a smaller correction to the infinite-size term, proportional to b_0. The standard deviations σ in Fig. 5.7 are obtained by fitting the magnetization points without weighting them with their respective errors. The point for $\xi = 0$ has ratio $\sqrt{b_0(\xi = 0)}/m(0) = 1$ by construction, and with standard deviation — determined as explained above — $\sigma = 0.04$. The final result, depicted in Fig. 5.7, shows that $\sqrt{b_0(\xi)}$ is compatible with $m(\xi)$ within σ for $-0.32 \leq \xi \leq 0$ and within 2σ for $-0.39 \leq \xi \leq -0.33$. To obtain more data in the range $-1 < \xi \leq -0.4$ one should have larger sizes. Similar results are obtained for the $+-$ data reported in Fig. 5.6.

The conclusion is that for the available data, the analytical predictions is in agreement with the Monte Carlo numerical results within 2σ.

5.5 Energy profile

Next, we can measure in the same way the local energy, defined as

$$e_i = -\frac{1}{2}\sum_{\langle j \rangle} s_i s_j. \tag{5.29}$$

More details about the energy field are in the next chapter. At the upper critical dimension, the energy field, identified with the ϕ^2 operator, has scaling dimension $\Delta_\epsilon = 2\Delta_\phi$, so for $d = 4$, $\Delta_\epsilon = 2$.

One can then try and fit the energy profile with the square of the function used for the magnetization profile (5.27), i.e.

$$\epsilon(x) = k\left[\gamma\left(\frac{x}{1+\lambda/L}\right)\right]^{-2}. \tag{5.30}$$

The results are seen in Fig. 5.8. We see qualitatively good agreement between points and the fitted function (5.30). But are we justified in doing this? We claim that the fractional Yamabe equation reduces to the integer version for $\Delta_\phi = \frac{d-2}{2}$,

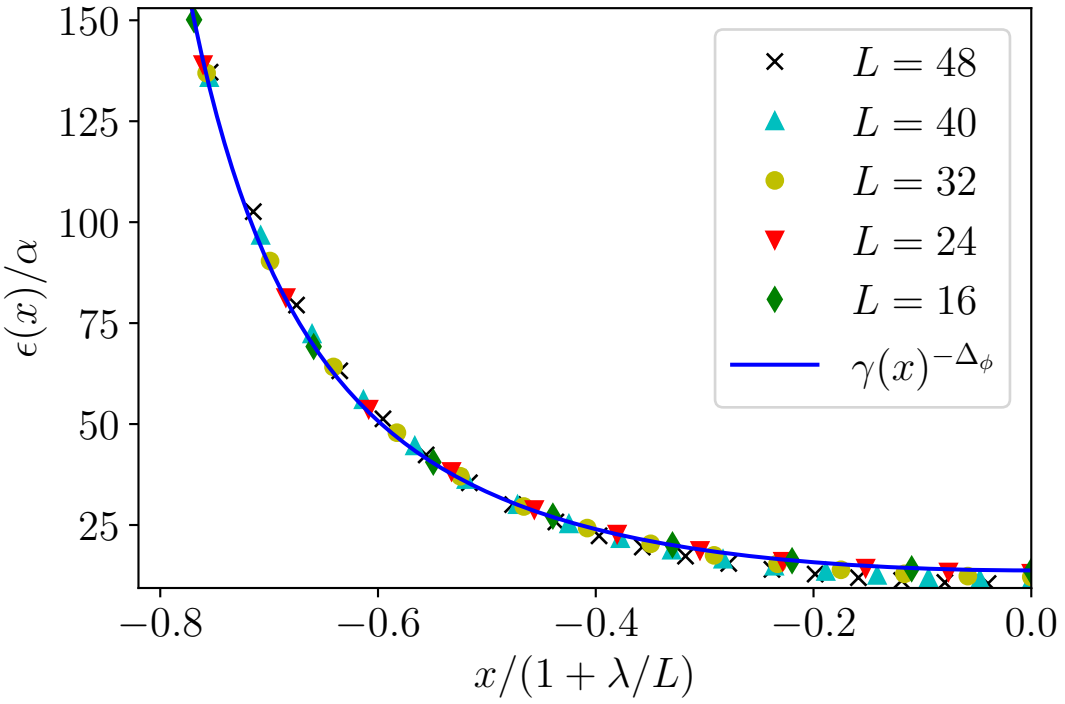

Figure 5.8: Energy profile for various sizes of the four-dimensional Ising model in a slab. The constant term for the bulk energy has been subtracted from each profiles, so that they all approach zero for large distance from the boundaries.

but here we are using the solution to that same equation for a field with scaling dimension which is twice that. Should we not use a different equation specific to the energy field? This is the question that the next chapter tries to answer.

Chapter 6

Energy field

6.1 Uniformization beyond the order parameter

So far, we used the uniformization approach to obtain one- and two-point correlation functions for the order parameter field. Because of the purely geometric nature of this approach, there is nothing preventing us from using it to obtain correlation of other fields. In particular, we will now focus on the energy density fields, for two reasons: first, because like the order parameter, the corresponding lattice observable can be measured straightforwardly in spin systems; secondly, it has much larger scaling dimension than the order parameter, whose importance will become clear soon.

The question is now: what should correlation functions of different fields in the fractional Yamabe framework look like? Two possibilities emerge:

1. **Complete uniformization**: the solution of the fractional Yamabe equation for the order parameter, $\gamma_{(\Delta_\phi)}$ also rules correlation functions of other fields, e.g.
$$\langle \epsilon(x) \rangle = \alpha \gamma_{(\Delta_\phi)}(x)^{-\Delta_\epsilon}. \tag{6.1}$$

2. **Operator uniformization**: for each field, one has to solve a different fractional Yamabe equation, for the corresponding scaling dimension:
$$(-\triangle)^{d/2-\Delta_\epsilon} \gamma_{(\Delta_\epsilon)}(\mathbf{x})^{-\Delta_\epsilon} \propto \gamma_{(\Delta_\epsilon)}(\mathbf{x})^{-d+\Delta_\epsilon}, \tag{6.2}$$
so that
$$\langle \epsilon(x) \rangle = \alpha \gamma_{(\Delta_\epsilon)}(x)^{-\Delta_\epsilon}. \tag{6.3}$$

The first case has a more pleasant geometric interpretation: the bounded system can be fully described by a single metric, and all correlation functions depend on the distances between points computed using such metric. The fields whose scaling dimension determines the metric is the order parameter, being both the most relevant field and the one that can be directly measured on the lattice. However, from a Conformal Field Theory point of view, different primary fields should be independent: if one forgets about the lattice meaning of the magnetization and energy fields, there is no a priori reason why the correlation of the latter should depend on the former.

On the other hand, "operator uniformization" means that each field in the theory is given the same importance: for every scaling dimension, one has to solve a different fractional Yamabe equation, and its solution only dictates the correlation functions of the respective field. This means there is no single metric which describes the systems, but rather a collection of metrics, each describing a field. In this framework, there is currently no way to determine correlation functions of different fields. For example, what would mixed correlation functions such as

$$\langle \phi(\mathbf{x})\epsilon(\mathbf{y})\rangle \quad \text{or} \quad \langle \phi(\mathbf{x})\phi(\mathbf{y})\epsilon(\mathbf{z})\rangle \tag{6.4}$$

look like? They must depend on the distance between the points, but which metric should be used is not clear. It should be noted that the mixed two-point function of the order parameter with the energy field vanishes in the bulk, since the Operator Product Expansion between ϕ and ϵ does not contain the identity operator, but in a bounded system with fixed boundary conditions it is nonzero.

Theoretical reasons can be given to in support of complete uniformization, although the existence of two (or more) independent primary fields would in essence be a reason in favor of operator uniformization. Without entering such discussion, in the present chapter we limit ourselves to presenting preliminary unpublished material in which we resort once again to numerical simulations to discriminate between the two hypotheses. For the three-dimensional improved Ising model, we perform Monte Carlo runs in which we additionally measure the local energy, which is of course defined as

$$e_i = -\frac{1}{2}\sum_{\langle j\rangle} s_i s_j + D s_i^2. \tag{6.5}$$

As a reminder, the D term appears in the improved models where a spin can also be zero, and it represent the energy cost to have a spin on a lattice site.

So Eq. (6.5) represents the contribution to the total energy due to the spin $\mathbf{s}_i$. The factor $\frac{1}{2}$ in front of the interaction term is there to account for the fact that the energy of a bond is "split" between the two spins: this way,

$$\sum_i e_i = H. \tag{6.6}$$

Next, we should remember that in any conformal field theory, the bulk average of a field at the critical point vanishes, $\langle \epsilon(x) \rangle = 0$. This means that the local energy on the lattice is not exactly the energy field, as the mean bulk energy has to be subtracted first:

$$\epsilon(x) = e(x) - \langle e(x) \rangle_{\text{bulk}} . \tag{6.7}$$

This introduces a further parameter in the fit[1]:

$$\langle \epsilon(x) \rangle = \alpha \left[L \, \gamma \left(\frac{x}{1 + \lambda/L} \right) \right]^{-\Delta_\epsilon} + e_0. \tag{6.8}$$

This same fit was performed for both the Ising and the XY model. Our aim is not to determine the value Δ_ϵ, since the current precision of the fractional Yamabe approach cannot compete with the conformal bootstrap, but rather to distinguish between our two hypotheses.

To do so, we can solve the fractional Yamabe equation for $\Delta_\epsilon^{\text{CB}} = 1.412625$ for the Ising model, which is the most precise value currently available, coming from [96][2]. These solutions are obtained with the same procedure as explained in Section 2.2. For each model, the data points can then be fitted with both of the following functions:

[1]There is another option: simulations of the same system with open boundary conditions were also performed, from which the bulk energy was measured and subtracted from the energy profile of the bounded system to obtain the profile of the energy field. The approach of letting this value be determined by the fit was eventually deemed the better choice.

[2]An alternative route that avoids relying on the conformal bootstrap results is also worth pursuing. To test the operator uniformization conjecture, the fractional Yamabe equation can be solved in a neighborhood of the respective exponent, as was done for the magnetization. While such a solution was obtained, the best way to compare its result to the complete uniformization results is not trivial. One option is to allow the fit for the energy profile in Eq. (6.1) to determine both Δ_ϕ and Δ_ϵ at the same time, since the former appears inside the function γ and the latter appears as the exponent. This would however necessitate extraordinarily accurate data. Alternatively, Δ_ϕ in the complete uniformization hypothesis could be fixed as the best value we obtained in Chapter 4. This would lead to results which are practically indistinguishable from the ones we present here, since the fractional Yamabe equation varies so slowly as a function of Δ_ϕ that the conformal bootstrap value and our value gives almost identical profiles.

$$
\begin{aligned}
&1. \qquad \langle \epsilon(x) \rangle = \alpha \left[L \; \gamma_{(\Delta_\phi)} \left(\frac{x}{1+\lambda/L} \right) \right]^{-\Delta_\epsilon} + e_0. \\
&2. \qquad \langle \epsilon(x) \rangle = \alpha \left[L \; \gamma_{(\Delta_\epsilon)} \left(\frac{x}{1+\lambda/L} \right) \right]^{-\Delta_\epsilon} + e_0.
\end{aligned}
\tag{6.9}
$$

The solution to the fractional Yamabe equation varies smoothly and quite slowly with its exponent. For this reason, despite Δ_ϕ and Δ_ϵ differing by roughly 1, the two corresponding fractional Yamabe equations are surprisingly similar, making it more difficult to determine numerically which hypothesis better describes the data.

6.2 Energy for the Ising model

The same "windowing" procedure used for the magnetization data, explained in Chapter 4.1.4, has been applied. Using the complete uniformization conjecture (6.1), discarding the first point (the one on the boundary, whose energy only depends on the value of the single non-fixed spin it interacts with) is enough to obtain a satisfying fit. Using the operator uniformization conjecture (6.3), around three points needs to be trimmed before the χ^2 reaches a low enough value (corresponding to $\int_0^{\chi^2} p_{\chi^2}(\xi) d\xi < 0.95$.) The only exception was the $L = 128$ case, where it became apparent that the thermalization process takes too long to be able to obtain accurate measurements, as can be seen by the inconsistent value of the fitted $\Delta_\epsilon^{L=128}$ and its large corresponding error.

As we can see from Table 6.1, using the first conjecture gives values closer to the bootstrap result $\Delta_\epsilon^{\mathrm{CB}} = 1.412625(10)$ [96], but neither of them is especially accurate. It should be noted, however, that obtaining a precise value for this exponent is not our main goal here. The point of the simulation for the energy field is to determine which of the two possibilities is (more likely to be) correct: after all, the fractional Yamabe equation for operator uniformization, γ_{Δ_ϵ} has been obtained specifically for the value of $\Delta_\epsilon^{\mathrm{Bootstrap}}$, meaning that we already assume knowledge of Δ_ϵ, so the value we obtain as fit exponent can be used to discriminate between the two hypotheses, but cannot be considered a prediction. So far, complete uniformization (6.1) requires less trimming to fit the profile and gives a value of Δ_ϵ closer to the best estimate: these are two points in favor of it. Another route to compare the two is to avoid any determination of Δ_ϵ, since as we said this is not our goal, and perform fits using again Eq. (6.9), but now with having fixed $\Delta_\epsilon = \Delta_\epsilon^{\mathrm{CB}} = 1.412625$. In this case the only fit parameters are the multiplicative constant α and the extrapolation length λ. Rather

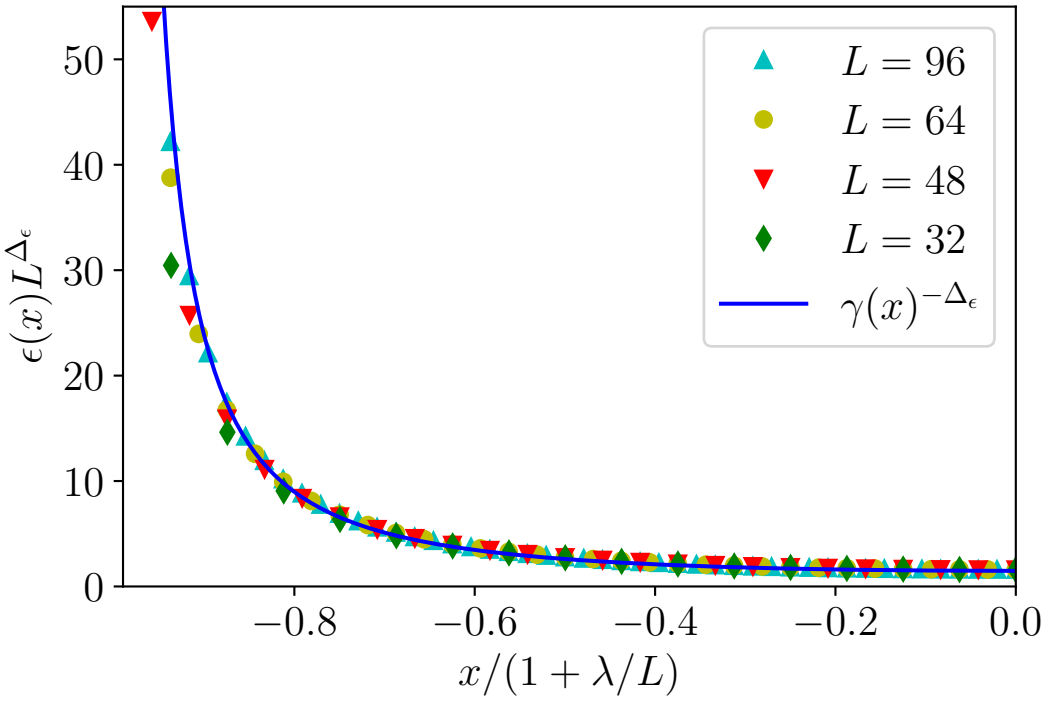

Figure 6.1: Ising energy profile after the bulk energy has been subtracted. The continuous line represents the solution assuming the first conjecture, but the other solution is so similar they would appear as the same line.

L	Δ_ϵ (1^{st} conj.)	Δ_ϵ (2^{nd} conj.)
16	1.4250(24)	1.663(77)
24	1.4231(17)	1.551(22)
32	1.4197(14)	1.4719(90)
40	1.4228(6)	1.517(14)
48	1.4201(6)	1.4505(37)
56	1.4239(7)	1.4560(34)
64	1.4212(7)	1.4446(28)
80	1.4199(6)	1.4256(6)
96	1.4205(6)	1.4435(35)
128	1.19(4)	1.2116(1)

Table 6.1: Best fit values of the energy scaling dimension for different sizes of the Ising model, assuming complete uniformization on the left and operator uniformization on the right. To be compared to $\Delta_\epsilon^{\text{CB}} = 1.412625(10)$.

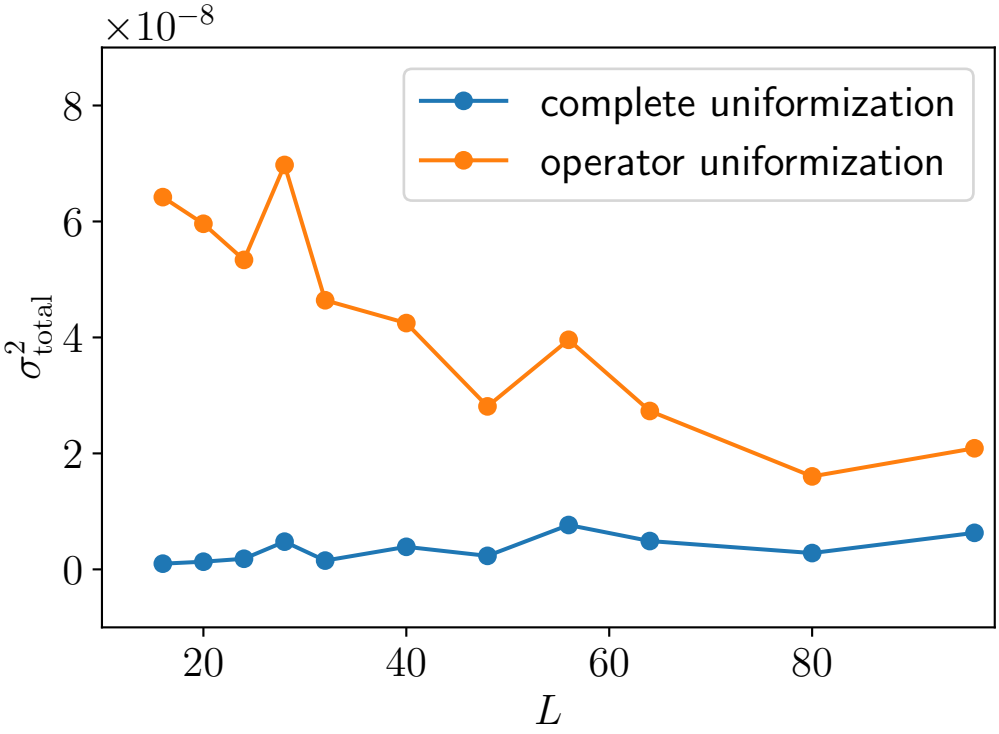

Figure 6.2: Sum of the mean square distances between the Ising energies measured from Monte Carlo simulation and the value predicted for the energy profiles, for the two options. The hypothesis which uses $\gamma_{(\Delta_\phi)}$ gives a better fit, since the distances are smaller.

than using the "trimming" technique, this time we only discard the first point: this way we can directly compare the mean square errors for the two hypotheses.

This way, for each size we can compare the sum of the mean square distances between the points and the fitted function,

$$\sigma^2_{\text{total}} = \sum_{i=0}^{\frac{L}{2}} \left(\epsilon_i^{\text{exp}} - \langle \epsilon(i/L) \rangle \right)^2. \tag{6.10}$$

The results for the various system sizes are shown in Fig. 6.2. We clearly see that for each system size, the total square error is lower by using $\gamma_{(\Delta_\phi)}$.

6.3 Summary

We can now come to some conclusions. We used three different ways to test which of the two hypothesis is more likely to be correct: better estimate of Δ_ϵ, fewer points needed to be discarded to obtain a good fit, quality of the fit using the best value for Δ_ϵ. For all three tests, complete uniformization performs better than the alternative on all sizes.Preliminary results for the Clock model seem to confirm that complete uniformization performs better for the XY universality class as well.

Of course, more tests would be needed to draw stringent conclusions, and further arguments in favour of the conjecture are very desirable. Nevertheless, we can claim that the fractional Yamabe solution in a given domain for a value of the scaling dimension equal to that of the order parameter field can describe to good accuracy the correlation functions of both the order parameter and the energy fields.

Chapter 7

Conclusions

In this thesis, after a recap on critical phenomena in the full space and in bounded domains, we presented the uniformization hypothesis based on the fractional Yamabe equation. We explained how to construct the fractional laplacian and solve the corresponding equation, and obtained a prediction for correlation functions in critical bounded systems.

The original work consisted in applying this theory, after ensuring its validity in $d = 2$, to three-dimensional models, in particular the XY model and percolation, to test the prediction for one- and two-point functions, and to obtain the respective exponent Δ_ϕ. To extend the theory to fields other than the order parameter, the XY model has been studied alongside the Ising model to obtain energy parameter profiles. At the upper critical dimension, the solution of the saddle-point equations equivalent to the integer Yamabe equation have been related to the zero and pole structures of Weierstrass elliptic functions.

Overall, this has provided additional pieces of evidence in support of the uniformization approach, but there is still a lot that could be learned about it, so in the following I will mention some directions which are worth exploring.

The most obvious follow-up one could take would be to study $O(N)$ models with higher values of N. We studied the Ising and the XY models, so $N = 1, 2$, and obtained different correlation ratio curves. How would this function look for the Heisenberg model? Knowing more about it could, optimistically, lead to a general form of the function of the distance $\mathcal{F}$ from Eq. (2.21), maybe even expressed as a function of N, valid for all $O(N)$ models. Numerical simulations of models with $N > 2$ may be cumbersome, however.

On the topic of $O(N)$ models with larger N, the $N \to \infty$ limit is also potentially interesting. For infinite systems, an old and famous result [134] shows that the free

energy per component of an $O(N \to \infty)$ model coincides with that of the spherical model by Berlin and Kac [135]. Some results exist on infinite-N limits for systems which are not infinite in all directions, like a slab which is just a few layers thick [136] or systems with more general interaction [137]. The model most suited to our favorite geometry (a slab with many layers) is the so-called mean spherical model, where the spherical condition is enforced through a sort of chemical potential μ, tuned so that the average of each spin is 1, rather than the exact spherical model, which fixes the value of $\sum_i s_i^2$ through a delta function. The reason for this is that on a slab, each layer can have its own value for the chemical potential, leading to what is basically a stack of spherical models interacting with each other. The main issue is to find a way to solve analytically the equations that give the value of each μ. Determining what we mean by fixed boundary conditions in this case is also nontrivial.

The reason why the spherical model can be interesting is that it has no anomalous dimensions $\eta = 0$. Therefore, one might argue that the integer Yamabe equation should apply to it for any dimension where it features a transition. On the other hand, its actions at the critical point coincides with that of a Gaussian model, which means its equation of motions would be that of a free particle and it might therefore not satisfy the Yamabe equation.

While for models in the $O(N)$ class, $d = 3$ is the only "interesting" dimension, since it lies below the upper critical dimension but still above $d = 2$, percolation has $d_c = 6$, which means that nontrivial critical exponents exist also for $d = 4, 5$. It may be worth trying to obtain them with the critical geometry approach. Numerical challenges may arise if one wishes to surpass the most precise determinations of Δ_ϕ to date: while their errors are comparable to the error of previous determinations of $\Delta_\phi^{(3d)}$, one can expect the precision of our approach to decrease as the dimensionality increases, due to the longer times needed for simulations. In those cases, lattice percolation, however less elegant and less fit for description of continuum profiles, might prove more efficient.

Continuum percolation may also provide with a way to analyze geometries other than a slab. For example, the Yamabe equation can be solved in a sphere, but it is impractical to define a lattice spin model on any curved geometry. Continuum percolation dodges this issue, since one can generate objects in a region of space, and then define any surface as the domain boundary, as was done in [101].

Finally, the most ambitious goal would be to derive the uniformization approach from general principles and, possibly, from the principles of conformal field theory. If that will turn out to be possible, one might be able to know more about how this approach can describe correlation functions of different fields and deal with boundary-condition-changing operators.

Chapter 8

Appendix

8.1 Solving the fractional Yamabe equation on a slab

We defined the conformal fractional laplacian as a scattering operator on an extended $d+1$-dimensional space, but we still need an algorithm to compute it. First of all, we can require that the extension metric on Θ be an Einstein metric, i.e. it satisfies the vacuum Einstein field equations with cosmological constant chosen so that

$$R_{(g_+)} + d\, g_+ = 0. \tag{8.1}$$

As the extension coordinate y we can use an angle, call it θ, where $\theta = 0$ corresponds to the physical space Ω. Using the geometry of a slab simplifies the problem considerably, since the metric is independent from the two directions parallel to the slab x_2, x_3. g_+ can then always be put in a diagonal form where

$$g_+ = \frac{1}{\sin^2\theta}\left(d\theta^2 + \frac{dx^2}{\gamma_x(x,\theta)^2} + \frac{dx_2^2 + dx_3^2}{\gamma_\parallel(x,\theta)^2}\right). \tag{8.2}$$

We started from the idea of looking for a metric in the same conformal class as the identity and now we have a metric which clearly lacks this property, but one should remember that this is the extended metric, and being in the same class as the identity is a requirement for the physical metric g. In fact, this requirement is satisfied just by requiring $\gamma_x(x,0) = \gamma_\parallel(x,0)$. Next, to solve Eq. (2.44), we need to expand the input and output functions appearing in Eq. (2.45), first in powers of

x	$\gamma(x)$
-1	0
-0.9	0.099965
-0.8	0.199440
-0.7	0.297174
-0.6	0.391147
-0.5	0.478688
-0.4	0.556675
-0.3	0.621813
-0.2	0.670996
-0.1	0.701632
0	0.712034

Table 8.1: Values of the solution of the fractional Yamabe equation on the left half of a slab for some values of the coordinate x, for $\Delta_\phi = 0.47846$.

$\sin\theta$:

$$u = (\sin\theta)^{\Delta_\phi} \left(\sum_{i \text{ even}}^{N_\theta} f_i(x)(\sin\theta)^{2i} + \sum_{i \text{ odd}}^{N_\theta - 1} f_i(x)(\sin\theta)^{2i-1} \right), \tag{8.3}$$

and then the f_is are expanded in powers of x. We use the even Chebyshev polynomials T_{2j} as our basis:

$$f_i = \sum_{j=0}^{N_x} T_{2j}(x)\varphi_{i,j}. \tag{8.4}$$

Once both variables θ and x are discretized, the eigenvalue problem (2.44) turns into a matrix equation for the coefficients $\varphi_{i,j}$.

Numerical values of the solution of the fractional Yamabe equation on a slab used for the case of percolation in Chapter 4 at the fitted value of Δ_ϕ is found in Table 8.1.

8.2 Simulation and data analysis of the clock model

To ensure the validity of the simulations described in the main text, the following tests have been performed:

- The critical temperature obtained in [23] has been checked by computing the Binder cumulant [138] in a system without fixed boundaries.

- The system has also been simulated at $\beta_c + \sigma_{\beta_c}$ and at $\beta_c - \sigma_{\beta_c}$ (with $\beta_c = 0.56379622$ and $\sigma_{\beta_c} = 10^{-7}$): the resulting magnetization profiles are compatible with the ones obtained at β_c, i.e. they are within the respective statistical errors. This means that, for the studied sizes, the uncertainty on the critical temperature does not affect our results. However, further increasing the size L, the uncertainty on the location of the critical point could affect the results, and supplementary studies would be necessary.

- The profiles have been obtained for various ratios between the length in the parallel directions and in the transverse direction. The final value we chose is 6, since increasing it further does not change the profiles beyond statistical uncertainties.

- Additional small-size simulations were performed using only single-spin flips, without cluster update, as a cross-check: once again, we verified that the results were compatible with the ones obtained from the employed optimized algorithm, which includes cluster updates.

For any system size L, two-to-four-day simulations were performed on up to 160 Intel(R) Xeon(R) CPUs E5-2680 v2 cores running at 2.80GHz.

8.3 Union/find algorithm for continuum percolation

For the sake of clarity, I will describe the algorithm used for the three-dimensional case; the two-dimensional version follows the same concept.

The main difficulty of simulating continuum percolation, compared to the lattice variants [108], is to locate the objects that intersect the newly added one. To do this for the case of spheres, the entire slab has been divided in cubes of size equal to the diameter of a sphere. Since we take the diameter of the spheres to be 1, the number of these boxes will be $N = L \times 4L \times 4L$. Two matrices C and P are then introduced, with N rows and variable number of columns, whose elements are themselves arrays: they will store, respectively, the coordinates of the sphere centers and a pointer. A new sphere is added by generating the coordinates of its center, uniformly within the slab. From them, we determine to which box it belongs, say the n^{th} box, which already contained k balls: an array containing the three coordinates is added to $C_{n,k}$, and we also set $P_{n,k} = (-1, 0)$, to signify that the new sphere does not yet belong to

any cluster. Then, we locate all the boxes that could contain spheres intersecting the newly added one: if box n is not on a boundary, we have to check 27 boxes, a $3\times3\times3$ grid centered in n. For each sphere in one of these boxes, we compute the distance between the two centers: if this is less than the sphere diameter, then an intersection has happened. Now we need to obtain the cluster to which the neighboring sphere belongs, and if it not the same as the cluster of the new sphere, the two will be merged. This is done by a "union/find" algorithm [139]. The idea is to label each sphere so that it points to a sphere in the same cluster. The cluster can then be considered a tree, with various branches growing from one root. The first step is defining a find function: when it is fed the values representing a sphere, (n, k), it looks at the values in $P_{n,k} = (n', k')$. If n' is negative, by convention, it means that the k'^{th} sphere in box n' is the root of its cluster. Otherwise, the search continues, as we find the point that (n', k') points to: $P_{n',k'} = (n'', k'')$.
In order to shorten the path for the next time the function is be called, once the root is found, the pointer of every sphere along the branch is changed so that it points directly to the root. Next is the "union" part of the algorithm. Once the root of the intersecting sphere is known, if it is the same as the newly added sphere, nothing needs to be done. If the two roots differ, the smaller cluster must be included into the larger one, simply by changing the pointer of its root to the root of the larger cluster. Adding the smaller cluster to the larger one ensures that the average path to the root is shorter, but it might seem that additional effort is required to keep track of the cluster size. However, there is some convenient space to store this information that so far has not been used: the pointer of a root. While the pointer of every other sphere is the location of another sphere, so far we only specified that for a root site (m, q), $P_{m,q} = (\alpha, \beta)$ with $\alpha < 0$ to distinguish it from other sites. We can set $-\alpha$ to be equal to the number of sites in the cluster, and $\beta = 0$ since it does not need to contain any information. Now, when this cluster is merged with another one with root (m', q') and $P_{m',q'} = (\alpha', 0)$, assuming $|\alpha| > |\alpha'|$, we just have to set $P_{m',q'} = (m, q)$ and $P_{m,q} = (\alpha + \alpha', 0)$. This links the smaller cluster to the larger one and updates the size of the latter.

The entire process repeats by adding new balls until the critical filling ratio η_c is reached. The main perk of this algorithm is that each union/find step takes an effectively constant computational time, i.e. it grows extremely slowly with system size. This means that the time to run the entire simulation is, for all practical purposes, simply proportional to the number of balls needed to reach the critical filling fraction.

As mentioned in the main text, we want to implement fixed boundary conditions. To do so, we add a special object, which is adjacent to all the balls whose center is

in a box on either boundary. This ensures that the balls in the first or last layer of boxes all belong to the same cluster, which is then the percolating cluster.

8.4 Data analysis and tests for percolation

After obtaining the order parameter profiles, by averaging the results of a few thousand realizations, an additional step is needed before performing the fit. The points closest to the boundary are most affected by finite-size effects. Therefore, despite having smaller errors than the central points, a few of them have to be discarded. In order to determine how many to discard in an unbiased way, as well as to avoid a sharp distinction between discarded and included points, we introduce a window function $w(x)$. The weight of each point in the fit is given by the square of the ratio between this function and the error of that point. This function starts off from 0 at the boundary, ramps linearly to 1 around a movable point t, and maintains the value 1 up to the center of the slab.

To determine the location of the point t, we start from $t = -1$ (the boundary point) and gradually move towards $t = 0$. For each value of t we compute the χ^2 of our data, and the corresponding p-value. We stop once the p-value reaches the reference value $p = 0.95$.

Some more tests are need to ensure that the errors on the critical filling ratios do not meaningfully affect our results. To that end, we checked that simulations performed at $\eta_c + \sigma_{\eta_c}$ and at $\eta_c - \sigma_{\eta_c}$ give profiles indistinguishable within the error, where σ_{η_c} is the error given in [100] (2d) and [106] (3d). In particular, for small sizes and especially in $2d$, where σ_{η_c} is very small, varying the number of balls by just one changes the filling ratio from below $\eta_c - \sigma_{\eta_c}$ to above $\eta_c + \sigma_{\eta_c}$. This does not alter the profile and the subsequent Δ_ϕ, either in $2d$ or in $3d$.

8.5 Weierstrass elliptic functions

Elliptic functions appear in numerous areas of physics. They get their name from their property of being the inverse of elliptic integrals.
A complex function of one complex variable $f(z)$ is called elliptic if it is meromorphic (its only singularities are poles) and is doubly periodic, i.e.,

$$f(z + 2\omega_1) = f(z), \qquad f(z + 2\omega_2) = f(z), \tag{8.5}$$

with $\omega_1/\omega_2 \notin \mathbb{R}$. ω_1 and ω_2 are called half-periods. The double periodicity induces a tessellation of the complex plane in parallelograms. It is therefore sufficient to know the values of the function within one of these parallelograms, say the one with vertices 0, $2\omega_1$, $2\omega_2$ and $2\omega_1 + 2\omega_2$.

The Weierstrass $\wp$ function is probably the most intuitive elliptic function to construct, starting from the definition and the requirement of having only a double pole within each cell:

$$\wp(z) = \frac{1}{z^2} + \sum_{(m,n)\neq(0,0)} \left(\frac{1}{(z + 2\,m\,\omega_1 + 2\,n\,\omega_2)^2} - \frac{1}{(2\,m\,\omega_1 + 2\,n\,\omega_2)^2} \right). \tag{8.6}$$

Instead of the half periods, the Weierstrass function can be identified with another pair of numbers, g_2 and g_3, called invariants. They are the lowest order coefficients in the Laurent expansion of $\wp$ around 0:

$$\wp(z) = \frac{1}{z^2} + \frac{g_2}{20} z^2 + \frac{g_3}{28} z^4 + O(z^6). \tag{8.7}$$

The invariants can be obtained from the half periods as

$$\begin{aligned} g_2 &= 60 \sum_{(m,n)\neq(0,0)} \frac{1}{(2m\omega_1 + 2n\omega_2)^4} \\ g_3 &= 140 \sum_{(m,n)\neq(0,0)} \frac{1}{(2m\omega_1 + 2n\omega_2)^6}. \end{aligned} \tag{8.8}$$

The importance of the invariants comes from the fact that they appear in the differential equation that the Weierstrass function obeys:

$$\wp'^2(z) = 4\wp^3(z) - g_2\wp(z) - g_3 = 0. \tag{8.9}$$

The particular cases encountered in the text are:

- $(g_2, g_3) = (1, 0)$, called lemniscatic elliptic function $\wp_l$ here, which gives orthogonal semiperiods $\omega_1 = \omega_l = \Gamma(\frac{1}{4})^2/(4\sqrt{\pi})$, $\omega_2 = i\omega_1$, that tessellate the complex plane with squares.

- $(g_2, g_3) = (0, 1)$, the equiharmonic case $\wp_e$ here, with $\omega_1 = \omega_e = \Gamma(\frac{1}{3})^3/(4\pi)$ and $\omega_2 = \frac{1}{2}(\sqrt{3}i - 1)\omega_1$, which produces a tessellation of parallelograms each made of two equilateral triangles.

8.6 Inverse functions of Weierstrass elliptic functions

In the main text explicit solutions for the nonlinear ODE $m''(x) \propto m^{\frac{d+2}{d-2}}$ have been derived for special values of d in terms of the lemniscatic and equiharmonic Weierstrass elliptic functions $\wp_l$ and $\wp_e$. When solving the equation for generic d a solution has been presented in implicit form. This allows us to write the following inversion formulas for $\wp_l$ and $\wp_e$:

$$\wp_l{}^{-1}(x) = \frac{1}{\sqrt{x}}\ {}_2F_1\left(\frac{1}{4}, \frac{1}{2}; \frac{5}{4}; \frac{1}{4x^2}\right) \tag{8.10}$$

$$\wp_e{}^{-1}(x) = \frac{1}{\sqrt{x}}\ {}_2F_1\left(\frac{1}{6}, \frac{1}{2}; \frac{7}{6}; \frac{1}{4x^3}\right). \tag{8.11}$$

These two results can be obtained by considering different representation of the elliptic integrals $\int \mathrm{d}x \frac{1}{\sqrt{4x^3-1}}$ and $\int \mathrm{d}x \frac{1}{\sqrt{4x^3-x}}$.

8.7 Miscellaneous results

For the case of the four-dimensional Ising model, we also measured two-point correlations, and plotted a similar correlation ratio collapse as for the case of the three-dimensional Clock model. The distance was computed for aligned points, i.e. with the same parallel coordinates and different transverse coordinate x. This way, all geodesics are guaranteed to be straight lines orthogonal to the slab. The distance is still different than the euclidean one, since it was obtained by integrating the square root of the metric. The resulting plot of $r(x,y) = \langle\phi(x)\phi(y)/\langle\phi(x)\rangle\langle\phi(y)\rangle\rangle$ is shown in Fig. 8.1.

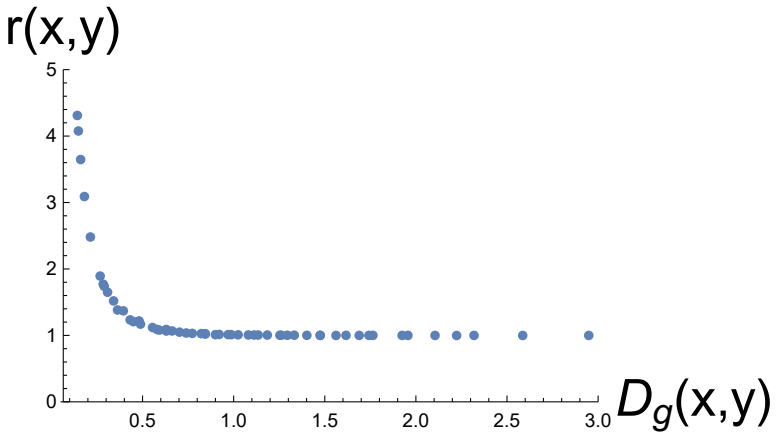

Figure 8.1: Correlation ratio of the four-dimensional Ising model for aligned points at $L = 32$.

Bibliography

[1] G. Gori and A. Trombettoni. "Geometry of bounded critical phenomena". In: *J. Stat. Mech: Theory Exp.* 2020.6 (2020), p. 063210.

[2] A. Galvani, G. Gori, and A. Trombettoni. "Critical 1- and 2-point spin correlations for the O(2) model in 3d bounded domains". In: *J. High Energy Phys.* 2021.10 (2021).

[3] A. Galvani, A. Trombettoni, and G. Gori. "High-precision anomalous dimension of three-dimensional percolation and spatial profile of the critical giant cluster". In: *Phys. Rev. E* 106 (6 2022), p. 064111.

[4] A. Galvani, G. Gori, and A. Trombettoni. "Magnetization profiles at the upper critical dimension as solutions of the integer Yamabe problem". In: *Phys. Rev. E* 104.2 (2021), p. 024138.

[5] H. Nishimori and G. Ortiz. *Elements of Phase Transitions and Critical Phenomena*. Oxford University Press, 2010.

[6] G. Parisi and R. Shankar. "Statistical Field Theory". In: *Physics Today* 41.12 (1988), pp. 110–110.

[7] R. J. Baxter. "Exactly Solved Models in Statistical Mechanics". In: *Series on Advances in Statistical Mechanics*. World Scientific, 1985, pp. 5–63.

[8] E. F. W. Heffern, H. Huelskamp, S. Bahar, and R. F. Inglis. "Phase transitions in biology: from bird flocks to population dynamics". In: *Proceedings of the Royal Society B: Biological Sciences* 288.1961 (2021).

[9] K. Kashiwa, Y. Kikuchi, and A. Tomiya. "Phase transition encoded in neural network". In: *Progress of Theoretical and Experimental Physics* 2019.8 (2019).

[10] J. A. Lipa, D. R. Swanson, J. A. Nissen, Z. K. Geng, P. R. Williamson, D. A. Stricker, T. C. P. Chui, U. E. Israelsson, and M. Larson. "Specific Heat of Helium Confined to a 57- μm Planar Geometry near the Lambda Point". In: *Phys. Rev. Lett.* 84 (2000), pp. 4894–4897.

[11] J. A. Lipa, D. R. Swanson, J. A. Nissen, T. C. P. Chui, and U. E. Israelsson. "Heat Capacity and Thermal Relaxation of Bulk Helium very near the Lambda Point". In: *Phys. Rev. Lett.* 76 (1996), pp. 944–947.

[12] S. M. Chester, W. Landry, J. Liu, D. Poland, D. Simmons-Duffin, N. Su, and A. Vichi. "Carving out OPE space and precise O(2) model critical exponents". In: *J. High Energy Phys.* 2020.6 (2020).

[13] L. Onsager. "Crystal Statistics. I. A Two-Dimensional Model with an Order-Disorder Transition". In: *Phys. Rev.* 65 (3-4 1944), pp. 117–149.

[14] N. Goldenfeld. *Phase Transitions (Frontiers in Physics, 85)*. Westview Press, 1962, p. 420. ISBN: 9780201554090.

[15] M. Kardar. *Statistical Physics of Fields*. Cambridge University Press, 2012. ISBN: 9780511815881.

[16] M. Creutz. *Quarks, gluons and lattices*. Cambridge Monographs on Mathematical Physics. Cambridge: Cambridge Univ. Press, June 1985. ISBN: 978-0-521-31535-7.

[17] H. J. Rothe and K. D. Rothe. *Classical and Quantum Dynamics of Constrained Hamiltonian Systems*. Singapore: World Scientific, 2010.

[18] E. Fradkin. *Field Theories of Condensed Matter Physics*. Cambridge: Cambridge University Press, 2013.

[19] J. B. Kogut and D. K. Sinclair. "Evidence for O(2) universality at the finite temperature transition for lattice QCD with 2 flavors of massless staggered quarks". In: *Phys. Rev. D* 73.7 (2006).

[20] P. Springer and B. Klein. "O(2)-scaling in finite and infinite volume". In: *Eur. Phys. J. C* 75.10 (2015).

[21] T. Matsubara and H. Matsuda. "A Lattice Model of Liquid Helium, I". In: *Prog. Theor. Phys.* 16.6 (1956), pp. 569–582.

[22] D. D. Betts and J. R. Lothian. "Comparison of the Critical Properties of the $s = 1/2$ XY Model and Liquid Helium Near the Lambda Transition". In: *Can. J. Phys.* 51.21 (1973), pp. 2249–2259.

[23] M. Hasenbusch. "Monte Carlo study of an improved clock model in three dimensions". In: *Phys. Rev. B* 100.224517 (Oct. 14, 2019).

[24] J. M. Kosterlitz and D. J. Thouless. "Ordering, metastability and phase transitions in two-dimensional systems". In: *J. Phys. C: Solid State Phys.* 6.7 (1973), pp. 1181–1203.

[25] J. M. Kosterlitz. "Nobel Lecture: Topological defects and phase transitions". In: *Rev. Mod. Phys.* 89.4 (2017), p. 040501.

[26] S. R. Shenoy. "Vortex-loop scaling in the three-dimensional XY ferromagnet". In: *Phys. Rev. B* 40.7 (1989), pp. 5056–5068.

[27] A. Forrester and G. A. Williams. "Vortex-loop calculation of the specific heat of superfluid He4 under pressure". In: *Phys. Rev. E* 100.6 (2019).

[28] V. Cvetkovic and J. Zaanen. "Vortex duality: Observing the dual nature using order propagators". In: *Physical Review B* 74.13 (2006).

[29] D. Stauffer and A. Aharony. *Introduction to Percolation Theory*. London: Taylor & Francis, 2018.

[30] G. Grimmett. *Percolation*. Berlin and Heidelberg: Springer, 1999.

[31] N. Araújo, P. Grassberger, B. Kahng, K. Schrenk, and R. Ziff. "Recent advances and open challenges in percolation". In: *Eur. Phys. J. Special Topics* 223.11 (2014), pp. 2307–2321. DOI: 10.1140/epjst/e2014-02266-y.

[32] P. J. Flory. "Molecular Size Distribution in Three Dimensional Polymers. I. Gelation". In: *Journal of the American Chemical Society* 63.11 (1941), pp. 3083–3090. DOI: 10.1021/ja01856a061. eprint: https://doi.org/10.1021/ja01856a061.

[33] W. H. Stockmayer. "Theory of Molecular Size Distribution and Gel Formation in Branched Polymers II. General Cross Linking". In: *J. Chem. Phys.* 12.4 (1944), pp. 125–131.

[34] G Caldarelli, R Frondoni, A Gabrielli, M Montuori, R Retzlaff, and C Ricotta. "Percolation in real wildfires". In: *Europhys. Lett. (EPL)* 56.4 (2001), pp. 510–516.

[35] P. Grassberger. "On the critical behavior of the general epidemic process and dynamical percolation". In: *Math. Biosci.* 63.2 (1983), pp. 157–172.

[36] L. Sander, C. Warren, I. Sokolov, C. Simon, and J. Koopman. "Percolation on heterogeneous networks as a model for epidemics". In: *Math. Biosci.* 180.1-2 (2002), pp. 293–305.

[37] M. E. J. Newman, I. Jensen, and R. M. Ziff. "Percolation and epidemics in a two-dimensional small world". In: *Phys. Rev. E* 65.2 (2002), p. 021904. DOI: 10.1103/physreve.65.021904.

[38] J. C. Miller. "Percolation and epidemics in random clustered networks". In: *Phys. Rev. E* 80.2 (2009).

[39] J. J. Binney, N. J. Dowrick, A. J. Fisher, and M. E. J. Newman. *The Theory of Critical Phenomena: An Introduction to the Renormalization Group*. 1992.

[40] P. W. Kasteleyn and C. M. Fortuin. "Phase Transitions in Lattice Systems with Random Local Properties". In: *Physical Society of Japan Journal Supplement* 26 (Jan. 1969), p. 11.

[41] G. Delfino and J. L. Cardy. "Universal amplitude ratios in the two-dimensional q-state Potts model and percolation from quantum field theory". In: (). arXiv: `hep-th/9712111`.

[42] M. E. Fisher and P. G. de Gennes. "Wall Phenomena in a Critical Binary Mixture". In: *C. R. Acad. Sci. Paris.* B 287. 1978, pp. 207–209.

[43] A. Bray and M. Moore. "Critical behaviour of semi-infinite systems". In: *J. Phys. A: Math. Gen.* 10.11 (1977), p. 1927.

[44] H. W. Diehl and S. Dietrich. "Scaling laws and surface exponents from renormalization group equations". In: *Phys. Lett. A* 80.5-6 (1980), pp. 408–412.

[45] H. W. Diehl and S. Dietrich. "Field-theoretical approach to static critical phenomena in semi-infinite systems". In: *Z. Phys., B Condens. matter* 42.1 (1981), pp. 65–86.

[46] T. C. Lubensky and M. H. Rubin. "Critical phenomena in semi-infinite systems. I. ε expansion for positive extrapolation length". In: *Phys. Rev. B* 11.11 (1975), p. 4533.

[47] D. Grüneberg and H. W. Diehl. "Thermodynamic Casimir effects involving interacting field theories with zero modes". In: *Phys. Rev. B* 77.11 (2008), p. 115409.

[48] H. W. Diehl and S. B. Rutkevich. "The three-dimensional O(n) ϕ^4 model on a strip with free boundary conditions: exact results for a nontrivial dimensional crossover in the limit $n \to \infty$". In: *Theor. Math. Phys.* 190.2 (2017), pp. 279–294.

[49] A Gambassi and S Dietrich. "Comment on "The Casimir effect for the Bose-gas in slabs" by P. A. Martin and V. A. Zagrebnov. Relation between the thermodynamic Casimir effect in Bose-gas slabs and critical Casimir forces". In: *Europhys. Lett.* 74.4 (May 2006), pp. 754–755.

[50] A. Gambassi and S. Dietrich. "Critical dynamics in thin films". In: *J. Stat. Phys.* 123.5 (2006), pp. 929–1005.

[51] O. Vasilyev, A. Gambassi, A. Maciołek, and S. Dietrich. "Monte Carlo simulation results for critical Casimir forces". In: *Europhys. Lett.* 80.6 (2007), p. 60009.

[52] N. Farahmand Bafi, A. Maciołek, and S. Dietrich. "Tricritical Casimir forces and order parameter profiles in wetting films of ^{3}He$-^4$He mixtures". In: *Phys. Rev. E* 95 (2017), p. 032802.

[53] J. Cardy. *Finite-size Scaling*. Current physics. ISBN: 9780444871107.

[54] M. Barber. In: *Phase Transitions and Critical Phenomena*. Ed. by C. Domb, M. Green, and J. L. Lebowitz. Vol. 8. New York: Academic Press, 1983.

[55] H. W. Diehl. "The Theory of boundary critical phenomena". In: *Int. J. Mod. Phys.* B11 (1997), pp. 3503–3523.

[56] I. Titvinidze and M. Potthoff. "Boundary and finite-size effects in the competition between indirect magnetic exchange and Kondo screening". In: *Journal of the Korean Physical Society* 62.10 (2013), pp. 1434–1439.

[57] S. Wu. "Topological quantum field theories on manifolds with a boundary". In: *Communications in mathematical physics* 136.1 (1991), pp. 157–168.

[58] Z. Haba. "Quantum field theory on manifolds with a boundary". In: (). arXiv: `hep-th/0506146`.

[59] E. Eisenriegler. *Polymers Near Surfaces*. WORLD SCIENTIFIC, 1993.

[60] A. M. Polyakov. "Conformal symmetry of critical fluctuations". In: *JETP Lett.* 12 (1970), pp. 381–383.

[61] A. Belavin, A. Polyakov, and A. Zamolodchikov. "Infinite conformal symmetry in two-dimensional quantum field theory". In: *Nucl. Phys. B* 241.2 (1984), pp. 333–380.

[62] J. L. Cardy. "Conformal invariance and surface critical behavior". In: *Nucl. Phys. B* 240.4 (1984), pp. 514–532.

[63] J. L. Cardy. "Boundary conditions, fusion rules and the Verlinde formula". In: *Nucl. Phys. B* 324.3 (1989), pp. 581–596.

[64] J. L. Cardy. "Boundary Conformal Field Theory". In: *Encyclopedia of Mathematical Physics*. Ed. by T. S. T. J.-P. Françoise G. L. Naber. Elsevier, 2006, pp. 333–340.

[65] J. Maldacena. In: *International Journal of Theoretical Physics* 38.4 (1999), pp. 1113–1133.

[66] J. McGreevy. "Holographic duality with a view toward many-body physics". In: (2009).

[67] J. L. Cardy. "Scaling and renormalization in statistical physics". In: *Cambridge Lecture Notes in Physics*. Vol. 5. Cambridge: Cambridge university press, 1996.

[68] R. M. Ziff. "Effective boundary extrapolation length to account for finite-size effects in the percolation crossing function". In: *Phys. Rev. E* 54.3 (1996), pp. 2547–2554.

[69] N. D. Mermin and H. Wagner. "Absence of Ferromagnetism or Antiferromagnetism in One- or Two-Dimensional Isotropic Heisenberg Models". In: *Phys. Rev. Lett.* 17.22 (1966), pp. 1133–1136. DOI: 10.1103/physrevlett.17.1133.

[70] P. Di Francesco, P. Mathieu, and D. Sénéchal. *Conformal Field Theory*. Graduate texts in contemporary physics. New York: Springer, 1997.

[71] B. Nienhuis. In: *Phase Transitions and Critical Phenomena*. Ed. by C. Domb, M. Green, and J. L. Lebowitz. Vol. 11. London: Academic Press, 1987.

[72] J. L. Cardy. In: *Phase Transitions and Critical Phenomena*. Ed. by C. Domb, M. Green, and J. L. Lebowitz. Vol. 11. London: Academic Press, 1987.

[73] J. J. H. Simmons, P. Kleban, K. Dahlberg, and R. M. Ziff. "The density of critical percolation clusters touching the boundaries of strips and squares". In: *J. Stat. Mech.* 2007.06 (2007), P06012–P06012.

[74] J. L. Cardy. "Critical percolation in finite geometries". In: *Journal of Physics A: Mathematical and General* 25.4 (1992), pp. L201–L206.

[75] A. L. Kholodenko and E. E. Ballard. "From Ginzburg–Landau to Hilbert–Einstein via Yamabe". In: *Physica A* 380 (2007), pp. 115–162. ISSN: 0378-4371.

[76] M. Kwaśnicki. "Ten equivalent definitions of the fractional Laplace operator". In: *Fract. Calc. Appl. Anal.* 20.1 (2017).

[77] C. Pozrikidis. *The Fractional Laplacian*. CRC PR INC, Feb. 2016. 278 pp. ISBN: 1498746152.

[78] L. Caffarelli and L. Silvestre. "An Extension Problem Related to the Fractional Laplacian". In: *Commun. Partial. Differ. Equ.* 32.8 (2007), pp. 1245–1260.

[79] C. Bucur. "Some nonlocal operators and effects due to nonlocality". PhD thesis. May 2017. arXiv: 1705.00953 [math.AP].

[80] C. R. Graham and M. Zworski. "Scattering matrix in conformal geometry". In: *Invent. Math.* 152.1 (2003), pp. 89–118.

[81] S.-Y. A. Chang and M. del Mar González. "Fractional Laplacian in conformal geometry". In: *Adv. Math.* 226.2 (2011), pp. 1410 –1432. ISSN: 0001-8708.

[82] S. M. Paneitz. "A Quartic Conformally Covariant Differential Operator for Arbitrary Pseudo-Riemannian Manifolds (Summary)". In: (2008).

[83] M. del Mar González and J. Qing. "Fractional conformal Laplacians and fractional Yamabe problems". In: *Anal. PDE* 6.7 (2013), pp. 1535–1576.

[84] A. Gambassi, A. Maciołek, C. Hertlein, U. Nellen, L. Helden, C. Bechinger, and S. Dietrich. "Critical Casimir effect in classical binary liquid mixtures". In: *Phys. Rev. E* 80.6 (2009).

[85] V. M. Vassilev, D. M. Dantchev, and P. A. Djondjorov. "Order parameter profiles in a system with Neumann – Neumann boundary conditions". In: *MATEC Web Conf.* 145 (2018), p. 01009.

[86] A Maciołek, M Krech, and S Dietrich. "Phase diagram of a model for 3 He- 4 He mixtures in three dimensions". In: *Phys. Rev. E* 69.3 (2004), p. 036117.

[87] W. Deng and W Zimmermann Jr. "Parallel-plate capacitor measurements of the superfluid wall-film thickness in a ^{3}He/^{4}He mixture of ^{3}He mole fraction x= 0.75". In: *J. Phys. Conf. Ser.* Vol. 150. 3. IOP Publishing. 2009, p. 032018.

[88] C. Hertlein, L. Helden, A. Gambassi, S. Dietrich, and C. Bechinger. "Direct measurement of critical Casimir forces". In: *Nature* 451.7175 (2008), pp. 172–175.

[89] K. Binder. "Critical Behaviour at Surfaces". In: *Phase Transitions and Critical Phenomena*. Ed. by C. Domb. Vol. 8. Elsevier, 2000. Chap. 1.

[90] M. A. Metlitski. "Boundary criticality of the O(N) model in d = 3 critically revisited". In: (Sept. 7, 2020). arXiv: `http://arxiv.org/abs/2009.05119v1 [cond-mat.str-el]`.

[91] J. Hove and A. Sudbø. "Criticality versus q in the (2+1)-dimensional Z_q clock model". In: *Phys. Rev. E* 68.4 (2003).

[92] M. Creutz, L. Jacobs, and C. Rebbi. "Monte Carlo study of Abelian lattice gauge theories". In: *Phys. Rev. D* 20.8 (1979), pp. 1915–1922.

[93] U. Wolff. "Collective Monte Carlo updating for spin systems". In: *Phys. Rev. Lett.* 62.4 (1989), p. 361.

[94] J. Kent-Dobias and J. P. Sethna. "Cluster representations and the Wolff algorithm in arbitrary external fields". In: *Phys. Rev. E* 98.6 (2018).

[95] K. A. Brakke. "The Surface Evolver". In: *Experimental Mathematics* 1.2 (1992), pp. 141–165. ISSN: 1058-6458.

[96] F. Kos, D. Poland, D. Simmons-Duffin, and A. Vichi. "Precision islands in the Ising and O(N) models". In: *J. High Energy Phys.* 2016.8 (2016).

[97] S. El-Showk, M. F. Paulos, D. Poland, S. Rychkov, D. Simmons-Duffin, and A. Vichi. "Solving the 3D Ising model with the conformal bootstrap". In: *Phys. Rev. D* 86.2 (2012), p. 025022.

[98] R. Rattazzi, V. S. Rychkov, E. Tonni, and A. Vichi. "Bounding scalar operator dimensions in 4D CFT". In: *J. High Energy Phys.* 2008.12 (2008), pp. 031–031.

[99] M. D. Rintoul and S Torquato. "Precise determination of the critical threshold and exponents in a three-dimensional continuum percolation model". In: *J. Phys. A: Math. Gen.* 30.16 (1997), pp. L585–L592.

[100] S. Mertens and C. Moore. "Continuum percolation thresholds in two dimensions". In: *Phys. Rev. E* 86.6 (2012), p. 061109.

[101] G. Gori and A. Trombettoni. "Conformal invariance in three dimensional percolation". In: *J. Stat. Mech: Theory Exp.* 2015.7 (2015), P07014.

[102] J. J. H. Simmons, P. Kleban, and R. M. Ziff. "Exact factorization of correlation functions in two-dimensional critical percolation". In: *Phys. Rev. E* 76.4 (2007), p. 041106.

[103] J. J. H. Simmons, R. M. Ziff, and P. Kleban. "Factorization of percolation density correlation functions for clusters touching the sides of a rectangle". In: *J. Stat. Mech.: Theory Exp.* 2009.02 (2009), P02067.

[104] J. J. H. Simmons, P. Kleban, S. M. Flores, and R. M. Ziff. "Cluster densities at 2D critical points in rectangular geometries". In: *J. Phys. A: Math. Theor.* 44.38 (2011), p. 385002.

[105] G. Delfino and J. Viti. "On three-point connectivity in two-dimensional percolation". In: *J. Phys. A: Math. Theor.* 44.3 (2010), p. 032001.

[106] C. D. Lorenz and R. M. Ziff. "Precise determination of the critical percolation threshold for the three-dimensional "Swiss cheese" model using a growth algorithm". In: *J. Chem. Phys.* 114.8 (2001), pp. 3659–3661.

[107] J. Adler, Y. Meir, A. Aharony, and A. B. Harris. "Series study of percolation moments in general dimension". In: *Phys. Rev. B* 41.13 (1990), pp. 9183–9206.

[108] C. D. Lorenz and R. M. Ziff. "Precise determination of the bond percolation thresholds and finite-size scaling corrections for the sc, fcc, and bcc lattices". In: *Phys. Rev. E* 57.1 (1998), pp. 230–236.

[109] N. Jan and D. Stauffer. "Random Site Percolation in Three Dimensions". In: *Int. J. Mod. Phys. C* 09.02 (1998), pp. 341–347.

[110] X. Xu, J. Wang, J.-P. Lv, and Y. Deng. "Simultaneous analysis of three-dimensional percolation models". In: *Frontiers of Physics* 9.1 (2013), pp. 113–119.

[111] H. G. Ballesteros, L. A. Fernández, V Martín-Mayor, A. M. Sudupe, G Parisi, and J. J. Ruiz-Lorenzo. "Scaling corrections: site percolation and Ising model in three dimensions". In: *J. Phys. A: Math. Gen.* 32.1 (1999), pp. 1–13.

[112] J. A. Gracey. "Four loop renormalization of φ^3 theory in six dimensions". In: *Phys. Rev. D* 92.2 (2015).

[113] M. Borinsky, J. A. Gracey, M. V. Kompaniets, and O. Schnetz. "Five loop renormalization of ϕ^3 theory with applications to the Lee-Yang edge singularity and percolation theory". In: (Mar. 2021). arXiv: `2103.16224 [hep-th]`.

[114] H. Tasaki. "Hyperscaling inequalities for percolation". In: *Commun Math Phys* 113.1 (1987), pp. 49–65.

[115] A. Sur, J. L. Lebowitz, J. Marro, M. H. Kalos, and S. Kirkpatrick. "Monte Carlo studies of percolation phenomena for a simple cubic lattice". In: *J. Stat. Phys.* 15.5 (1976), pp. 345–353.

[116] G. Mussardo. *Statistical Field Theory: an Introduction to Exactly Solved Models in Statistical Physics*. 2nd ed. Oxford: Oxford University Press, 2020. ISBN: 9780198788102.

[117] *NIST Digital Library of Mathematical Functions*. http://dlmf.nist.gov/, Release 1.1.0 of 2020-12-15. F. W. J. Olver, A. B. Olde Daalhuis, D. W. Lozier, B. I. Schneider, R. F. Boisvert, C. W. Clark, B. R. Miller, B. V. Saunders, H. S. Cohl, and M. A. McClain, eds. URL: `http://dlmf.nist.gov/`.

[118] R. Zandi, A. Shackell, J. Rudnick, M. Kardar, and L. P. Chayes. "Thinning of superfluid films below the critical point". In: *Phys. Rev. E* 76 (2007), p. 030601.

[119] M. Panero and A. Smecca. "Topological excitations in statistical field theory at the upper critical dimension". In: *J. High Energy Phys.* 2021.3 (2021).

[120] Z. Borjan and P. J. Upton. "Order-Parameter Profiles and Casimir Amplitudes in Critical Slabs". In: *Phys. Rev. Lett.* 81.22 (1998), p. 4911.

[121] M. E. Fisher and P. J. Upton. "Fluid interface tensions near critical end points". In: *Phys. Rev. Lett.* 65.27 (1990), pp. 3405–3408.

[122] D. J. Amit, D. J. Wallace, and R. K. P. Zia. "Universality in the percolation problem—Anomalous dimensions of φ^4 operators". In: *Phys. Rev. B* 15.10 (1977), p. 4657.

[123] O. F. de Alcantara Bonfirm, J. E. Kirkham, and A. J. McKane. "Critical exponents for the percolation problem and the Yang-Lee edge singularity". In: *J. Phys. A: Math. Gen.* 14.9 (1981), pp. 2391–2413.

[124] A. Polyanin and V. Zaitsev. *Handbook of Exact Solutions for Ordinary Differential Equations*. Boca Raton: CRC Press, 1995.

[125] M. Krech. "Casimir forces in binary liquid mixtures". In: *Phys. Rev. E* 56.2 (1997), p. 1642.

[126] E. Carlon and F. Iglói. "Density profiles, Casimir amplitudes, and critical exponents in the two-dimensional Potts model: A density-matrix renormalization study". In: *Phys. Rev. B* 57.13 (1998), pp. 7877–7886.

[127] D. J. Amit and V. Martin-Mayor. *Field Theory, the Renormalization Group, and Critical Phenomena*. 3rd ed. Singapore: World Scientific, 2005. ISBN: 9812561099.

[128] M. Le Bellac. *Quantum and Statistical Field Theory*. 1st ed. Oxford: Clarendon, 1991. ISBN: 0198539290.

[129] S. Rychkov. *EPFL Lectures on Conformal Field Theory in $D \geq 3$ Dimensions*. Springer, 2017.

[130] C. Cosme, J. V. P. Lopes, and J. Penedones. "Conformal symmetry of the critical 3D Ising model inside a sphere". In: *J. High Energy Phys.* 2015.8 (2015), pp. 1–15.

[131] E. Luijten. "Interaction Range, Universality and the Upper Critical Dimension". PhD thesis. 1997.

[132] E. Bittner, W. Janke, and H. Markum. "Ising spins coupled to a four-dimensional discrete Regge skeleton". In: *Phys. Rev. D* 66 (2002), p. 024008.

[133] P. H. Lundow and K. Markström. "Critical behavior of the Ising model on the four-dimensional cubic lattice". In: *Phys. Rev. E* 80 (2009), p. 031104.

[134] H. E. Stanley. "Spherical Model as the Limit of Infinite Spin Dimensionality". In: *Phys. Rev.* 176 (2 1968), pp. 718–722.

[135] T. H. Berlin and M. Kac. "The Spherical Model of a Ferromagnet". In: *Phys. Rev.* 86 (6 1952), pp. 821–835.

[136] S. Hikami and R. Abe. "A Few Layered n-Vector Model in the Limit $n \to \infty$". In: *Progress of Theoretical Physics* 55.5 (May 1976), pp. 1412–1418. ISSN: 0033-068X.

[137] H. J. F. Knops. "Infinite spin dimensionality limit for nontranslationally invariant interactions". In: *Journal of Mathematical Physics* 14 (1973), pp. 1918–1920.

[138] K. Binder. "Finite size scaling analysis of Ising model block distribution functions". In: *Zeitschrift für Physik B Cond. Mat.* 43.2 (1981), pp. 119–140.

[139] M. E. J. Newman and R. M. Ziff. "Fast Monte Carlo algorithm for site or bond percolation". In: *Phys. Rev. E* 64.1 (2001).